Solitary and Transitional Waves in Two-Layer Microchannel Flows

by

Christopher James Bennett

A thesis submitted to
The University of Birmingham
for the degree of
DOCTOR OF PHILOSOPHY
IN APPLIED MATHEMATICS

School of Mathematics
The University of Birmingham
May 15, 2015

Abstract

The understanding of wave dynamics in interfacial microchannel flows is important for many technological applications in the micro-device industry. Here, a theoretical and numerical study is undertaken in order to understand the propagation of interfacial waves in a two-layer flow. The flow is considered to be driven by, in separate cases, the force of gravity and a pressure gradient. The results may provide steps towards more efficiently designed microfluidic products, and a better understanding of experimentally observed waves.

Acknowledgements

I must first thank my supervisor and friend, Grigori Sisoev, for all of his effort and support over the past four years. I will forever be indebted to him for the time he has kindly set aside to the benefit of my education. Discussions about our research, curtailed more often than not by conversations about Soviet history, European geography, culture, and language, amongst other unrelated topics, have been interesting and enjoyable. His expertise has been invaluable to this Thesis, and the publications to which it has led. He is an extremely kind, generous, and wise man, and to work with him has been a privilege.

I would also like to thank my family for their support throughout my university career, and in particular my Dad who, it seems, always knew I was capable of this.

Finally, I would like to thank the School of Mathematics for awarding me the scholarship which has funded this research.

List of Publications

1. G. Sisoev and C. Bennett. Solitary and transitional waves in gravity-driven two-layer microchannel flow. *Fluid Dynamics Research*, 45:015503, 2013

2. G. Sisoev and C. Bennett. Solitary and transitional waves in pressure-driven two-layer microchannel flow. *Fluid Dynamics Research*, 46:025504, 2014

Contents

List of Figures

Chapter 1

Introduction

Microfluidics concerns the understanding, modelling and manipulation of fluid flows in systems with typical characteristic dimensions in the order of 100μm. It is seen that, by shrinking fluidic systems down to a micro-scale, it is possible to exploit the scaling effects to achieve different results and, in many specific cases, better performance. For very small volumes of liquids, the surface to volume ratio is high. This provides short diffusion distances, which in turn leads to better efficiency of heat and mass transfer. However, as the scales are reduced so dramatically, the relative importance of forces governing the flow are altered considerably: volume forces such as gravitational acceleration and inertia are dominated by surface forces such as surface tension induced by capillary effects[1].

There are many advantages of micro-scale systems. Obviously, micro-devices are small in size and so can be fitted to portable devices. Although micro-heat exchangers are already used for electronic device cooling, one of the main goals for the micro-device industry is to incorporate such systems on to portable devices such as laptops, tablets, cameras and mobile phones [57, 35]. In addition to their minute size, the efficiency of micro-scale systems is very high, as mentioned above. Moreover, the level of efficiency can

[1]Capillarity is defined as the phenomena where intermolecular forces, namely the adhesive forces between fluid molecules and the adjoining material surface molecules, and the cohesive forces between neighbouring fluid particles, dominate over gravitational forces due to the insignificant mass of fluid involved.

be controlled within a large interval by varying the flow regimes within the device. This can be achieved by altering the flow parameters, for example the volumetric flow rate, or by adjusting the flow conditions. These changes are very quick to take effect due to the the small volumes of liquids involved. Furthermore, these systems operate at relatively low pressures and hence are inexpensive to run. It is clear that the scope for advances in efficiency extends to any industrial or technological process which requires fluid-fluid interaction for heat or mass transfer, extraction, or reaction.

Despite the numerous benefits of using micro-devices for heat and mass transfer, there are also some significant disadvantages and difficulties to consider. Firstly, and perhaps most importantly, since micro-systems are balanced in a very delicate manner in order to achieve a particular type of flow, they are susceptible to any minute disturbance which could potentially destroy the flow. If fitted to a portable device, the system should obviously be able to cope with continuous movement and changes in orientation, as well as deal with potentially significant changes in operating temperature. This is perhaps the most challenging obstacle facing the micro-device industry at present.

Similarly, if the parts containing the flow themselves have any defects, this will again alter the flow dramatically. Due to the precision needed, the manufacturing of such parts from traditional alloys currently utilises accurate laser welding methods, before being analysed by x-ray to detect any deficiencies. Recently however, techniques in microfabrication have improved extensively, providing many other ways in which to manufacture microchannels [57]. For example, chemical etching may be utilised to create channels in materials such as glass or silicon, but the finished product must still be carefully scrutinised, often with a microscope. The surface roughness of all fluid bounding materials must be kept to a negligible level too. This often means polishing surfaces so that the roughness perturbations of the surface are less than a nanometre, followed by a thorough cleaning of the surface using a solvent [15]. As a result of this meticulous attention to detail, the cost

of production of micro-systems is very expensive. Despite this, as a consequence of their applications in high-tech electronic devices in particular, the understanding of micro-flows is a priority at the forefront of current technological advances.

Here, micro-scale flows incorporating two liquids flowing simultaneously in a rectangular channel, of typical width $100 - 500\mu$m and sufficiently large aspect ratio[2], with no separating wall or membrane, are discussed. The aim is to find solitary and transitional wave regimes which develop on the interface of the two liquids due to developing instabilities.

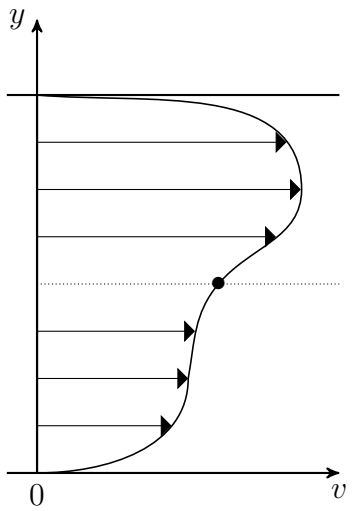

Figure 1.1: Velocity profile $v(y)$ of a two-phase flow showing the point of weak discontinuity.

These instabilities arise due to a variety of mechanisms, a classification of which was given by Boomkamp and Miesen [6]. The most significant of these instabilities are those due to the density and viscosity discontinuities across the interface. The instability due to the density discontinuity of the inclined fluids, is well known as the Rayleigh-Taylor instability [39, 58], and arises even if the acceleration due to gravity is replaced by another acceleration. The instability due to the discontinuity in viscosity across the layers, was originally discovered much later in a pioneering work by Yih [64]. In this paper, the linear stability analysis was carried out in the case of a horizontal pressure-driven, Poiseuille, two-layer flow. It was shown that the flow is unstable to long waves at any value of the Reynolds number, due to the viscosity stratification. Considering the velocity profile $v(y)$ of a two-layer flow, where each fluid has a different viscosity (see Fig. 1.1), it is apparent that there is a point of weak discontinuity at the interface. The discontinuity in the first derivative of velocity is attributed to the cause of the instability

[2]In many experiments [61, 31, 38], it is seen that the ratio of microchannel width to height ranged from 3 to 7, therefore allowing the development of the governing two-dimensional problem statement.

described by Yih [64].

In all cases, as the flow rate increases the flow becomes unstable, resulting in the formation and propagation of capillary waves on the interface, in the direction of the flow. These interfacial waves are the result of the competition between viscous, gravitational and capillary forces.

It is important that the Reynolds number remains roughly of order 100, so that an unsteady laminar flow is achieved[3]. Smaller Reynolds numbers would result in the interfacial perturbations vanishing. However, if much larger Reynolds numbers are considered, chaotic waves leading to turbulent flows would occur, yielding an undesired mixing of the liquids into an emulsion [67, 21]. The regular waves achieved by utilising the desired Reynolds number mentioned above, are predictable and can be manipulated to give new results.

Specifically, the type of waves considered here fall into two categories: solitary waves, a general type of the commonly studied 'soliton'; and transitional waves, comparable to a shock wave type disturbance but with a less abrupt change in properties. Solitary waves are waves of infinitely long wavelength, and are characterised locally by a set number of oscillations. They travel with constant velocity whilst maintaining their shape and amplitude. In many cases, a solitary wave is regarded as the limit long wave of a family of periodic solutions of the same shape. Transitional waves are comparable to solitary waves, but have the added property that they facilitate the thickening or thinning of a given layer of liquid. In order to allow the identification and classification of experimentally observed periodic interfacial waves, the aim of this Thesis is to provide details of the encompassing solitary wave solutions for a given system. The theoretical waves studied here are therefore considered to be of infinite length. It will be shown that each solitary wave indicates the

[3]Considering a flow of water in a microchannel of width 200μm, with Reynolds number of 100, the velocity scale required is 0.5m/s. Such a velocity scale is easily achieved in the case of a pressure driven flow, but will require the channel to be sufficiently long in the gravity driven case without the assistance of an additional external force.

existence of a corresponding family of periodic waves [43]. Many classical examples of non-linear partial differential equations modelling wave propagation have solitary wave solutions, for example, the Korteweg-de Vries equation[4].

The potential benefits of finding the type of flow regimes sought here, are two fold. Each solitary wave indicates the existence of a family of steady-travelling periodic waves which may be generated and controlled in applications. Thus, the heat or mass transfer between the two fluids for a given length scale will be greatly improved, due to the increased contact area between the liquids and also the altered concentration/temperature distribution within them [51]. Secondly, since the types of wave regimes considered here are difficult to observe experimentally, the theoretical results discovered will help to understand practical findings. Much attention has been focused on improving the quality of experimental visualisations. The use of high speed, high definition video cameras is commonly used to try to accurately capture microscopic flows of liquids with fluorescent additives, illuminated in the corresponding fashion. Furthermore, shadowgraphy[5] can be used to identify changes in the flow characteristics [57, 15]. However, as discussed in more detail in Chapter 4, it may be easier and more accurate, to measure the pressure distribution at intervals along the microchannel in order to build up a profile of the flow which arises.

Below, a brief history of the considered problem is given, with reference to the most notable publications in the field.

As discussed above, two-phase microchannel flows play a key role in many technological processes [56, 66] due to their high efficiency, which depends on the flow conditions and physical properties of the fluids [26].

[4]The Korteweg-de Vries equation, often abbreviated to KdV, is a model for small amplitude, long wavelength waves of the surface of an expanse of shallow water.

[5]Shadowgraphy is a method used to detect changes in the properties of a transparent fluid by passing light through it, and observing the resulting 'shadow'. Many details which may otherwise be invisible can be detected, such a flow patterns, and the temperature distribution.

Firstly, as confirmed by the following experimental works, the Reynolds number is critical in determining the type of flow which is achieved. Experiments with a two-layer flow of oil and water in a horizontal (macro) channel were carried out by Charles and Lilleleht [13]. In the case of turbulence in the water layer, large regular two-dimensional interfacial waves were observed at oil Reynolds numbers below 500. Experiments by Kao and Park [24], also used the oil-water system, and the results confirmed the critical Reynolds number for the water layer, but the interface was undisturbed below this critical value.

In the case of microchannel flows, two stable parallel streams have been observed in many experiments [8]. Conversely, Zhao *et al.* [67, 68] observed that, when the Reynolds number varied between 19 and 650, flow regimes with both smooth and wavy interfaces occurred. In further experiments [55], the pressure driven air-liquid flow, in microchannels of width was less than 500 μm, demonstrated the formation of stationary interfacial waves.

Therefore, the key to enforcing the desired interfacial disturbances is to maintain a Reynolds number that is large enough to excite the interface from its stable waveless flow, but is also below the threshold at which turbulence begins to occur. The result will be a laminar two layer flow with wavy interface, which not only increases the contact area between the two fluids, but also alters the concentration or temperature distribution within them, leading to more efficient heat and mass transfer. Furthermore, if the interface returns to its undisturbed level after the wave has passed, the layers of fluid can be easily separated at the channel exit.

As eluded to earlier, the co-current flow of two immiscible liquids in a channel is subject to important instability mechanisms. Since the pioneering work by Yih [64], numerous theoretical studies have been carried out to study the linear stability analysis of the problem. Furthermore, there are many publications concerning weakly non-linear equations which describe the dynamics of waves whose wavelengths are close to the neutral

wavelengths. In the case of a simple pressure driven flow between two static parallel plates, Poiseuille flow, the asymptotic solution initially found by Yih [64], was extended by Yiantsios and Higgins [63] for short waves. In parallel with the interfacial mode, numerical solutions of the Orr-Sommerfeld problem[6] also revealed the existence of the shear unstable mode at relatively high values of the Reynolds number. Linear stability of horizontal gas-liquid flow was also studied by Kuru *et al.* [29] as an Orr-Sommerfeld type problem. Moreover, a numerical analysis of the unstable modes in a two-layer Poiseuille flow, in the case of equal densities of the liquids and thicknesses of the layers, as well as the absence of surface tension, was carried out by South and Hooper [54].

In the case of a plane Poiseuille-Couette flow, the combination of Poiseuille flow and Couette flow, where a moving plate drives the fluid by viscous resistance, the linear stability analysis originally carried out by Yih [64], was modified in the work by Hooper and Grimshaw [23] by retaining the surface tension term. The resulting weakly non-linear equation, which can be reduced to Burger's equation for a specific case, was found by applying the lubrication approximation[7] for small values of the Reynolds number, $\mathrm{Re} = O(1)$. Since surface tension was included in the model, stability of short waves is provided, and solutions demonstrated the formation of steady travelling waves. Again using the lubrication theory, another weakly non-linear evolution system for the Couette-Poiseuille flow was derived by Charru and Fabre [14]. The authors considered a specific interval for the value of the surface tension, in order to study the linear stability.

In the case of a horizontal channel, the integro-differential equation derived by Arkhipov and Khabakhpashev [4, 5] for long small-amplitude waves, is reduced to the Korteweg-de Vries equation if energy dissipation can be neglected.

[6]The Orr-Sommerfeld equation is an eigenvalue problem, derived from the Navier-Stokes equations with perturbed velocity field, which predicts the instability of disturbances in a parallel laminar flow.

[7]The lubrication approximation exploits the fact that inertial forces are small compared to viscous forces. Hence, the approximation may be applied to flows attaining very small values of the Reynolds number.

There are very few works concerning non-linear waves in two-layer flows with large viscosity and/or density stratification. Two-layer Couette flow was analysed by Roberts *et al.* [40] in the case of a large viscosity stratification using the modified Kuramoto-Sivashinsky equation[8]. The case of a counter-flowing liquid-gas system was studied under the lubrication approximation by Segin *et al.* [42].

In the specific case of a high viscosity ratio, weakly non-linear evolution equations were derived and solved by Matar *et al.* [32] but again within the framework of the lubrication approximation. It was shown that transient computations led to the formation of steady-travelling waves. This evolution system was later generalised by the same group [33], by taking into consideration the channel inclination. It was shown that in the case when the viscosity ratio of the two fluids was high, but the densities were closely matched, solitary waves were formed.

A specific type of Galerkin discretisation method, in conjunction with particle tracking, was used by Frank [17, 18] to solve the full Navier-Stokes problem modelling shear driven waves in a liquid-gas system. It was shown that increasing the Reynolds number of the gas flow led to a conversion of limit steady waves, from sinusoidal waves to solitary waves.

The effect of gravity was taken into consideration by Tilley *et al.* [59] where the flow in an inclined channel was numerically investigated to identify unstable modes, and their dependence on the similarity parameters. Gravity-driven two-layer flow in an inclined channel was again studied by Tilley *et al.* [60] but this time in the framework of a weakly non-linear equation, generalising the Kuramoto-Sivashinsky equation.

Numerical results by Zhang *et al.* [65], calculated by the front tracking numerical method, without explicit treatment of the interface, did not demonstrate formation of permanent non-linear stationary waves. In actual fact, fingers in the interfacial domain were observed at studied intervals of the similarity parameters, similar to the instabilities

[8]The Kuramoto-Sivashinsky equation, often abbreviated to K-S, describes the interfacial long-wave dynamics of film flows, and the development of interfacial disturbances.

found by Cao *et al*, where a pressure-driven flow at small values of the Reynolds number was considered. Cao *et al.* [9] also applied the front-tracking method, without explicit treatment of the interface, to analyse the linear stability of a two-layer viscosity stratified flow and the non-linear development of perturbations. However, analysis of the linear stability was carried out without consideration of the effects of surface tension, which led to the non-physical conclusion that shorter waves are more unstable. The non-linear solutions demonstrating finger-like structures, were seen to occur even at relatively small Reynolds numbers, and were calculated using the interfacial velocity and the thickness and viscosity of the more viscous liquid.

The lubrication approximation was again used by Mavromoustaki *et al.* [34] to derive an evolution equation modelling transitional waves, where the first layer thickness attains a different level at positive and negative infinity. Some solutions were computed by transient numerical simulations .

Since the two-layer microchannel flow may, in fact, be considered as a flow of two films sharing the same surface whose perturbations are bounded by the channel width, it is important to study inherent features of the flow at real-life values of the physical parameters. This may be achieved by using methods and results from the more developed theory of falling films, in particular the work done by Alekseenko *et al.* [3], Chang [11], and Chang and Demekhin [12].

A non-linear model describing a gravity-driven two-layer microchannel flow, at a moderate value of the Reynolds number, was formulated by Sisoev *et al.* [52]. It was shown that the model generates a spectrum of eigenvalues which are in good agreement with the linear spectrum of the full Navier-Stokes problem. Furthermore, the model can be reduced to the falling film case. However, calculations of periodic steady travelling waves revealed differing wave shapes in comparison with the case of the falling film, in particular for very long waves. In Chapter 2 of this Thesis, the model derived by Sisoev *et al.* [52] is

re-formulated as a dynamical system in order to investigate limit long waves, or solitary waves. As mentioned above, in flows which demonstrate long wave instability, a solitary wave is the limit long wave of a family of periodic waves (see [7, 48] where solitary waves in falling films are discussed).

In Chapter 3, a detailed analysis of developing solitary waves in a gravity-driven flow, is aimed at providing guidance in detecting the corresponding families of periodic waves in interfacial microchannel flows. In addition, the wave velocities and shapes of the solitary waves and corresponding long periodic waves, are very similar, and hence the given results can be used to identify observed waves in future experimental works.

Now, shifting attention to the case of a pressure-driven flow, the pressure gradient imposed over the length of the channel is considered to be a free parameter, and is therefore specified in order to achieve a particular flow rate. This situation is more desirable for industrial and technological applications for several reasons . Firstly, since the restriction of the force of gravity no longer applies, a much wider range of flow rates can be considered. It is seen that the pressure gradient is a much more powerful and flexible tool which may be continually altered to maintain a particular flow rate in the channel, also facilitating the possibility of a feedback loop. In Chapter 2, it is shown that the pressure gradient may be found as a function of the interface location, potentially providing a radical way of determining wave regimes in experiments, which are otherwise very difficult to detect. The amplitudes of the waves found for the pressure-driven problem are much smaller than those in the case of the gravity-driven flow, typically just 0.01% of the width of the channel, hence the difficulty in observing them in experiments.

Typical flow regimes in microchannels of widths ranging from tens of nanometres to several hundred micrometers, and their applications, are reviewed by Günther and Jensen [20] and Hardt and Hahn [22]. The roles of the similarity parameters which characterise such flows are also discussed.

Experiments concerning interfacial flows of two immiscible liquids in narrow channels of sub-millimetre sizes, were carried out by Burns and Ramshaw [8]. For typical flow velocities between 2 cm s^{-1} to 20 cm s^{-1}, the Reynolds number varied in the range of 1 to 25. In most cases, stable co-current flows were observed, but increasing the ratio of liquid viscosities for example, led to flow instabilities.

The design of microchips utilising microchannel flows for continuous flow chemical processing is described by Tokeshi *et al.* [61]. Each microchip consisted of a few microchannels of dimensions 50 μm $\times$ 20 μm, 140 μm $\times$ 20 μm and 90 μm $\times$ 20 μm. It was noted that special guide structures were used to prevent interface instabilities inside the microchannels over a long distance.

The highest value of the Reynolds number in experiments by Maruyama *et al.* [31], with an enzymatic reaction in a two-phase flow, was lower than 50. Microchannels of various dimensions, namely 100 μm $\times$ 25 μm, 70 μm $\times$ 25 μm, 150 μm $\times$ 25 μm, 100 μm $\times$ 10 μm and 100 μm $\times$ 40 μm, were used. It is noted that a stable laminar flow can be achieved with suitable surface modification, and that the aspect ratio of the channel also affects the stability of the flow. Pohar *et al.* [38] found that the most favourable aspect ratio for parallel flow is 2, so that the diffusion distance has been minimised - an intuitive result for the case of waveless flow. Although the efficiency of mass transfer in parallel flows compared with other regimes, for example slug flow [16], has not been investigated, it seems intuitive that the highest mass transfer rate in parallel flows should be achieved with a flow with a wavy interface, as discussed previously. Despite this, the role of the interfacial instabilities has not been fully understood.

In addition to aspect ratio related investigations, experiments by Kashid *et al.* [26] examined the effects of channel geometry on the flow. In channels of various shaped cross sections, it was found that, at low flow rates slug flow occurred, and at higher flow rates parallel flows were observed, with wavy interface flows appearing between the two.

Experimental studies of immiscible fluids such as aqueous and oil solutions, were carried out by Guillot and Colin [19] in microchannels of sections 100 μm $\times$ 100 μm and 100 μm $\times$ 200 μm. The experimental data shows that, for example, decreasing the water flow rate at a fixed oil flow rate, changes the flow regime from a parallel flow, to a flow which breaks into droplets inside the microchannel. The authors noted that such transitions cannot be explained in terms of the capillary number.

Different flow regimes in microchannels with rectangular cross sections, 300 μm $\times$ 600 μm, were observed by Zhao *et al.* [67], and it was noted that a flow with a smooth interface transformed into a flow with a wavy interface when the flow rate was increased. The same group experimentally studied the mass transfer characteristics of immiscible liquids in a microchannel of the same size [68]. The experiments showed that the mass transfer rate strongly depended on the Reynolds number of the total mixture, which varied between 19 and 650. In particular, the dependence became non-linear as the Reynolds number passed a critical value, observed to be around 200, and this value corresponded to a transition from a parallel flow with smooth interface to a flow with a wavy interface.

In the experimental and theoretical work by Kockmann *et al.* [27], the mixing characteristics of the T-shaped junction were studied in a wide interval of the Reynolds number. It was observed that the flow was laminar and the streamlines were straight at Reynolds numbers less than 10, and by increasing this parameter, symmetrical vortex pairs appeared at the entrance of the mixing channel. As the Reynolds number exceeded a certain value between 120 and 300, depending on the channel geometry, the vortices subsided.

Two particular flow regimes, parallel flow and slug flow, were studied experimentally and theoretically by Pohar *et al.* [38]. In experiments, water and *n*-hexane were used in three rectangular microchannels, whose depths and widths were 50 μm $\times$ 220 μm, 50 μm $\times$ 440 μm and 100 μm $\times$ 1000 μm, respectively, and the Reynolds number ranged from 0.2 to 60. The authors presented a flow map combining two planes, namely the water

average velocity against the n-hexane average velocity, and the water flow rate against the n-hexane flow rate, where the domains of the parallel flow and slug flow were shown. Pohar *et al.* [38] concluded that the Weber number is not related to the transition from slug flow to parallel flow. However, Zhao *et al.* [67] had previously observed a range of flow regimes, including parallel and slug flow, as they gradually increased the Weber number. There are also theoretical papers analysing instability mechanisms in a two-layer Poiseuille flow, studied at values of the similarity parameters not reached in microchannels [54].

Although there are many works showing experimental observations of interfacial instabilities, there are no qualitative descriptions of observed wave shapes and quantitative parameters, such as their velocities, lengths and amplitudes.

For the pressure-driven problem, the approach developed by Sisoev *et al.* [52] and Sisoev and Bennett [49] is used by the same authors [50] to derive new evolution equations modelling very long waves on the interface of the considered microchannel flow. Analysis of these waves demonstrates that this flow also possesses many complex sets of periodic waves.

This rest of this Thesis is organised as follows: Chapter 2 discusses, in detail, the problem set-up and formulation of the governing mathematical model, Chapter 3 solves the specific case of a gravity-driven flow and Chapter 4 deals with the pressure-driven case, before conclusions are given in Chapter 5.

Chapter 2

Mathematical Model

2.1 Equations and boundary conditions

A plane flow of two immiscible incompressible viscous fluids [1], separated by an interface, in a microchannel of width H_c with rigid impermeable walls, is considered. To describe the flow, a two-dimensional Cartesian co-ordinate system (x, y) is introduced with the x-axis pointing in the direction of the flow along the bounding channel wall at $y = 0$, and the y-axis pointing into the channel interior. The velocity components u and v correspond to the x and y directions respectively. Denoting the interface as $y = h(x, t)$ where t is time, fluids in domains $y \in (0, h)$ and $y \in (h, H_c)$ are referred to as '1' and '2', respectively.

It suffices to study the problem in two-dimensions as a result of Squire's theorem which states that two-dimensional perturbations are more influential on the developing flow than three-dimensional perturbations. Furthermore, the approximation may be utilised for flows in channels with high aspect ratios, such as those found in typical experimental investigations discussed in Chapter 1 [61, 31, 38].

The microchannel flow is described by the Navier-Stokes system, accompanied by boundary conditions stated on both microchannel walls and on the fluid-fluid interface.

Firstly, on both channel walls, that is at $y = 0$ and $y = H_c$, no-slip conditions $u = 0$ are

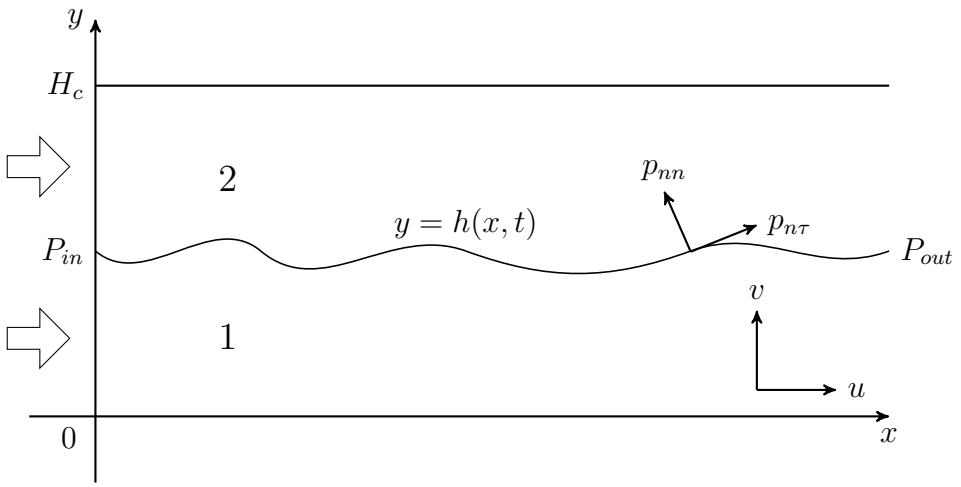

Figure 2.1: Two-layer interfacial microchannel flow

applied. Also, the channel walls are considered impermeable and so the normal velocity component should be zero, that is $v = 0$ at both $y = 0$ and $y = H_c$. These particular boundary conditions describe the absence of flux, in the y-direction, through the walls.

Secondly, there are a number of conditions regarding the fluid-fluid interface, $y = h(x,t)$. There should be no discontinuity in fluid velocities at the interface, hence the velocity components of each layer have a difference of zero here: $[u]_1^2 = 0$ and $[v]_1^2 = 0$, where $[u]_1^2$ denotes the jump in velocity component u across the interface. Regarding the stresses on the interface, there should be no discontinuity in tangential stress, $[p_{n\tau}]_1^2 = 0$, and the condition describing the normal stress is given by the recognisable Young-Laplace equation. This condition states that the jump in normal stress across the interface is proportional to the curvature, ζ, and the coefficient of proportionality is the surface tension, σ. Hence the relation, $[p_{nn}]_1^2 = \sigma\zeta$ is found. The final condition on the interface is given by the kinematic boundary condition which describes the fact that a liquid particle on the interface remains on the interface for all time. This condition is derived by considering the interface, described by the equation $y = h(x,t)$, and hence a particle located on the interface satisfies $y(t) = h(x(t),t)$. Now, differentiating with respect to t using the chain

rule, it is seen that

$$\frac{dy}{dt} = \frac{\partial h}{\partial x}\frac{dx}{dt} + \frac{\partial h}{\partial t},$$

which gives

$$v = \frac{\partial h}{\partial x}u + \frac{\partial h}{\partial t}. \tag{2.1}$$

Hence, the full system of equations and boundary conditions can be written as

$$\begin{aligned}
&\frac{\partial u}{\partial x} + \frac{\partial v}{\partial y} = 0, \\
&\frac{\partial u}{\partial t} + u\frac{\partial u}{\partial x} + v\frac{\partial u}{\partial y} = -\frac{1}{\rho^{(j)}}\frac{\partial p}{\partial x} + \nu^{(j)}\left(\frac{\partial^2 u}{\partial x^2} + \frac{\partial^2 u}{\partial y^2}\right) + g, \\
&\frac{\partial v}{\partial t} + u\frac{\partial v}{\partial x} + v\frac{\partial v}{\partial y} = -\frac{1}{\rho^{(j)}}\frac{\partial p}{\partial y} + \nu^{(j)}\left(\frac{\partial^2 v}{\partial x^2} + \frac{\partial^2 v}{\partial y^2}\right), \\
&y = 0, H_c: \quad u = 0, \quad v = 0, \\
&y = h(x,t): \quad \frac{\partial h}{\partial t} + u\frac{\partial h}{\partial x} = v, \quad [p_{nn}]_1^2 = \sigma\zeta, \quad [p_{n\tau}]_1^2 = 0, \\
&\qquad\qquad [u]_1^2 = 0, \quad [v]_1^2 = 0,
\end{aligned} \tag{2.2}$$

where $\rho^{(j)}$ and $\nu^{(j)}$ for $j = 1, 2$ are the densities and viscosities of the first and second layer liquids respectively, p is pressure, and g is the gravitational acceleration.

Normal and shear stresses, p_{nn} and $p_{n\tau}$ respectively, and the interface curvature $\zeta(x,t)$ are calculated as

$$\begin{aligned}
p_{nn} &= -p + 2\rho\nu\left[1 + \left(\frac{\partial h}{\partial x}\right)^2\right]^{-1}\left[\left(\frac{\partial h}{\partial x}\right)^2\frac{\partial u}{\partial x} + \frac{\partial v}{\partial y} - \frac{\partial h}{\partial x}\left(\frac{\partial u}{\partial y} + \frac{\partial v}{\partial x}\right)\right], \\
p_{n\tau} &= \rho\nu\left[1 + \left(\frac{\partial h}{\partial x}\right)^2\right]^{-1}\left[\left(1 - \left(\frac{\partial h}{\partial x}\right)^2\right)\left(\frac{\partial u}{\partial y} + \frac{\partial v}{\partial x}\right) + 2\frac{\partial h}{\partial x}\left(\frac{\partial v}{\partial y} - \frac{\partial u}{\partial x}\right)\right], \\
\zeta &= \left[1 + \left(\frac{\partial h}{\partial x}\right)^2\right]^{-\frac{3}{2}}\frac{\partial^2 h}{\partial x^2}.
\end{aligned}$$

The full system of equations and boundary conditions (2.2) has a steady flow solution

under a constant external pressure gradient, $\frac{dP}{dx}$. The steady flow solution is a completely parallel flow of the two fluids with an undisturbed, waveless interface. In other words, the first layer thickness is constant, $y = H$, for all time.

A solution of (2.2) such that the velocity of the flow does not depend on x and t, is found when all derivatives $\frac{\partial}{\partial t}$ and $\frac{\partial}{\partial x_\kappa}$ vanish. Furthermore, there is no velocity in the y-direction and so the corresponding velocity component is zero, $v = 0$. It is seen that the only terms which remain, result in the following reduction of the second equation from (2.2),

$$\frac{d^2U^{(j)}}{dy^2} = -\frac{1}{\rho^{(j)}\nu^{(j)}}\frac{dP}{dx}, \tag{2.3}$$

where the capital letters have been introduced to denote variables corresponding to the waveless flow. Equation (2.3) is integrated twice to give the following two relations,

$$\begin{aligned} U^{(1)} &= -\frac{1}{\rho^{(1)}\nu^{(1)}}\frac{dP}{dx}\frac{y^2}{2} + C_1 y + C_2, \\ U^{(2)} &= -\frac{1}{\rho^{(2)}\nu^{(2)}}\frac{dP}{dx}\frac{y^2}{2} + C_3 y + C_4, \end{aligned} \tag{2.4}$$

where C_i, for $i = 1, ..., 4$, are the constants of integration which arise. Equations (2.4) are solved simultaneously by applying the corresponding boundary conditions

$$\begin{aligned} y = 0 \quad &: \quad U^{(1)} = 0 \\ y = H_c \quad &: \quad U^{(2)} = 0 \\ y = H \quad &: \quad U^{(1)} = U^{(2)}, \\ &\qquad \rho^{(1)}\nu^{(1)}\frac{dU^{(1)}}{dy} = \rho^{(2)}\nu^{(2)}\frac{dU^{(2)}}{dy}. \end{aligned}$$

The resulting solution is given by

$$
\begin{aligned}
y \in [0, H] \quad &: \quad U^{(1)}(y) = \left(\frac{1}{\rho^{(1)}\nu^{(1)}} \frac{dP}{dx} - \frac{g}{\nu^{(1)}} \right) \frac{y^2}{2} + a^{(1)} y, \\
&\qquad V^{(1)} = 0, \\
&\qquad P^{(1)} = P, \\
y \in [H, H_c] \quad &: \quad U^{(2)}(y) = \left(\frac{1}{\rho^{(2)}\nu^{(2)}} \frac{dP}{dx} - \frac{g}{\nu^{(2)}} \right) \frac{y^2 - H_c^2}{2} + a^{(2)} (y - H_c), \\
&\qquad V^{(2)} = 0, \\
&\qquad P^{(2)} = P,
\end{aligned}
\tag{2.5}
$$

and contains the following constants

$$
\begin{aligned}
a^{(1)} &= -\frac{1}{2} \frac{\rho^{(2)}\nu^{(2)}}{\rho^{(1)}\nu^{(1)}} \frac{\frac{H_c^2 - H^2}{\rho^{(2)}\nu^{(2)}} + \frac{H^2}{\rho^{(1)}\nu^{(1)}}}{H_c - \left(1 - \frac{\rho^{(2)}\nu^{(2)}}{\rho^{(1)}\nu^{(1)}}\right) H} \frac{dP}{dx} \\
&\quad + \left(\frac{\rho^{(2)}\nu^{(2)}}{\rho^{(1)}\nu^{(1)}} \frac{\frac{H_c^2 - H^2}{2\nu^{(2)}} + \frac{H^2}{2\nu^{(1)}} + \frac{\rho^{(2)} - \rho^{(1)}}{\rho^{(1)}} \frac{H^2}{\nu^{(1)}}}{H_c - \left(1 - \frac{\rho^{(2)}\nu^{(2)}}{\rho^{(1)}\nu^{(1)}}\right) H} - \frac{\rho^{(2)} - \rho^{(1)}}{\rho^{(1)}\nu^{(1)}} H \right) g, \\
&= \frac{\rho^{(2)}\nu^{(2)}}{\rho^{(1)}\nu^{(1)}}\, a^{(2)} - \frac{\rho^{(2)} - \rho^{(1)}}{\rho^{(1)}\nu^{(1)}}\, gH \\
a^{(2)} &= \left[H_c - \left(1 - \frac{\rho^{(2)}\nu^{(2)}}{\rho^{(1)}\nu^{(1)}} \right) H \right]^{-1} \\
&\quad \times \left[-\frac{1}{2} \left(\frac{H_c^2 - H^2}{\rho^{(2)}\nu^{(2)}} + \frac{H^2}{\rho^{(1)}\nu^{(1)}} \right) \frac{dP}{dx} + g \left(\frac{H_c^2 - H^2}{2\nu^{(2)}} + \frac{H^2}{2\nu^{(1)}} + \frac{\rho^{(2)} - \rho^{(1)}}{\rho^{(1)}} \frac{H^2}{\nu^{(1)}} \right) \right].
\end{aligned}
$$

Flow rates of the first and second layers, $Q^{(1)}$ and $Q^{(2)}$, are found as

$$
\begin{aligned}
Q^{(1)} &\equiv \int_0^H U^{(1)} dy \\
&= \left(\frac{1}{\rho^{(1)}\nu^{(1)}} \frac{dP}{dx} - \frac{g}{\nu^{(1)}} \right) \frac{H^3}{6} + a^{(1)} \frac{H^2}{2}
\end{aligned}
$$

$$
\begin{aligned}
&= \left(\frac{H^3}{6\rho^{(1)}\nu^{(1)}} - \frac{H^2}{4}\frac{\rho^{(2)}\nu^{(2)}}{\rho^{(1)}\nu^{(1)}} \frac{\frac{H_c^2-H^2}{\rho^{(2)}\nu^{(2)}} + \frac{H^2}{\rho^{(1)}\nu^{(1)}}}{H_c - \left(1 - \frac{\rho^{(2)}\nu^{(2)}}{\rho^{(1)}\nu^{(1)}}\right) H} \right) \frac{dP}{dx} \\
&\quad + \left[-\frac{H^3}{6\nu^{(1)}} + \frac{H^2}{2} \left(\frac{\rho^{(2)}\nu^{(2)}}{\rho^{(1)}\nu^{(1)}} \frac{\frac{H_c^2-H^2}{2\nu^{(2)}} + \frac{H^2}{2\nu^{(1)}} + \frac{\rho^{(2)}-\rho^{(1)}}{\rho^{(1)}}\frac{H^2}{\nu^{(1)}}}{H_c - \left(1 - \frac{\rho^{(2)}\nu^{(2)}}{\rho^{(1)}\nu^{(1)}}\right) H} - \frac{\rho^{(2)}-\rho^{(1)}}{\rho^{(1)}\nu^{(1)}} H \right) \right] g,
\end{aligned}
$$

$$
\begin{aligned}
Q^{(2)} &\equiv \int_H^{H_c} U^{(2)} dy \\
&= \left(\frac{1}{\rho^{(2)}\nu^{(2)}} \frac{dP}{dx} - \frac{g}{\nu^{(2)}} \right) \frac{3H_c^2 H - H^3 - 2H_c^3}{6} \\
&\quad + a^{(2)} \frac{2H_c H - H_c^2 - H^2}{2} \\
&= \left(\frac{3H_c^2 H - H^3 - 2H_c^3}{6\rho^{(2)}\nu^{(2)}} - \frac{(2H_c H - H_c^2 - H^2)\left(\frac{H_c^2-H^2}{\rho^{(2)}\nu^{(2)}} + \frac{H^2}{\rho^{(1)}\nu^{(1)}}\right)}{4\left(H_c - \left(1 - \frac{\rho^{(2)}\nu^{(2)}}{\rho^{(1)}\nu^{(1)}}\right) H\right)} \right) \frac{dP}{dx} \\
&\quad + \left(-\frac{3H_c^2 H - H^3 - 2H_c^3}{6\nu^{(2)}} \right. \\
&\quad \left. + \frac{(2H_c H - H_c^2 - H^2)\left(\frac{H_c^2-H^2}{2\nu^{(2)}} + \frac{H^2}{2\nu^{(1)}} + \frac{\rho^{(2)}-\rho^{(1)}}{\rho^{(1)}}\frac{H^2}{\nu^{(1)}}\right)}{2\left(H_c - \left(1 - \frac{\rho^{(2)}\nu^{(2)}}{\rho^{(1)}\nu^{(1)}}\right) H\right)} \right) g.
\end{aligned}
$$

Summing the flow rates in the individual fluid layers, the total flow rate is given by

$$
\begin{aligned}
Q &\equiv Q^{(1)} + Q^{(2)} \\
&= \left[\frac{H^3}{6\rho^{(1)}\nu^{(1)}} + \frac{3H_c^2 H - H^3 - 2H_c^3}{6\rho^{(2)}\nu^{(2)}} \right. \\
&\quad \left. - \frac{\left(\frac{\rho^{(2)}\nu^{(2)}}{\rho^{(1)}\nu^{(1)}} H^2 + 2H_c H - H_c^2 - H^2\right)\left(\frac{H_c^2-H^2}{\rho^{(2)}\nu^{(2)}} + \frac{H^2}{\rho^{(1)}\nu^{(1)}}\right)}{4\left[H_c - \left(1 - \frac{\rho^{(2)}\nu^{(2)}}{\rho^{(1)}\nu^{(1)}}\right) H\right]} \right] \frac{dP}{dx} \\
&\quad + \left[\frac{\left(\frac{\rho^{(2)}\nu^{(2)}}{\rho^{(1)}\nu^{(1)}} H^2 + 2H_c H - H_c^2 - H^2\right)\left(\frac{H_c^2-H^2}{2\nu^{(2)}} + \frac{H^2}{2\nu^{(1)}} + \frac{\rho^{(2)}-\rho^{(1)}}{\rho^{(1)}}\frac{H^2}{\nu^{(1)}}\right)}{2\left[H_c - \left(1 - \frac{\rho^{(2)}\nu^{(2)}}{\rho^{(1)}\nu^{(1)}}\right) H\right]} \right. \\
&\quad \left. - \left(\frac{H^3}{6\nu^{(1)}} + \frac{3H_c^2 H - H^3 - 2H_c^3}{6\nu^{(2)}} + \frac{\rho^{(2)}-\rho^{(1)}}{\rho^{(1)}} \frac{H^3}{2\nu^{(1)}} \right) \right] g.
\end{aligned}
$$

It is now required for the system (2.2) to be non-dimensionalised. Using the average

fluid velocity over the channel width as the scaling parameter, $U_c = \dfrac{Q_c}{H_c}$, where Q_c is the total flow rate, dimensionless variables are introduced with the following replacements,

$$\begin{aligned} x &\to H_c x, & y &\to H_c y, \\ h &\to H_c h, & t &\to \frac{H_c t}{U_c}, \\ u &\to U_c u, & v &\to U_c v, \\ p &\to \rho^{(1)} U_c^2 p. \end{aligned}$$

The system of equations (2.2) may now be written in dimensionless form,

$$\begin{aligned} &\frac{\partial u}{\partial x} + \frac{\partial v}{\partial y} = 0, \\ &\frac{\partial u}{\partial t} + u\frac{\partial u}{\partial x} + v\frac{\partial u}{\partial y} = -\frac{1}{\rho_0^{(j)}}\frac{\partial p}{\partial x} + \frac{\nu_0^{(j)}}{\mathrm{Re}}\left(\frac{\partial^2 u}{\partial x^2} + \frac{\partial^2 u}{\partial y^2}\right) + \frac{1}{\mathrm{Fr}^2}, \\ &\frac{\partial v}{\partial t} + u\frac{\partial v}{\partial x} + v\frac{\partial v}{\partial y} = -\frac{1}{\rho_0^{(j)}}\frac{\partial p}{\partial y} + \frac{\nu_0^{(j)}}{\mathrm{Re}}\left(\frac{\partial^2 v}{\partial x} + \frac{\partial^2 v}{\partial y^2}\right), \\ &y = 0, 1: \quad u = 0, \quad v = 0, \\ &y = h\,(x,t): \quad \frac{\partial h}{\partial t} + u\frac{\partial h}{\partial x} = v, \quad [p_{nn}]_1^2 + \frac{\zeta}{\mathrm{We}} = 0, \quad [p_{n\tau}]_1^2 = 0, \\ &\qquad\qquad [u]_1^2 = 0, \quad [v]_1^2 = 0, \end{aligned} \tag{2.6}$$

with normal and tangential stresses, and curvature, given by

$$\begin{aligned} p_{nn} &= -p + \frac{2\rho_0^{(j)}\nu_0^{(j)}}{\mathrm{Re}}\left[1 + \left(\frac{\partial h}{\partial x}\right)^2\right]^{-1}\left[\left(1 - \left(\frac{\partial h}{\partial x}\right)^2\right)\frac{\partial v}{\partial x} - \frac{\partial h}{\partial x}\left(\frac{\partial u}{\partial y} + \frac{\partial v}{\partial x}\right)\right], \\ p_{n\tau} &= \frac{\rho_0^{(j)}\nu_0^{(j)}}{\mathrm{Re}}\left[1 + \left(\frac{\partial h}{\partial x}\right)^2\right]^{-1}\left[\left(1 - \left(\frac{\partial h}{\partial x}\right)^2\right)\left(\frac{\partial u}{\partial y} + \frac{\partial v}{\partial x}\right) + 4\frac{\partial h}{\partial x}\frac{\partial v}{\partial y}\right], \\ \zeta &= \left[1 + \left(\frac{\partial h}{\partial x}\right)^2\right]^{-\frac{3}{2}}\frac{\partial^2 h}{\partial x^2}. \end{aligned}$$

The notations $\rho_0^{(j)}$ and $\nu_0^{(j)}$ have been introduced to represent the ratio of densities and viscosities. In particular $\rho_0^{(1)} = 1$, $\rho_0^{(2)} = \rho_0$, $\nu_0^{(1)} = 1$ and $\nu_0^{(2)} = \nu_0$. Hence, the system (2.6) contains the following dimensionless parameters

$$\mathrm{Re} = \frac{U_c H_c}{\nu^{(1)}}, \quad \mathrm{Fr}^2 = \frac{U_c^2}{g H_c}, \quad \mathrm{We} = \frac{\rho^{(1)} U_c^2 H_c}{\sigma}, \quad \rho_0 = \frac{\rho^{(2)}}{\rho^{(1)}}, \quad \nu_0 = \frac{\nu^{(2)}}{\nu^{(1)}}. \quad (2.7)$$

The steady flow solution (2.5) may now be re-written as

$$\begin{aligned}
y \in [0, H] \quad &: \quad U^{(1)}(y) = \mathrm{Re}\left(\frac{dP}{dx} - \frac{1}{\mathrm{Fr}^2}\right)\frac{y^2}{2} + a^{(1)} y, \qquad (2.8)\\
&\qquad V^{(1)} = 0,\\
&\qquad P^{(1)} = P,\\
y \in [H, 1] \quad &: \quad U^{(2)}(y) = \frac{\mathrm{Re}}{\nu_0}\left(\frac{1}{\rho_0}\frac{dP}{dx} - \frac{1}{\mathrm{Fr}^2}\right)\frac{y^2 - 1}{2} + a^{(2)}(y - 1),\\
&\qquad V^{(2)} = 0,\\
&\qquad P^{(2)} = P,
\end{aligned}$$

where the constants are given by

$$\begin{aligned}
a^{(1)} &= \left[(1 - \rho_0) H + \rho_0 \frac{1 - (1 - \nu_0) H^2 - 2\nu_0 (1 - \rho_0) H^2}{2\left[1 - (1 - \rho_0 \nu_0) H\right]}\right]\frac{\mathrm{Re}}{\mathrm{Fr}^2}\\
&\quad - \frac{1 - (1 - \rho_0 \nu_0) H^2}{2\left[1 - (1 - \rho_0 \nu_0) H\right]}\,\mathrm{Re}\frac{dP}{dx},\\
a^{(2)} &= \frac{1 - (1 - \nu_0) H^2 - 2\nu_0 (1 - \rho_0) H^2}{2\nu_0\left[1 - (1 - \rho_0 \nu_0) H\right]}\,\frac{\mathrm{Re}}{\mathrm{Fr}^2} - \frac{1 - (1 - \rho_0 \nu_0) H^2}{2\rho_0 \nu_0\left[1 - (1 - \rho_0 \nu_0) H\right]}\,\mathrm{Re}\frac{dP}{dx}.
\end{aligned}$$

Dimensionless flow rates, $Q^{(1)}$ and $Q^{(2)}$, now become

$$\begin{aligned}
Q^{(1)} &= \int_0^H U^{(1)} dy \qquad (2.9)\\
&= \mathrm{Re}\left(\frac{dP}{dx} - \frac{1}{\mathrm{Fr}^2}\right)\frac{H^3}{6} + a^{(1)}\frac{H^2}{2}
\end{aligned}$$

$$
\begin{aligned}
&= \frac{\mathrm{Re}}{\mathrm{Fr}^2} H^2 \left[\left(\frac{1}{3} - \frac{\rho_0}{2} \right) H + \rho_0 \frac{1 - (1-\nu_0) H^2 - 2\nu_0 (1-\rho_0) H^2}{4 \left[1 - (1 - \rho_0 \nu_0) H \right]} \right] \\
&\quad + \mathrm{Re} \frac{dP}{dx} H^2 \left[\frac{H}{6} - \frac{1 - (1 - \rho_0 \nu_0) H^2}{4 \left[1 - (1 - \rho_0 \nu_0) H \right]} \right], \\
Q^{(2)} &= \int_H^1 U^{(2)} dy \\
&= \mathrm{Re} \left(\frac{1}{\rho_0 \nu_0} \frac{dP}{dx} - \frac{1}{\nu_0 \mathrm{Fr}^2} \right) \frac{3H - H^3 - 2}{6} + a^{(2)} \frac{2H - 1 - H^2}{2} \\
&= \frac{\mathrm{Re}}{\nu_0 \mathrm{Fr}^2} \left[\frac{2 - 3H + H^3}{6} + \frac{(2H - 1 - H^2) \left[1 - (1-\nu_0) H^2 - 2\nu_0 (1-\rho_0) H^2 \right]}{4 \left[1 - (1 - \rho_0 \nu_0) H \right]} \right] \\
&\quad - \frac{\mathrm{Re}}{\rho_0 \nu_0} \frac{dP}{dx} \left[\frac{2 - 3H + H^3}{6} + \frac{(2H - 1 - H^2) \left[1 - (1 - \rho_0 \nu_0) H^2 \right]}{4 \left[1 - (1 - \rho_0 \nu_0) H \right]} \right],
\end{aligned}
$$

and the total flow rate is found by summing $Q^{(1)}$ and $Q^{(2)}$ from (2.9),

$$
\begin{aligned}
Q &\equiv Q^{(1)} + Q^{(2)} \\
&= \varphi_1 (\rho_0, \nu_0, H) \frac{\mathrm{Re}}{\mathrm{Fr}^2} + \varphi_2 (\rho_0, \nu_0, H) \, \mathrm{Re} \frac{dP}{dx},
\end{aligned} \tag{2.10}
$$

where

$$
\begin{aligned}
\varphi_1 (\rho_0, \nu_0, H) &= H^2 \left[\left(\frac{1}{3} - \frac{\rho_0}{2} \right) H + \rho_0 \frac{1 - (1-\nu_0) H^2 - 2\nu_0 (1-\rho_0) H^2}{4 \left[1 - (1 - \rho_0 \nu_0) H \right]} \right] \\
&\quad + \frac{1}{\nu_0} \left[\frac{2 - 3H + H^3}{6} \right. \\
&\quad \left. + \frac{(2H - 1 - H^2) \left[1 - (1-\nu_0) H^2 - 2\nu_0 (1-\rho_0) H^2 \right]}{4 \left[1 - (1 - \rho_0 \nu_0) H \right]} \right], \\
\varphi_2 (\rho_0, \nu_0, H) &= H^2 \left[\frac{H}{6} - \frac{1 - (1 - \rho_0 \nu_0) H^2}{4 \left[1 - (1 - \rho_0 \nu_0) H \right]} \right] \\
&\quad - \frac{1}{\rho_0 \nu_0} \left[\frac{2 - 3H + H^3}{6} + \frac{(2H - 1 - H^2) \left[1 - (1 - \rho_0 \nu_0) H^2 \right]}{4 \left[1 - (1 - \rho_0 \nu_0) H \right]} \right].
\end{aligned} \tag{2.11}
$$

Since the velocity scale, U_c, has been chosen as the average velocity in the channel, then the total flow rate is given by $Q = 1$. The Reynolds number may now be found using

(2.10),

$$\mathrm{Re} = \frac{1}{\varphi_1 \frac{1}{\mathrm{Fr}^2} + \varphi_2 \frac{dP}{dx}}. \tag{2.12}$$

The relation (2.12) allows the velocity scale in dimensional form to be calculated as

$$U_c = \frac{H_c^2}{\nu^{(1)}} \left(\varphi_1 g + \frac{\varphi_2}{\rho^{(1)}} \frac{d\tilde{P}}{d\tilde{x}} \right). \tag{2.13}$$

The relations derived above can be shown to reduce to the case of a falling film[1].

The final step of the problem formulation is to stretch the scales of x and t. A stretch of co-ordinates is applied for convenience when seeking solutions in the form of long waves as their length scale is much larger than the scale of the microchannel. The stretching parameter κ is applied to variables x and t, and hence v, and are denoted with subscript κ as follows,

$$x_\kappa = \kappa x, \qquad t_\kappa = \kappa t, \qquad v_\kappa = \frac{v}{\kappa}. \tag{2.14}$$

Applying the scaling (2.14) to the system (2.6), the system of stretched dimensionless Navier-Stokes equations and relevant boundary conditions is attained,

$$\begin{aligned}
&\frac{\partial u}{\partial x_\kappa} + \frac{\partial v_\kappa}{\partial y} = 0, \\
&\frac{\partial u}{\partial t_\kappa} + u\frac{\partial u}{\partial x_\kappa} + v_\kappa \frac{\partial u}{\partial y} = -\frac{1}{\rho_0^{(j)}} \frac{\partial p}{\partial x_\kappa} + \frac{\nu_0^{(j)}}{\kappa \mathrm{Re}} \left(\kappa^2 \frac{\partial^2 u}{\partial x_\kappa^2} + \frac{\partial^2 u}{\partial y^2} \right) + \frac{1}{\kappa \mathrm{Fr}^2}, \\
&\kappa^2 \left(\frac{\partial v_\kappa}{\partial t_\kappa} + u\frac{\partial v_\kappa}{\partial x_\kappa} + v_\kappa \frac{\partial v_\kappa}{\partial y} \right) = -\frac{1}{\rho_0^{(j)}} \frac{\partial p}{\partial y} + \frac{\kappa^2 \nu_0^{(j)}}{\kappa \mathrm{Re}} \left(\kappa^2 \frac{\partial^2 v_\kappa}{\partial x_\kappa^2} + \frac{\partial^2 v_\kappa}{\partial y^2} \right), \\
&y = 0: \quad u = 0, \quad v_\kappa = 0,
\end{aligned} \tag{2.15}$$

[1] If $\rho_0 = 0$, $H = 1$ and $\frac{dP}{dx} = 0$, it follows that

$$U^{(1)} = \frac{\mathrm{Re}}{\mathrm{Fr}^2} \left(Hy - \frac{y^2}{2} \right), \quad Q^{(1)} = \frac{\mathrm{Re}}{3\mathrm{Fr}^2},$$

and also $\varphi_1 = \frac{1}{3}$. If an average velocity scale is used, then $Q^{(1)} = 1$ or $U_c = \frac{gH_c^2}{3\nu^{(1)}}$.

$$
\begin{aligned}
y = h\left(x_\kappa, t_\kappa\right): \quad & \frac{\partial h}{\partial t_\kappa} + u\frac{\partial h}{\partial x_\kappa} = v_\kappa, \quad [p_{nn}]_1^2 + \frac{\kappa^2\zeta_\kappa}{\mathrm{We}} = 0, \quad [p_{n\tau}]_1^2 = 0, \\
& [u]_1^2 = 0, \quad [v_\kappa]_1^2 = 0, \\
y = 1: \quad & u = 0, \quad v_\kappa = 0.
\end{aligned}
$$

The normal stress p_{nn}, tangential stress $p_{n\tau}$ and the interface curvature ζ_κ are calculated as follows,

$$
\begin{aligned}
p_{nn} &= -p + \frac{2\kappa^2\rho_0^{(j)}\nu_0^{(j)}}{\kappa d^2 \mathrm{Re}}\left[\left(1 - \kappa^2\left(\frac{\partial h}{\partial x_\kappa}\right)^2\right)\frac{\partial v_\kappa}{\partial y} - \frac{\partial h}{\partial x_\kappa}\left(\frac{\partial u}{\partial y} + \kappa^2\frac{\partial v_\kappa}{\partial x_\kappa}\right)\right], \\
p_{n\tau} &= \frac{\rho_0^{(j)}\nu_0^{(j)}}{d^2\mathrm{Re}}\left[\left(1 - \kappa^2\left(\frac{\partial h}{\partial x_\kappa}\right)^2\right)\left(\frac{\partial u}{\partial y} + \kappa^2\frac{\partial v_\kappa}{\partial x_\kappa}\right) + 4\kappa^2\frac{\partial h}{\partial x_\kappa}\frac{\partial v_\kappa}{\partial y}\right], \\
\zeta_\kappa &= \frac{1}{d^3}\frac{\partial^2 h}{\partial x_\kappa^2}, \quad d = \sqrt{1 + \kappa^2\left(\frac{\partial h}{\partial x_\kappa}\right)^2}.
\end{aligned}
$$

The governing equations (2.15) are now applied in order to investigate two individual cases of the considered microchannel flow. Firstly, the case of a solely gravity-driven flow is considered, followed by an investigation into a pressure-driven flow.

2.2 Gravity-driven two-layer microchannel flow

2.2.1 Steady flow solution

The considered microchannel flow, driven only by the force of gravity, is discussed in this section. The model outlined below was first derived by Sisoev *et al.* [52], to study steady-travelling periodic waves. Here, the model is formulated so that it may be utilised in Chapter 3, where steady-travelling solitary and transitional wave solutions are sought.

Since pressure is included as its gradient only, in the specific case of the gravity-driven flow, the accuracy of the pressure term may be defined as a constant so that its derivative vanishes. Hence, the pressure constant is chosen to be zero, $P = 0$. Therefore, the steady

flow solution (2.8), for the gravity-driven case is given by,

$$
\begin{aligned}
y \in [0, H]: \quad & V^{(1)} = 0, \quad P^{(1)} = 0, \\
& U^{(1)}(y) = \frac{\mathrm{Re}}{\mathrm{Fr}^2} y \left[(1-\rho_0) H + \rho_0 \frac{1-(1-\nu_0) H^2 - 2\nu_0 (1-\rho_0) H^2}{2\left[1-(1-\rho_0\nu_0) H\right]} - \frac{y}{2} \right], \\
y \in [H, 1]: \quad & V^{(2)} = 0, \quad P^{(2)} = 0, \\
& U^{(2)}(y) = \frac{\mathrm{Re}}{\mathrm{Fr}^2} (y-1) \left[\frac{1-(1-\nu_0) H^2 - 2\nu_0 (1-\rho_0) H^2}{2\nu_0 \left[1-(1-\rho_0\nu_0) H\right]} - \frac{y+1}{2\nu_0} \right].
\end{aligned} \tag{2.16}
$$

The flow rates of the first and second layers are given as a reduction of the expressions given in the general case (2.9),

$$
\begin{aligned}
Q^{(1)} &= \frac{\mathrm{Re}}{\mathrm{Fr}^2} H^2 \left[\left(\frac{1}{3} - \frac{\rho_0}{2} \right) H + \rho_0 \frac{1-(1-\nu_0) H^2 - 2\nu_0 (1-\rho_0) H^2}{4\left[1-(1-\rho_0\nu_0) H\right]} \right], \\
Q^{(2)} &= \frac{\mathrm{Re}}{\nu_0 \mathrm{Fr}^2} \left[\frac{2-3H+H^3}{6} + \frac{(2H-1-H^2)\left[1-(1-\nu_0) H^2 - 2\nu_0 (1-\rho_0) H^2\right]}{4\left[1-(1-\rho_0\nu_0) H\right]} \right],
\end{aligned}
$$

and hence the total flow rate of the waveless flow (2.10) is reduced to

$$
Q \equiv \int_0^1 U dy = \varphi_1 \frac{\mathrm{Re}}{\mathrm{Fr}^2} = 1,
$$

where the function φ_1 is given in (2.11). Therefore, it is seen that

$$
\mathrm{Fr}^2 = \varphi_1 \mathrm{Re}. \tag{2.17}
$$

Furthermore, the velocity scale (2.13) also reduces to

$$
U_c = \frac{\varphi_1 g H_c^2}{\nu^{(1)}}. \tag{2.18}
$$

2.2.2 Similarity parameters

In the thin film theory, the Reynolds number, Re, and the Weber number, We, are replaced with the film parameter, δ, and the Kapitza number, Ka, [12]. The parameter δ is a normalised Reynolds number and the Kapitza number, named after the pioneering Soviet scientist following his work on falling films [25], depends on the physical properties of a given liquid and the force of gravity, g. The advantage of the Kapitza number is that it does not depend on the flow rate, which is unknown at this stage. The aforementioned parameters can be defined for the microchannel flow as

$$\delta = \frac{1}{45\left(\nu^{(1)}\right)^2}\left(\frac{\rho^{(1)} g^4 \left(H_c^{(1)}\right)^{11}}{\sigma}\right)^{\frac{1}{3}}, \quad \mathrm{Ka} = \frac{\sigma}{\rho^{(1)}\left[g\left(\nu^{(1)}\right)^4\right]^{\frac{1}{3}}}, \tag{2.19}$$

where $H_c^{(1)} = H_c H$ is the dimensional thickness of the first layer in the waveless solution (2.16). Then, the Reynolds number and the Weber number are easily calculated from (2.7),

$$\mathrm{Re} = (45\delta)^{\frac{9}{11}}\,\mathrm{Ka}^{\frac{3}{11}}\frac{\varphi_1}{H^3}, \quad \mathrm{We} = \frac{(45\delta)^{\frac{15}{11}}}{\mathrm{Ka}^{\frac{6}{11}}}\frac{\varphi_1^2}{H^5}.$$

Finally, it is seen that the system (2.15) is governed by the following five parameters: δ, Ka, ρ_0, ν_0 and H. In other words, to find the similarity parameters for a given microchannel flow, it is necessary to compute the ratios ρ_0 and ν_0 using (2.7), the film parameter δ and the Kapitza number Ka using (2.19), and the relative thickness of the first layer $H = \dfrac{H_c^{(1)}}{H_c}$.

The regular waves stimulated by such capillary flows are the result of a balance of viscous, gravitational and capillary forces. The relationship between these forces may be

formulated in the following way,

$$\frac{\gamma}{\kappa \mathrm{Re}} = \frac{1}{\kappa \mathrm{Fr}^2}, \quad \frac{\gamma}{\kappa \mathrm{Re}} = \frac{\kappa^2}{\mathrm{We}}, \tag{2.20}$$

where γ is the scale constant. These equalities allow the constants γ and κ to be found,

$$\gamma = \frac{1}{\varphi_1}, \quad \kappa = \left(\frac{\rho^{(1)} g H_c^2}{\sigma}\right)^{\frac{1}{3}} = \frac{(45\delta)^{\frac{2}{11}}}{\mathrm{Ka}^{\frac{3}{11}} H^{\frac{2}{3}}}. \tag{2.21}$$

2.2.3 Linear stability analysis: eigenvalue problem

The stability of the waveless flow solution (2.16), of the full Navier-Stokes system, can be investigated by considering the corresponding Orr-Sommerfeld problem. The Orr-Sommerfeld equation [36, 37, 53], named after William Orr and Arnold Sommerfeld, is an eigenvalue equation which determines the sufficient conditions for instability of the waveless flow solution.

In order to carry out the linear stability analysis, a solution of (2.15) is sought by applying a small perturbation to the steady flow solution,

$$\begin{aligned} u(x,y,t) &= U(y) + \widehat{u}(x,y,t), \qquad v(x,y,t) = \widehat{v}(x,y,t), \\ p(x,y,t) &= \widehat{p}(x,y,t), \qquad h(x,t) = H + \widehat{h}(x,t), \end{aligned} \tag{2.22}$$

where hats denote small perturbations. Having substituted the perturbed variables (2.22) into (2.15), the system becomes

$$\begin{aligned} &\frac{\partial \widehat{u}}{\partial x} + \frac{\partial \widehat{v}}{\partial y} = 0, \\ &\frac{\partial \widehat{u}}{\partial t} + U\frac{\partial \widehat{u}}{\partial x} + U'\widehat{v} = -\frac{1}{\rho_0^{(j)}}\frac{\partial \widehat{p}}{\partial x} + \frac{\nu_0^{(j)}}{\mathrm{Re}}\left(\frac{\partial^2 \widehat{u}}{\partial x^2} + \frac{\partial^2 \widehat{u}}{\partial y^2}\right), \end{aligned} \tag{2.23}$$

$$
\begin{aligned}
&\frac{\partial \widehat{v}}{\partial t} + U\frac{\partial \widehat{v}}{\partial x} = -\frac{1}{\rho_0^{(j)}}\frac{\partial \widehat{p}}{\partial y} + \frac{\nu_0^{(j)}}{\mathrm{Re}}\left(\frac{\partial^2 \widehat{v}}{\partial x^2} + \frac{\partial^2 \widehat{v}}{\partial y^2}\right),\\
&y = 0: \quad \widehat{u} = 0, \quad \widehat{v} = 0,\\
&y = H: \quad \frac{\partial \widehat{h}}{\partial t} + U\frac{\partial \widehat{h}}{\partial x} = \widehat{v},\\
&\qquad \left[U'\widehat{h} + \widehat{u}\right]_1^2 = 0, \quad [\widehat{v}] = 0,\\
&\qquad \left[-\widehat{p} - P'\widehat{h} + \frac{2\rho_0^{(j)}\nu_0^{(j)}}{\mathrm{Re}}\left(\frac{\partial \widehat{v}}{\partial y} - U'\frac{\partial \widehat{h}}{\partial x}\right)\right]_1^2 + \frac{1}{\mathrm{We}}\frac{\partial^2 \widehat{h}}{\partial x^2} = 0,\\
&\qquad \left[\rho_0^{(j)}\nu_0^{(j)}\left(\frac{\partial \widehat{u}}{\partial y} + \frac{\partial \widehat{v}}{\partial x} + U''\widehat{h}\right)\right]_1^2 = 0,\\
&y = 1: \quad \widehat{u} = 0, \quad \widehat{v} = 0.
\end{aligned}
$$

In general, the linearised system (2.23) depending only on y, has a solution in the form of a travelling wave. Using a solution for normal modes,

$$
\left(\widehat{u}(x,y,t), \widehat{v}(x,y,t), \widehat{p}(x,y,t), \widehat{h}(x,t)\right) = \left(\check{u}(y), \check{v}(y), \check{p}(y), \check{h}\right) e^{i\alpha(x-ct)},
$$

the system for amplitude functions, $\check{u}(y)$, $\check{v}(y)$, $\check{p}(y)$ and $\check{h}$ is given by

$$
\begin{aligned}
&i\alpha\check{u} + \check{v}' = 0, \qquad (2.24)\\
&i\alpha\left(U - c\right)\check{u} + U'\check{v} = -\frac{i\alpha}{\rho_0^{(j)}}\check{p} + \frac{\nu_0^{(j)}}{\mathrm{Re}}\left(\check{u}'' - \alpha^2\check{u}\right),\\
&i\alpha\left(U - c\right)\check{v} = -\frac{1}{\rho_0^{(j)}}\check{p}' + \frac{\nu_0^{(j)}}{\mathrm{Re}}\left(\check{v}'' - \alpha^2\check{v}\right),\\
&y = 0: \quad \check{u} = 0, \quad \check{v} = 0,\\
&y = H: \quad i\alpha\left(U - c\right)\check{h} = \check{v},\\
&\qquad \left[U'\check{h} + \check{u}\right]_1^2 = 0, \quad \left[\check{v}\right]_1^2 = 0,\\
&\qquad \left[-\check{p} - P'\check{h} + \frac{2\rho_0^{(j)}\nu_0^{(j)}}{\mathrm{Re}}\left(\check{v}' - i\alpha U'\check{h}\right)\right]_1^2 - \frac{\alpha^2}{\mathrm{We}}\check{h} = 0,\\
&\qquad \left[\rho_0^{(j)}\nu_0^{(j)}\left(\check{u}' + i\alpha\check{v} + U''\check{h}\right)\right]_1^2 = 0,
\end{aligned}
$$

$$y = 1: \quad \check{u} = 0, \quad \check{v} = 0.$$

In order to find the Orr-Sommerfeld eigenvalue equation, a manipulation of the equations of system (2.24) is required. The initial step is to rearrange the first equation from system (2.24) for $\check{u}$,

$$\check{u} = -\frac{\check{v}'}{i\alpha},$$

or

$$\check{u} = \frac{i}{\alpha}\check{v}'. \tag{2.25}$$

Now, replacing (2.25) into the second equation from (2.24) and rearranging for $\check{p}$, it is seen that

$$\check{p} = \frac{\rho_0^{(j)}\nu_0^{(j)}}{\alpha^2 \mathrm{Re}}\check{v}''' - \rho_0^{(j)}\left[\frac{i}{\alpha}(U-c) + \frac{\nu_0^{(j)}}{\mathrm{Re}}\right]\check{v}' + \frac{i\rho_0^{(j)}}{\alpha}U'\check{v}. \tag{2.26}$$

Subsequently replacing (2.26) into the third equation from (2.24) and also noting that

$$i\alpha\left[U(H) - c\right]\check{h} = \check{v}(H), \tag{2.27}$$

the following eigenvalue problem is found,

$$\begin{aligned}
&\check{v}'''' - 2\alpha^2\check{v}'' + \alpha^4\check{v} - \frac{i\alpha\mathrm{Re}}{\nu_0^{(j)}}\left[(U-c)(\check{v}'' - \alpha^2\check{v}) - U''\check{v}\right] = 0, \qquad (2.28)\\
&y = 0: \quad \check{v} = 0, \quad \check{v}' = 0,\\
&y = H: \quad [\check{v}]_1^2 = 0,\\
&\qquad \left[\check{v}' - \frac{U'}{U-c}\check{v}\right]_1^2 = 0,\\
&\qquad \left[\rho_0^{(j)}\nu_0^{(j)}\left(\check{v}''' - \left(3\alpha^2 + \frac{i\alpha\mathrm{Re}}{\nu_0^{(j)}}(U-c)\right)\check{v}'\right.\right.\\
&\qquad\quad \left.\left. + \left(\frac{i\alpha\mathrm{Re}U'}{\nu_0^{(j)}} + \frac{2\alpha^2U'}{U-c} - \frac{i\alpha\mathrm{Re}P'}{\rho_0^{(j)}\nu_0^{(j)}(U-c)}\right)\check{v}\right)\right]_1^2 - \frac{i\alpha\mathrm{Re}}{\mathrm{We}(U-c)}\check{v} = 0,
\end{aligned}$$

$$\left[\rho_0^{(j)}\nu_0^{(j)}\left(\check{v}''+\left(\alpha^2-\frac{U''}{U-c}\right)\check{v}\right)\right]_1^2=0,$$

$$y=1: \quad \check{v}=0, \quad \check{v}'=0.$$

This eigenvalue problem is used to find the complex velocity $c=c_r+ic_i$, and the perturbation amplitude v. The system (2.28), depending on the similarity parameters ρ_0, ν_0, δ, Ka, H and the wavenumber α, was solved numerically for the gravity-driven problem by Sisoev *et al.* [52], in order to verify the approximate evolution system shown below.

2.2.4 Long wave approximation

It was shown by Shkadov and Sisoev [46, 48], that the square of the stretching parameter attains a very small value, $\kappa^2 \ll 1$, in most experiments concerning falling films, due to the strong surface tension. Indeed, many studies into falling film problems have successfully applied the approximation that $\kappa^2 \ll 1$ in order to reduce the governing system of equations [44, 46, 12, 48, 10]. It is reasonable to make similar estimations for the case of a two-layer microchannel flow when the microchannel width is sufficiently small since, as described above, the flow may be considered as a flow of two falling films sharing the same interface. Having introduced the coefficient $b=\dfrac{9\varphi^2}{H^{\frac{11}{3}}}$, the relation $\dfrac{\gamma}{\kappa\mathrm{Re}}=(5\delta b)^{-1}$ may also be written. Then, having neglected terms of order $O(\kappa^2)$, the system (2.15) is reduced to the following,

$$\begin{aligned}
&\frac{\partial u}{\partial x_\kappa}+\frac{\partial v_\kappa}{\partial y}=0, \quad \frac{\partial p}{\partial y}=0, \qquad (2.29)\\
&\frac{\partial u}{\partial t_\kappa}+u\frac{\partial u}{\partial x_\kappa}+v_\kappa\frac{\partial u}{\partial y}=-\frac{1}{\rho_0^{(j)}}\frac{\partial p}{\partial x_\kappa}+\frac{\nu_0^{(j)}}{5\delta b\gamma}\frac{\partial^2 u}{\partial y^2}+\frac{1}{\kappa\mathrm{Fr}^2},\\
&y=0,1: \quad u=0, \quad v_\kappa=0,\\
&y=h(x_\kappa,t_\kappa): \quad \frac{\partial h}{\partial t_\kappa}+u\frac{\partial h}{\partial x_\kappa}=v_\kappa, \quad [p]_1^2-\frac{1}{5\delta b}\frac{\partial^2 h}{\partial x_\kappa^2}=0,\\
&\qquad\qquad \left[\rho_0^{(j)}\nu_0^{(j)}\frac{\partial u}{\partial y}\right]_1^2=0, \quad [u]_1^2=0, \quad [v_\kappa]_1^2=0.
\end{aligned}$$

The accuracy of the model relies on the assumption that $\kappa^2 \ll 1$. Obviously, the closer the attained value of κ^2 is to zero, the more accurate the developed model is at describing the full Navier-Stokes problem.

2.2.5 Integral method and evolution equations

Simplification of the system (2.29) utilises two steps successfully applied in the film theory, for example, by Shkadov and Sisoev [48] and Sisoev and Çekiç [10], a method pioneered by Shkadov [44]. The initial step is to apply the so-called integral method, which involves integrating the continuity and x-momentum equations from (2.29) across the respective liquid layers.

Firstly, integrating the continuity equation over the first layer yields

$$\int_0^{h(x,t)} \left(\frac{\partial u^{(1)}}{\partial x_\kappa} + \frac{\partial v_\kappa}{\partial y} \right) dy = 0,$$

which may be written

$$\frac{\partial}{\partial x_\kappa} \int_0^{h(x,t)} u^{(1)}(x,y) dy + v_\kappa \Big|_h - v_\kappa \Big|_0 = 0. \tag{2.30}$$

For wavy interfacial flows, the flow rate of the first layer may be introduced as

$$q^{(1)} \equiv \int_0^{h(x,t)} u^{(1)}(x,y) dy. \tag{2.31}$$

Using (2.31) and that $v_\kappa = 0$ on the channel wall at $y = 0$, the equation (2.30) may be written as

$$\frac{\partial q^{(1)}}{\partial x_\kappa} - u^{(1)} \Big|_h \frac{\partial h}{\partial x} + v_\kappa \Big|_h = 0.$$

Finally, using the kinematic boundary condition on the interface, the equation may be

written

$$\frac{\partial q^{(1)}}{\partial x_\kappa} + \frac{\partial h}{\partial t} = 0.$$

Similarly, integrating over the second liquid layer,

$$\int_{h(x,t)}^{1} \left(\frac{\partial u^{(2)}}{\partial x_\kappa} + \frac{\partial v_\kappa}{\partial y} \right) dy = 0,$$

it is seen that

$$\frac{\partial}{\partial x_\kappa} \int_{h(x,t)}^{1} u^{(2)}(x,y)dy + v_\kappa\Big|_1 - v_\kappa\Big|_h = 0. \tag{2.32}$$

Introducing the following expression for the second layer flow rate, similar to that for the first layer flow rate,

$$\int_{h(x,t)}^{1} u^{(2)}(x,y)dy \equiv q^{(2)}, \tag{2.33}$$

and noting that $v_\kappa = 0$ on the channel wall at $y = 1$, equation (2.32) may be written

$$\frac{\partial q^{(2)}}{\partial x_\kappa} + u^{(2)}\big|_h \frac{\partial h}{\partial x} - v_\kappa|_h = 0.$$

Finally, using the kinematic boundary condition on the interface, it is seen that

$$\frac{\partial q^{(2)}}{\partial x_\kappa} - \frac{\partial h}{\partial t} = 0.$$

Now dealing with the x-momentum equation, integration over the first liquid layer is carried out first,

$$\int_0^{h(x,t)} \left(\frac{\partial u^{(1)}}{\partial t_\kappa} + u^{(1)} \frac{\partial u^{(1)}}{\partial x_\kappa} + v_\kappa \frac{\partial u^{(1)}}{\partial y} \right) dy = \tag{2.34}$$

$$\int_0^{h(x,t)} \left(-\frac{1}{\rho_0^{(1)}} \frac{\partial p^{(1)}}{\partial x_\kappa} + \frac{\nu_0^{(1)}}{5\delta b\gamma} \frac{\partial^2 u^{(1)}}{\partial y^2} + \frac{1}{\kappa \mathrm{Fr}^2} \right) dy.$$

The following terms on the left-hand-side may be re-written as

$$\begin{aligned} u^{(1)} \frac{\partial u^{(1)}}{\partial x_\kappa} + v_\kappa \frac{\partial u^{(1)}}{\partial y} &= u^{(1)} \frac{\partial u^{(1)}}{\partial x_\kappa} + \frac{\partial \left(u^{(1)} v_\kappa \right)}{\partial y} - u^{(1)} \frac{\partial v_\kappa}{\partial y}, \\ &= u^{(1)} \frac{\partial u^{(1)}}{\partial x_\kappa} + \frac{\partial \left(u^{(1)} v_\kappa \right)}{\partial y} + u^{(1)} \frac{\partial u^{(1)}}{\partial x_\kappa}, \\ &= \frac{\partial \left(u^{(1)} \right)^2}{\partial x_\kappa} + \frac{\partial \left(u^{(1)} v_\kappa \right)}{\partial y}, \end{aligned}$$

by exploiting the continuity equation and reassembling the derivative of $u^{(1)}$. Now using the relationship (2.20) and that $\rho_0^{(1)} = \nu_0^{(1)} = 1$, equation (2.34) may be written as

$$\begin{aligned} \frac{\partial q^{(1)}}{\partial t_\kappa} - u^{(1)}\Big|_h \frac{\partial h}{\partial x_\kappa} + \int_0^{h(x,t)} \left(\frac{\partial \left(u^{(1)} \right)^2}{\partial x_\kappa} + \frac{\partial (u^{(1)} v_\kappa)}{\partial y} \right) dy = \\ - h \frac{\partial p^{(1)}}{\partial x_\kappa} + \frac{1}{5\delta b\gamma} \left(\frac{\partial u^{(1)}}{\partial y}\Big|_{y=h} - \frac{\partial u^{(1)}}{\partial y}\Big|_{y=0} \right) + \frac{h}{5\delta b}, \end{aligned}$$

or,

$$\begin{aligned} \frac{\partial q^{(1)}}{\partial t_\kappa} - u^{(1)}\Big|_h \frac{\partial h}{\partial x_\kappa} + \frac{\partial}{\partial x_\kappa} \int_0^{h(x,t)} \left(u^{(1)} \right)^2 dy - \left(u^{(1)} \right)^2 \Big|_h \frac{\partial h}{\partial x} + \left(u^{(1)} v_\kappa \right) \Big|_h - \left(u^{(1)} v_\kappa \right) \Big|_0 = \\ - h \frac{\partial p^{(1)}}{\partial x_\kappa} + \frac{1}{5\delta b\gamma} \left(\frac{\partial u^{(1)}}{\partial y}\Big|_{y=h} - \frac{\partial u^{(1)}}{\partial y}\Big|_{y=0} \right) + \frac{h}{5\delta b}. \end{aligned}$$

Now since $v_\kappa = 0$ on the channel wall at $y = 0$, and also noting that multiplying the kinematic boundary condition by $u^{(1)}$, $u^{(1)} \dfrac{\partial h}{\partial t_\kappa} + \left(u^{(1)} \right)^2 \dfrac{\partial h}{\partial x_\kappa} = v_\kappa u^{(1)}$, equation (2.2.5) may be written

$$\frac{\partial q^{(1)}}{\partial t_\kappa} + \frac{\partial}{\partial x_\kappa} \int_0^{h(x,t)} \left(u^{(1)} \right)^2 dy = -h \frac{\partial p^{(1)}}{\partial x_\kappa} + \frac{1}{5\delta b\gamma} \left(\frac{\partial u^{(1)}}{\partial y}\Big|_{y=h} - \frac{\partial u^{(1)}}{\partial y}\Big|_{y=0} \right) + \frac{h}{5\delta b}.$$

Similarly, integration of the x-momentum equation is carried out over the second liquid layer

$$\int_{h(x,t)}^{1}\left(\frac{\partial u^{(2)}}{\partial t_\kappa}+u^{(2)}\frac{\partial u^{(2)}}{\partial x_\kappa}+v_\kappa\frac{\partial u^{(2)}}{\partial y}\right)dy=\int_{h(x,t)}^{1}\left(-\frac{1}{\rho_0^{(2)}}\frac{\partial p^{(2)}}{\partial x_\kappa}+\frac{\nu_0^{(2)}}{5\delta b\gamma}\frac{\partial^2 u^{(2)}}{\partial y^2}+\frac{1}{\kappa \mathrm{Fr}^2}\right)dy.$$

Again using the relationship (2.20) and also that $\rho_0^{(2)}=\rho_0$ and $\nu_0^{(2)}=\nu_0^{(2)}$, equation (2.2.5) may be written,

$$\frac{\partial}{\partial t_\kappa}\int_{h(x,t)}^{1}u^{(2)}dy+\int_{(h(x,t)}^{1}\left(u^{(2)}\frac{\partial u^{(2)}}{\partial x_\kappa}+\frac{\partial\left(u^{(2)}v_\kappa\right)}{\partial y}-u^{(2)}\frac{\partial v_\kappa}{\partial y}\right)dy=$$
$$-\frac{1}{\rho_0}\frac{\partial p^{(2)}}{\partial x_\kappa}(1-h)+\frac{\nu_0}{5\delta b\gamma}\left[\frac{\partial u^{(2)}}{\partial y}\right]_{y=h(x)}^{y=1}+\frac{1-h}{5\delta b}.$$

Finally, using the same techniques as above to rewrite the left hand side terms, it is seen that

$$\frac{\partial q^{(2)}}{\partial t_\kappa}+\frac{\partial}{\partial x_\kappa}\int_{h(x,t)}^{1}\left(u^{(2)}\right)^2dy=-\frac{1-h}{\rho_0}\frac{\partial p^{(2)}}{\partial x_\kappa}+\frac{\nu_0}{5\delta b\gamma}\left(\left.\frac{\partial u^{(2)}}{\partial y}\right|_{y=1}-\left.\frac{\partial u^{(2)}}{\partial y}\right|_{y=h}\right)+\frac{1-h}{5\delta b}.$$

Combining all above derivations, the following system of integral equations is found,

$$\begin{aligned}
&\frac{\partial h}{\partial t_\kappa}+\frac{\partial q^{(1)}}{\partial x_\kappa}=0, \qquad (2.35)\\
&\frac{\partial q^{(1)}}{\partial t_\kappa}+\frac{\partial}{\partial x_\kappa}\int_0^h\left(u^{(1)}\right)^2\,dy=-h\frac{\partial p^{(1)}}{\partial x_\kappa}+\frac{1}{5\delta b\gamma}\left(\left.\frac{\partial u^{(1)}}{\partial y}\right|_{y=h}-\left.\frac{\partial u^{(1)}}{\partial y}\right|_{y=0}\right)+\frac{h}{5\delta b},\\
&\frac{\partial h}{\partial t_\kappa}-\frac{\partial q^{(2)}}{\partial x_\kappa}=0,\\
&\frac{\partial q^{(2)}}{\partial t_\kappa}+\frac{\partial}{\partial x_\kappa}\int_h^1\left(u^{(2)}\right)^2\,dy=-\frac{1-h}{\rho_0}\frac{\partial p^{(2)}}{\partial x_\kappa}+\frac{\nu_0}{5\delta b\gamma}\left(\left.\frac{\partial u^{(2)}}{\partial y}\right|_{y=1}-\left.\frac{\partial u^{(2)}}{\partial y}\right|_{y=h}\right)\\
&\quad+\frac{1-h}{5\delta b}.
\end{aligned}$$

Rearranging the two momentum equations for the pressure terms, and subtracting the second from the first, the boundary condition relating to the balance of normal stress across the interface from (2.35), $[p]_1^2 - \frac{1}{5\delta b}\frac{\partial^2 h}{\partial x_\kappa^2} = 0$, may be differentiated to eliminate pressure entirely from the following third order equation,

$$\begin{aligned}
&\frac{1}{h}\left[\frac{\partial q^{(1)}}{\partial t_\kappa} + \frac{\partial}{\partial x_\kappa}\int_0^h \left(u^{(1)}\right)^2 \, dy\right] - \frac{\rho_0}{1-h}\left[\frac{\partial q^{(2)}}{\partial t_\kappa} + \frac{\partial}{\partial x_\kappa}\int_h^1 \left(u^{(2)}\right)^2 dy\right] \\
&-\frac{1}{5\delta b}\frac{\partial^3 h}{\partial x_\kappa^3} - \frac{1}{5\delta b\gamma h}\left(\left.\frac{\partial u^{(1)}}{\partial y}\right|_h - \left.\frac{\partial u^{(1)}}{\partial y}\right|_0\right) \\
&+\frac{\rho_0\nu_0}{5\delta b\gamma\left(1-h\right)}\left(\left.\frac{\partial u^{(2)}}{\partial y}\right|_1 - \left.\frac{\partial u^{(2)}}{\partial y}\right|_h\right) - \frac{1-\rho_0}{5\delta b} = 0.
\end{aligned} \tag{2.36}$$

Also, subtracting the continuity equations from (2.35) leads to

$$q^{(1)} + q^{(2)} = q\left(t_\kappa\right). \tag{2.37}$$

Thus, the the total flow rate q does not depend on x_κ, since at any position downstream, the total flow rate is equal. Below, the case of a constant total flow rate, $q \equiv 1$, is studied. Therefore, the flow rate of the second layer, $q^{(2)}$, may be eliminated from the system using (2.37).

The second step of the falling film type simplification method requires the velocity profiles to be approximated with quadratics which satisfy the boundary conditions in (2.29),

$$\begin{aligned}
&u^{(1)} = a_{11}y + a_{12}y^2, \quad u^{(2)} = a_{21}\left(y-1\right) + a_{22}\left(y-1\right)^2, \\
&a_{11} = \frac{3\left[1-\left(1-2\rho_0\nu_0\right)h\right]}{h^2\left[1-\left(1-\rho_0\nu_0\right)h\right]}\, q^{(1)} + \frac{3}{h\left(h-1\right)^2}\Bigg\{4 - 2\left(2-\rho_0\nu_0\right)h \\
&\qquad -\frac{\left[1-\left(1-2\rho_0\nu_0\right)h\right]\left[4-\left(4-\rho_0\nu_0\right)h\right] + 2\rho_0\nu_0 h\left(h-1\right)}{1-\left(1-\rho_0\nu_0\right)h}\Bigg\}\, q^{(2)},
\end{aligned}$$

$$
\begin{aligned}
a_{12} &= -\frac{3\left[1-\left(1-4\rho_0\nu_0\right)h\right]}{2h^3\left[1-\left(1-\rho_0\nu_0\right)h\right]}\ q^{(1)} \\
&\quad -\frac{3}{2h^2\left(h-1\right)^2}\left\{4-2\left(2-\rho_0\nu_0\right)h-\frac{\left[1-\left(1-2\rho_0\nu_0\right)h\right]\left[4-\left(4-\rho_0\nu_0\right)h\right]}{1-\left(1-\rho_0\nu_0\right)h}\right\}\ q^{(2)}, \\
a_{21} &= \frac{3}{h\left[1-\left(1-\rho_0\nu_0\right)h\right]}\ q^{(1)}-\frac{3\left[2-\left(2-\rho_0\nu_0\right)h\right]}{\left(h-1\right)^2\left[1-\left(1-\rho_0\nu_0\right)h\right]}\ q^{(2)}, \\
a_{22} &= -\frac{9}{2h\left(h-1\right)\left[1-\left(1-\rho_0\nu_0\right)h\right]}\ q^{(1)}+\frac{3\left[4-\left(4-\rho_0\nu_0\right)h\right]}{2\left(h-1\right)^3\left[1-\left(1-\rho_0\nu_0\right)h\right]}\ q^{(2)}.
\end{aligned}
$$

Substituting these approximations into (2.36) leads to the system of evolution equations for two variables,

$$
\begin{aligned}
&\frac{\partial h}{\partial t_\kappa}+\frac{\partial q^{(1)}}{\partial x_\kappa}=0, \\
&\left(1+\frac{\rho_0 h}{1-h}\right)\frac{\partial q^{(1)}}{\partial t_\kappa}+\frac{\partial}{\partial x_\kappa}\left(\frac{a_{11}^2}{3}h^3+\frac{a_{11}a_{12}}{2}h^4+\frac{a_{12}^2}{5}h^5\right)+ \\
&\quad\frac{\rho_0 h}{1-h}\frac{\partial}{\partial x_\kappa}\left(\frac{a_{21}^2}{3}\left(h-1\right)^3+\frac{a_{21}a_{22}}{2}\left(h-1\right)^4+\frac{a_{22}^2}{5}\left(h-1\right)^5\right)= \\
&\quad\frac{1}{5\delta b}\left[h\frac{\partial^3 h}{\partial x_\kappa^3}+\frac{2\left(a_{12}-\rho_0\nu_0 a_{22}\right)}{\gamma}h+\left(1-\rho_0\right)h\right].
\end{aligned}
\tag{2.38}
$$

The system of evolution equations (2.38) for variables $h\left(x_\kappa,t_\kappa\right)$ and $q^{(1)}\left(x_\kappa,t_\kappa\right)$, first derived by Sisoev *et al.* [52], includes the following similarity parameters: two parameters, ρ_0 and ν_0, characterising the physical properties of fluids, the parameter H is the relative thickness of the first layer, and the film parameter δ is based on the properties of the first layer fluid and the layer thickness. The full problem (2.15) also depends on the Kapitza number, Ka, whose large values for most fluids, consequently provides small values of κ^2, assumed in order to derive the equations (2.38). The system of evolution equations is now much simpler to solve as it contains just two unknowns, namely the location of the interface, h, and the flow rate of the first layer, $q^{(1)}$, depending on x_κ and t_κ, and contains one fewer dimensionless parameter.

As shown by Sisoev *et al.* [52] the system (2.38) can be reduced to the falling film

case. This is achieved by considering the ratio of densities tending to zero, $\rho_0 \to 0$, to represent the large difference in densities between, for example, water and air.

The steady flow solution (2.16) corresponds to the solution $h = H$ and $q^{(1)} = Q^{(1)}$, see (2.17), of the system (2.38).

Considering both $h = h_0$ and $q^{(1)} = q_0^{(1)}$ as constants, the system is reduced to

$$\frac{2}{\gamma}\left(a_{12} - \rho_0\nu_0 a_{22}\right) + 1 - \rho_0 = 0, \quad q_0^{(1)} + q_0^{(2)} = 1 \tag{2.39}$$

where

$$\begin{aligned}
a_{12} &= a_{12,0}^{(1)} q_0^{(1)} + a_{12,0}^{(2)} q_0^{(2)}, \quad a_{12,0}^{(1)} = -\frac{3\left[1 - \left(1 - 4\rho_0\nu_0\right) h_0\right]}{2h_0^3\left[1 - \left(1 - \rho_0\nu_0\right) h_0\right]}, \qquad (2.40)\\
a_{12,0}^{(2)} &= -\frac{3}{2h_0^2\left(h_0 - 1\right)^2}\Bigg\{4 - 2\left(2 - \rho_0\nu_0\right) h_0 \\
&\qquad\qquad - \frac{\left[1 - \left(1 - 2\rho_0\nu_0\right) h_0\right]\left[4 - \left(4 - \rho_0\nu_0\right) h_0\right]}{1 - \left(1 - \rho_0\nu_0\right) h_0}\Bigg\}\\
a_{22} &= a_{22,0}^{(1)} q_0^{(1)} + a_{22,0}^{(2)} q_0^{(2)}, \quad a_{22,0}^{(1)} = -\frac{9}{2h_0\left(h_0 - 1\right)\left[1 - \left(1 - \rho_0\nu_0\right) h_0\right]}\\
a_{22,0}^{(2)} &= \frac{3\left[4 - \left(4 - \rho_0\nu_0\right) h_0\right]}{2\left(h_0 - 1\right)^3\left[1 - \left(1 - \rho_0\nu_0\right) h_0\right]}.
\end{aligned}$$

Hence the first and second layer flow rates may be calculated as

$$q_0^{(1)} = \frac{\frac{\gamma(\rho_0 - 1)}{2} - \left(a_{12,0}^{(2)} - \rho_0\nu_0 a_{22,0}^{(2)}\right)}{a_{12,0}^{(1)} - \rho_0\nu_0 a_{22,0}^{(1)} - \left(a_{12,0}^{(2)} - \rho_0\nu_0 a_{22,0}^{(2)}\right)}, \quad q_0^{(2)} = 1 - q_0^{(1)}. \tag{2.41}$$

2.2.6 Linear stability analysis

To investigate the linear stability of the waveless solution (2.39), a solution of (2.38) is considered in the form

$$h\left(x_\kappa, t_\kappa\right) = H + \widehat{h}\left(x_\kappa, t_\kappa\right), \quad q^{(1)}\left(x_\kappa, t_\kappa\right) = Q^{(1)} + \widehat{q}^{(1)}\left(x_\kappa, t_\kappa\right),$$

where $\widehat{h}$ and $\widehat{q}^{(1)}$ are small perturbations. Further linearisation leads to the equations

$$\begin{aligned}
&\frac{\partial \widehat{h}}{\partial t_\kappa} + \frac{\partial \widehat{q}^{(1)}}{\partial x_\kappa} = 0, \\
&\left(\frac{1}{H} + \frac{\rho_0}{1-H}\right)\frac{\partial \widehat{q}^{(1)}}{\partial t_\kappa} + \frac{1}{H}\frac{\partial}{\partial x_\kappa}\left(I_{1,1}\widehat{h} + I_{1,2}\widehat{q}^{(1)}\right) + \frac{\rho_0}{1-H}\frac{\partial}{\partial x_\kappa}\left(I_{2,1}\widehat{h} + I_{2,2}\widehat{q}^{(1)}\right) \\
&\quad = \frac{1}{5\delta_p\beta}\frac{\partial^3 \widehat{h}}{\partial x_\kappa^3} + \frac{2}{5\delta_p\beta}\left[\left(a_{12,1} - \rho_0\nu_0 a_{22,1}\right)\widehat{h} + \left(a_{12,2} - \rho_0\nu_0 a_{22,2}\right)\widehat{q}^{(1)}\right],
\end{aligned}$$

where the calculation of coefficients $I_{i,j}$ for $i = 1, 2$ and $j = 0, 1, 2$ are given in Appendix (A.1) for the sake of brevity.

Substituting normal modes,

$$\left(\widehat{h}, \widehat{q}^{(1)}\right) = \left(\breve{h}, \breve{q}^{(1)}\right) e^{i\alpha_\kappa\left(x_\kappa - ct_\kappa\right)},$$

gives the characteristic equation for the complex velocity $c = c_r + ic_i$, depending on the wavenumber α_κ and the similarity parameters ρ_0, ν_0, δ and H,

$$\begin{aligned}
&\left(\frac{1}{H} + \frac{\rho_0}{1-H}\right)c^2 - \left[\frac{2i}{5\delta\beta\alpha_\kappa}\left(a_{12,2} - \rho_0\nu_0 a_{22,2}\right) + \frac{I_{1,2}}{H} + \frac{\rho_0 I_{2,2}}{1-H}\right]c \\
&\quad - \frac{\alpha_\kappa^2}{5\delta\beta} - \frac{2i}{5\delta\beta\alpha_\kappa}\left(a_{12,1} - \rho_0\nu_0 a_{22,1}\right) - \frac{I_{1,1}}{H} - \frac{\rho_0 I_{2,1}}{1-H} = 0.
\end{aligned} \tag{2.42}$$

The equation (2.42) allows the neutral velocity c_n, when $c_i = 0$, and the wavenumber

$\alpha_{\kappa,n}$ to be found,

$$c_n = -\frac{a_{12,1} - \rho_0\nu_0 a_{22,1}}{a_{12,2} - \rho_0\nu_0 a_{22,2}},$$
$$\alpha_{\kappa,n}^2 = 5\delta\beta\left[\left(\frac{1}{H} + \frac{\rho_0}{1-H}\right)c_n^2 - \left(\frac{I_{1,2}}{H} + \frac{\rho_0 I_{2,2}}{1-H}\right)c_n - \frac{I_{1,1}}{H} - \frac{\rho_0 I_{2,1}}{1-H}\right].$$

The linear stability analysis discussed above was first carried out by Sisoev *et al.* [52] where the linear spectra of (2.42) and the Orr-Sommerfeld problem (2.28) were compared in order to verify the evolution model (2.38).

2.3 Pressure-driven two-layer microchannel flow

In the case of the pressure-driven flow, the problem formulation is identical to that of the gravity-driven case. However, there is one essential difference in the problem statement. In the gravity-driven case, the flow was considered to be acted upon by the body force gravity, and hence the dimensionless x-momentum equation included the gravity term $\frac{1}{\kappa \mathrm{Fr}^2}$. In this section, the flow is considered to be driven by a pressure gradient, that is, driven by the boundary condition stating that the pressure at the channel inlet is greater than the pressure at the channel outlet. The gravity term is therefore neglected from the x-momentum equation. The force of gravity is considered weak compared to that of the imposed pressure gradient.

It is seen therefore, that the combination of this section and the previous, deals with the two main cases of fluid flow: driven by a body force, and driven by a boundary force.

2.3.1 Steady flow solution

The system (2.15), as with the gravity-driven case, has a waveless (steady) solution. Considering the solution (2.8), the equations for the pressure-driven case retain the pressure term $\frac{dP}{dx_\kappa}$. Furthermore, in the absence of the gravitational force, $g \to 0$, it is seen that

$\frac{1}{\mathrm{Fr}^2} \to 0$. Hence the steady flow solution is given below, denoted by capital letters,

$$\begin{aligned} y \in [0, H] \quad &: \quad U^{(1)}(y) = \mathrm{Re}\frac{dP}{dx}\left(y^2 - ay\right), \quad V^{(1)} = 0, \quad P^{(1)} = P, \\ y \in [H, 1] \quad &: \quad U^{(2)}(y) = \frac{\mathrm{Re}}{2\rho_0\nu_0}\frac{dP}{dx}\left(y^2 - 1 - a(y-1)\right), \quad V^{(2)} = 0, \quad P^{(2)} = P, \end{aligned} \tag{2.43}$$

where the pressure gradient $dP/dx = \mathrm{const} < 0$ is given, and the coefficient a depends on $\rho_0\nu_0$ and H,

$$a = \frac{1 - (1 - \rho_0\nu_0)H^2}{1 - (1 - \rho_0\nu_0)H}.$$

The flow rates in each layer are calculated as

$$\begin{aligned} Q^{(1)} &= \int_0^H U^{(1)} dy = \mathrm{Re}\frac{dP}{dx}\frac{H^2}{2}\left(\frac{H}{3} - \frac{a}{2}\right), \\ Q^{(2)} &= \int_H^1 U^{(2)} dy = -\frac{\mathrm{Re}}{2\rho_0\nu_0}\frac{dP}{dx}\left(\frac{2 - 3H + H^3}{3} + \frac{(2H - 1 - H^2)a}{2}\right), \end{aligned} \tag{2.44}$$

and summing them, the total flow rate is given by

$$Q = Q^{(1)} + Q^{(2)} = \varphi_2(\rho_0\nu_0, H)\,\mathrm{Re}\frac{dP}{dx}, \tag{2.45}$$

where φ_2 is given in (2.11).

The choice of velocity scale, providing a unit total flow rate, gives a relation between the Reynolds number, Re, the product of the ratios of density, ρ_0, and viscosity, ν_0, the dimensionless thickness of the first layer in the waveless flow, H, and the dimensionless

pressure gradient, dP/dx, see (2.12),

$$\varphi_2 \mathrm{Re} \frac{dP}{dx} = 1. \tag{2.46}$$

This equation in dimensional form yields the velocity scale, see (2.13),

$$U_c = \frac{\varphi_2 H_c^2}{\rho^{(1)} \nu^{(1)}} \left(\frac{dP}{dx} \right)_c ,$$

where $(dP/dx)_c$ is the dimensional pressure gradient. Note that this is similar to the velocity scale found for the gravity-driven case apart from the pressure gradient term appears instead of the gravity term.

2.3.2 Similarity parameters

The problem (2.15) contains five governing parameters: Re, We, ρ_0, ν_0 and H. In accordance with (2.44), the first layer thickness of the waveless flow H determines the flow rates in both layers.

As in the previous section, the Reynolds number, Re, and the Weber number, We, are replaced with the Kapitza number, Ka, and the film parameter, δ_p, in line with the convention of falling films [12]. However, since the effect of gravity is not considered here, as explained above, two new parameters, Ka_p and δ_p, which are similar to the Kapitza number and the film parameter, but based on the pressure gradient of the waveless flow, are introduced,

$$\mathrm{Ka}_p = \frac{\sigma}{\left[\left(\rho^{(1)}\right)^2 \left(\nu^{(1)}\right)^4 \left(-\frac{dP}{dx}\right)_c \right]^{\frac{1}{3}}}, \quad \delta_p = \frac{1}{45 \rho^{(1)} \left(\nu^{(1)}\right)^2} \left[\frac{\left(-\frac{dP}{dx}\right)_c^4 \left(H_c H\right)^{11}}{\sigma} \right]^{\frac{1}{3}}.$$

Then, the Reynolds number and the Weber number can be calculated using these new

parameters

$$\mathrm{Re} = -\frac{\varphi_2 \left(45\delta_p\right)^{\frac{9}{11}} \mathrm{Ka}_p^{\frac{3}{11}}}{H^3}, \quad \mathrm{We} = \frac{\varphi_2^2}{H^5} \frac{\left(45\delta_p\right)^{\frac{15}{11}}}{\mathrm{Ka}_p^{\frac{6}{11}}}, \tag{2.47}$$

and the inverse formulas are

$$\mathrm{Ka}_p = -\frac{\varphi_2^{\frac{1}{3}} \mathrm{Re}^{\frac{5}{3}}}{\mathrm{We}}, \quad \delta_p = \frac{1}{45} \left(\frac{H^{11} \mathrm{Re}^2 \mathrm{We}}{\varphi_2^4}\right)^{\frac{1}{3}}.$$

To complete the problem formulation for the pressure-driven case, the stretching parameter κ in (2.15) must be determined in terms of the new parameters Ka_p and δ_p. Again, observing that capillary waves can be observed in interfacial flows if there is a balance of viscous and capillary forces, a relationship can be formulated,

$$(\kappa \mathrm{Re})^{-1} = \frac{\kappa^2}{\mathrm{We}}.$$

Using (2.47), this relation allows the stretching parameter to be found,

$$\kappa = -\frac{\varphi_2^{\frac{1}{3}} \left(45\delta_p\right)^{\frac{2}{11}}}{\left(\mathrm{Ka}_p^{\frac{3}{11}} H^{\frac{2}{3}}\right)}.$$

Finally, relations for the coefficients in (2.15) may be written as,

$$\frac{1}{\kappa \mathrm{Re}} = \frac{\kappa^2}{\mathrm{We}} = \frac{1}{5\delta_p \beta}, \quad \beta = 9 \left(\frac{\varphi_2^4}{H^{11}}\right)^{\frac{1}{3}}.$$

It is worth noting that the case $\delta_p \to 0$, and thus $\kappa \mathrm{Re} \to 0$, corresponds to the lubrication approximation exploited in papers reviewed in Chapter 1. Below, the case of finite values of the parameter δ_p, when inertia is important, is analysed.

2.3.3 Linear stability analysis: eigenvalue problem

The eigenvalue problem for the pressure-driven waveless flow solution is found in the same way as in section (2.2.3). A solution of (2.15) is sought by applying a small perturbation to the steady flow solution (2.43) and substituting into (2.15). Linearising the resulting system and substituting in normal modes, the system for amplitude functions is found. Finally, rearranging the equations leads to the eigenvalue problem,

$$
\begin{aligned}
&\check{v}'''' - 2\alpha^2\check{v}'' + \alpha^4\check{v} - \frac{i\alpha\mathrm{Re}}{\nu_0^{(j)}}\left[(U-c)(\check{v}''-\alpha^2\check{v}) - U''\check{v}\right] = 0,\\
&y = 0: \quad \check{v} = 0, \quad \check{v}' = 0,\\
&y = H: \quad [\check{v}]_1^2 = 0,\\
&\qquad \left[\check{v}' - \frac{U'}{U-c}\check{v}\right]_1^2 = 0,\\
&\qquad \left[\rho_0^{(j)}\nu_0^{(j)}\left(\check{v}''' - \left(3\alpha^2 + \frac{i\alpha\mathrm{Re}}{\nu_0^{(j)}}(U-c)\right)\check{v}'\right.\right.\\
&\qquad\quad \left.\left. + \left(\frac{i\alpha\mathrm{Re}U'}{\nu_0^{(j)}} + \frac{2\alpha^2U'}{U-c} - \frac{i\alpha\mathrm{Re}P'}{\rho_0^{(j)}\nu_0^{(j)}(U-c)}\right)\check{v}\right)\right]_1^2 - \frac{i\alpha\mathrm{Re}}{\mathrm{We}(U-c)}\check{v} = 0,\\
&\qquad \left[\rho_0^{(j)}\nu_0^{(j)}\left(\check{v}'' + \left(\alpha^2 - \frac{U''}{U-c}\right)\check{v}\right)\right]_1^2 = 0,\\
&y = 1: \quad \check{v} = 0, \quad \check{v}' = 0.
\end{aligned}
$$

It is seen that the Orr-Sommerfeld problem above is identical to that formulated in subsection (2.2.3). The differences appear in the calculation of the similarity parameters Re and We. Also, different velocity profiles are apparent in the case of the pressure-driven flow.

2.3.4 Similarity parameters in experiments by Zhao *et al.* [67]

In order to verify that the same assumptions can be made regarding the similarity parameters for the pressure driven case, as were made for the gravity driven case in the

previous chapter, a detailed analysis of the experimental data collected by Zhao *et al.* [67], is discussed. It is the intention of this section to confirm that for the pressure-driven flow, the non-linear laminar regimes which are sought, occur at moderate values of the Reynolds number, as they did for the gravity-driven case. Furthermore, it is important to confirm that the same assumptions can be made about the stretching parameter κ^2. This will again enable the approximation $\kappa^2 \ll 1$ to reduce the equations. In the following subsection, the experiments conducted by Zhao *et al.* [67], are used to find real-life values of the similarity parameters.

Dyed deionized water and kerosene were used as working liquids Zhao *et al.* [67], and the properties of these liquids are

$$\begin{aligned} &\rho^{(1)} = 0.9982 \text{ g cm}^{-3}, \qquad &&\nu^{(1)} = 0.01 \text{ cm}^2 \text{ s}^{-1}, \\ &\rho^{(2)} = 0.780 \text{ g cm}^{-3}, \qquad &&\nu^{(2)} = 0.0147 \text{ cm}^2\text{s}^{-1}, \\ &\sigma = 45 \text{ dyn s}^{-1}, \end{aligned}$$

and thus $\rho_0 = 0.781$ and $\nu_0 = 1.47$, so that $\rho_0\nu_0 = 1.15$. All flow regimes were summarised in the plane $(\text{We}_{ws}, \text{We}_{ks})$ where the Weber numbers of water and kerosene were defined as follows,

$$\text{We}_{ws} = \frac{D_H U_{ws}^2 \rho^{(1)}}{\sigma}, \quad \text{We}_{ks} = \frac{D_H U_{ks}^2 \rho^{(2)}}{\sigma}, \tag{2.48}$$

where $D_H = 0.04$ cm is the hydraulic diameter[2], and $U_{ws} = Q_{ws}/A$ and $U_{ks} = Q_{ks}/A$ are the superficial velocities[3] where $A = 0.0018\text{cm}^2$ is the cross-sectional area of the microchannel and Q_{ws} and Q_{ks} are the flow rates of the water and kerosene layers, respectively. Different stable flow regimes were observed: parallel flows, slug flows, droplet flows

[2]The hydraulic diameter is defined as $D_H = \frac{4A}{P}$, where A is the cross sectional area and P is the perimeter. The hydraulic diameter is used for convenience when dealing with non-circular pipes.

[3]Superficial velocities are calculated as if each phase was flowing separately, alone in the channel.

Case	$\log_{10}\mathrm{We}_{ks}$	H	$Q^{(1)}$	$Q^{(2)}$	δ_p	Ka_p	κ^2	Re	We	κRe
A	-0.94	0.462	0.452	0.548	0.967	2218	0.03	141	0.734	24.4
B	-1.14	0.501	0.509	0.491	1.104	2308	0.0277	125	0.578	20.8
C	-1.68	0.602	0.659	0.341	1.536	2516	0.0234	96.6	0.345	14.8
D	-2.28	0.702	0.794	0.206	2.091	2681	0.0206	80.2	0.238	11.5

Table 2.1: Parameters at $\mathrm{We}_{ws} = 0.1$ in experiments [67].

and annular flows. Almost all parallel flows were observed in domain $\log_{10}\mathrm{We}_{ws} \in (-5, 2)$ and $\log_{10}\mathrm{We}_{ks} \in (-4, 2)$.

The experiments by Zhao *et al.* [67] were continued by the same group [69] to analyse the role of the wettability between the walls and liquids. Flow regimes in PMMA[4] microchannels, before and after surface modification, were compared. The experiments displayed an absence of interfacial waves at relatively small values of the Reynolds number Re_M. Unfortunately, there is insufficient information needed re-calculate the regular Reynolds number Re from Re_M, but the values are expected to be close.

By increasing the flow rates of the layers, the amplitudes of the interfacial waves increased and shorter waves were observed. The authors also noted that in the modified channels, only interfacial flow regimes appeared, whereas dispersed flows including slug flows were observed at low flow rates in non-modified microchannels. Wave shapes in non-modified microchannels and modified microchannels at $\mathrm{Re}_M = 55, 110, 165, 220$ and 275 are shown in the paper by Zhao *et al.* [67], Figs. 4b and 5b respectively, over a short distance: about 6 times that of the microchannel width.

Thus, the experimental results in both works by Zhao *et al.* [67, 69] clearly demonstrate the wavy character of two-layer microchannel flows at moderate values of the Reynolds number. Moreover, the observed waves were long, which corresponds to small values of the stretching parameter κ^2 (Fig. 2.2a).

Table 2.1 presents examples of values of We_{ws} and We_{ks} from the domain where the

[4]Poly-methyl-methacrylate, often called acrylic glass.

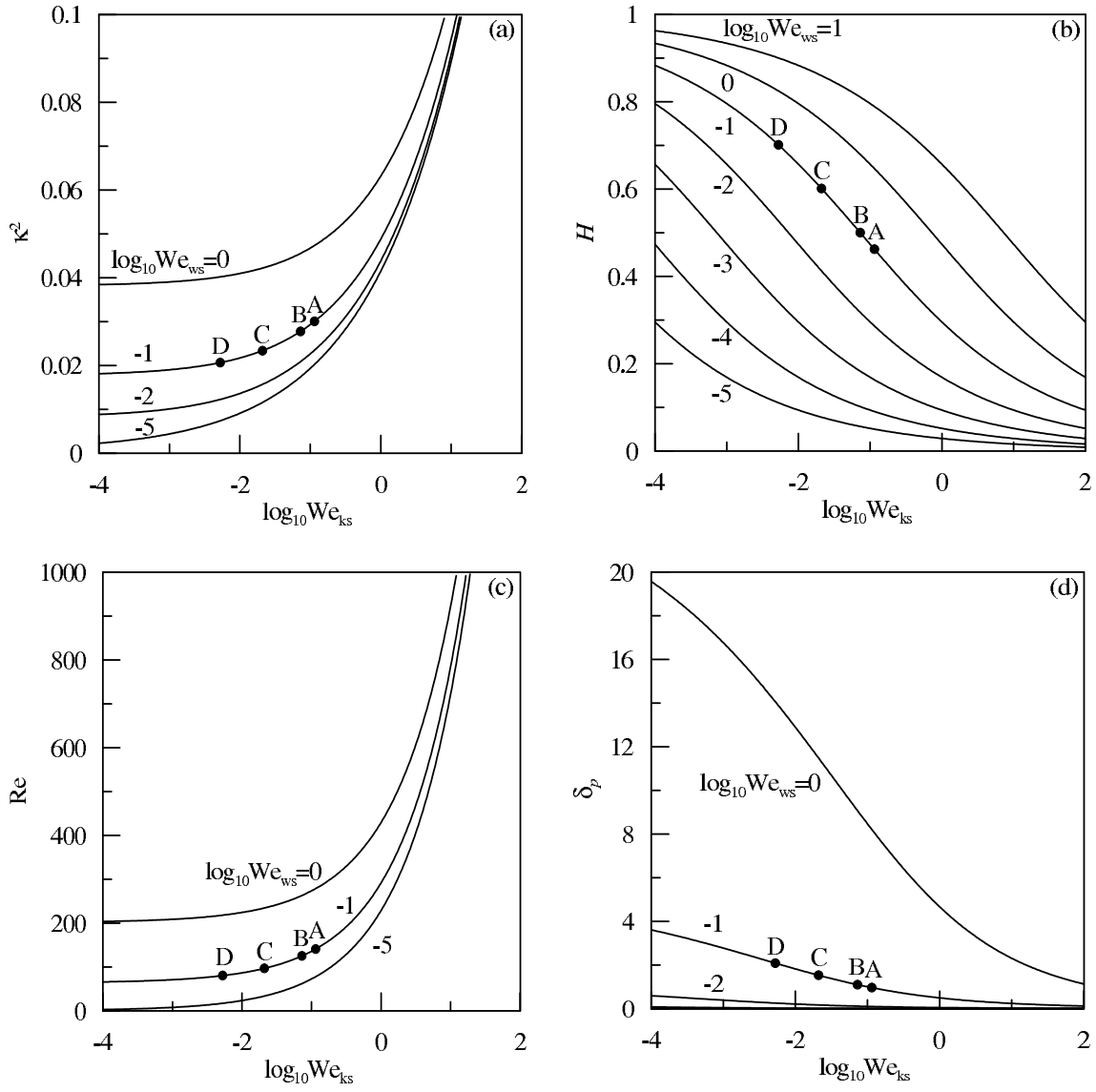

Figure 2.2: Dependence of the stretching κ^2 (a), the first layer thickness H (b), the Reynolds number Re (c) and the film parameter δ_p (d) on the Weber numbers (2.48) for experiments by Zhao *et al.* [67]. The full dots indicate the parameters in the cases A, B, C and D in Table 2.1.

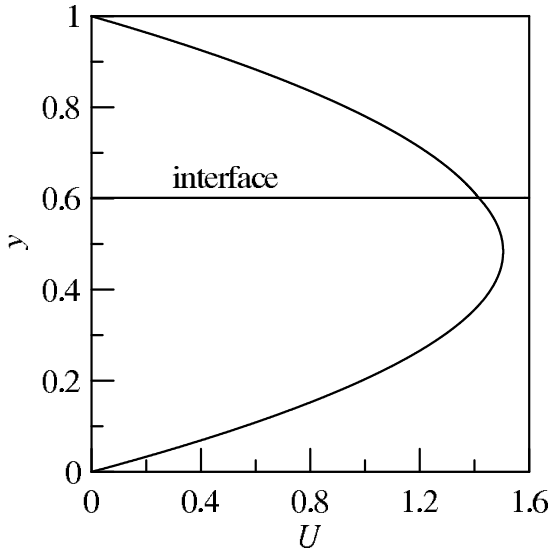

Figure 2.3: Velocity profile (2.43) in case C in Table 2.1.

interfacial flows, or 'parallel flows', were observed in experiments, and corresponding values of the similarity parameters for the model.

Fig. 2.2 shows values of the similarity parameters in this domain. Panel (a) demonstrates that the value κ^2 is small in parallel flows, and panel (b) shows the dependence of the first layer thickness on $\log_{10} \mathrm{We}_{ks}$ at different values of $\log_{10} \mathrm{We}_{ws}$. Panel (c) confirms that the two-layer microchannel flows were studied at moderate values of the Reynolds number where non-linear laminar regimes are expected. Finally, panel (d) shows real-life values of the film parameter δ_p. It is seen that this parameter attains finite values, and hence, the lubrication approximation cannot be used to model flows in these experiments. It is seen that from Table 2.1, for the given values of δ_p, the inverse formula yields Reynolds numbers of order 100. In particular, it is seen that the stretching parameter κ^2 is small in all cases, but the product $\kappa\mathrm{Re}$, which may be referred to as the reduced Reynolds number, attains finite values.

The velocity profile of the steady flow solution (2.43) for case C in Table 2.1, is shown in Fig. 2.3. Since $\rho_0\nu_0 = 1.15$, there is a weak discontinuity of the velocity profile at the

interface.

2.3.5 Long wave approximation

The full Navier-Stokes problem (2.15) may be approximated, as for the gravity-driven problem (2.2.4), by applying the method developed in the film theory [44, 46, 12, 48, 10]. Again, it is seen that in flows where a small value of the stretching parameter κ^2 is attained, for example in the experiments by Zhao *et al.* [67, 69] discussed above, the governing equations may be reduced. Similar estimations can be made for the pressure-driven microchannel flow over a wide range of the similarity parameters, as was the case for the gravity-driven case in the previous section.

Having neglected terms of order $O(\kappa^2)$, the system (2.15) can be reduced to

$$
\begin{aligned}
y = 0 \quad &: \quad u^{(1)} = 0, \quad v_\kappa^{(1)} = 0, \\
y \in (0,h) \quad &: \quad \frac{\partial u^{(1)}}{\partial x_\kappa} + \frac{\partial v_\kappa^{(1)}}{\partial y} = 0, \quad \frac{\partial p^{(1)}}{\partial y} = 0, \\
&\quad \frac{\partial u^{(1)}}{\partial t_\kappa} + u^{(1)}\frac{\partial u^{(1)}}{\partial x_\kappa} + v_\kappa^{(1)}\frac{\partial u^{(1)}}{\partial y} = -\frac{\partial p^{(1)}}{\partial x_\kappa} + \frac{1}{5\delta_p\beta}\frac{\partial^2 u^{(1)}}{\partial y^2}, \\
y = h\,(x_\kappa, t_\kappa) \quad &: \quad \frac{\partial h}{\partial t_\kappa} + u\frac{\partial h}{\partial x_\kappa} = v_\kappa, \quad p^{(2)} - p^{(1)} - \frac{1}{5\delta_p\beta}\frac{\partial^2 h}{\partial x_\kappa^2} = 0, \quad \rho_0\nu_0\frac{\partial u^{(2)}}{\partial y} - \frac{\partial u^{(1)}}{\partial y} = 0, \\
&\quad u^{(2)} - u^{(1)} = 0, \quad v_\kappa^{(2)} - v_\kappa^{(1)} = 0, \\
y \in (h,1) \quad &: \quad \frac{\partial u^{(2)}}{\partial x_\kappa} + \frac{\partial v_\kappa^{(2)}}{\partial y} = 0, \quad \frac{\partial p^{(2)}}{\partial y} = 0 \\
&\quad \frac{\partial u^{(2)}}{\partial t_\kappa} + u^{(2)}\frac{\partial u^{(2)}}{\partial x_\kappa} + v_\kappa^{(2)}\frac{\partial u^{(2)}}{\partial y} = -\frac{1}{\rho_0}\frac{\partial p^{(2)}}{\partial x_\kappa} + \frac{\nu_0}{5\delta_p\beta}\frac{\partial^2 u^{(2)}}{\partial y^2}, \\
y = 1 \quad &: \quad u^{(2)} = 0, \quad v_\kappa^{(2)} = 0.
\end{aligned}
\tag{2.49}
$$

It is seen that the pressure in both layers does not depend on the variable y, and the balance of the normal stresses at the interface allows the pressure in the first layer to be

eliminated,

$$p^{(1)}\left(x_\kappa, t_\kappa\right) = p^{(2)}\left(x_\kappa, t_\kappa\right) - \frac{1}{5\delta_p\beta}\frac{\partial^2 h}{\partial x_\kappa^2}.$$

2.3.6 Integral method and evolution equations

The integral method, as discussed in subsection (2.2.5), is again applied, and follows an identical routine as before. Firstly, integrating the continuity and x-momentum equations from (2.49) across individual fluid layers, leads to

$$\frac{\partial h}{\partial t_\kappa} + \frac{\partial q^{(1)}}{\partial x_\kappa} = 0, \quad q^{(1)} \equiv \int_0^h u^{(1)}\, dy, \tag{2.50}$$

$$\frac{\partial q^{(1)}}{\partial t_\kappa} + \frac{\partial}{\partial x_\kappa}\int_0^h \left(u^{(1)}\right)^2\, dy = -h\left(\frac{\partial p^{(2)}}{\partial x_\kappa} - \frac{1}{5\delta_p\beta}\frac{\partial^3 h}{\partial x_\kappa^3}\right) + \frac{1}{5\delta_p\beta}\left(\left.\frac{\partial u^{(1)}}{\partial y}\right|_h - \left.\frac{\partial u^{(1)}}{\partial y}\right|_0\right),$$

$$\frac{\partial h}{\partial t_\kappa} - \frac{\partial q^{(2)}}{\partial x_\kappa} = 0, \quad q^{(2)} \equiv \int_h^1 u^{(2)}\, dy,$$

$$\frac{\partial q^{(2)}}{\partial t_\kappa} + \frac{\partial}{\partial x_\kappa}\int_h^1 \left(u^{(2)}\right)^2\, dy = -\frac{1-h}{\rho_0}\frac{\partial p^{(2)}}{\partial x_\kappa} + \frac{\nu_0}{5\delta_p\beta}\left(\left.\frac{\partial u^{(2)}}{\partial y}\right|_1 - \left.\frac{\partial u^{(2)}}{\partial y}\right|_h\right).$$

Subtracting the continuity equations, the relation $q^{(1)} + q^{(2)} = q\left(t_\kappa\right)$ is found, and replaces the continuity equation in the second layer. Below, flows with a constant total flow rate $q = 1$ as in the specific steady flow solution, are considered. This means that the pressure gradient should be continually varied in order to maintain the constant total flow rate.

Secondly, the x-components of velocity are approximated with the following quadratic equations, satisfying the boundary conditions in (2.49),

$$u^{(1)} = a_{11}y + a_{12}y^2, \quad u^{(2)} = a_{21}\left(y-1\right) + a_{22}\left(y-1\right)^2,$$

$$
\begin{aligned}
a_{11} &= \frac{3\left[1-(1-2\rho_0\nu_0)\,h\right]}{h^2\left[1-(1-\rho_0\nu_0)\,h\right]}\,q^{(1)} + \frac{3}{h\,(h-1)^2}\Bigg[4-2\,(2-\rho_0\nu_0)\,h \\
&\qquad -\frac{\left[1-(1-2\rho_0\nu_0)\,h\right]\left[4-(4-\rho_0\nu_0)\,h\right]+2\rho_0\nu_0 h\,(h-1)}{1-(1-\rho_0\nu_0)\,h}\Bigg]\,q^{(2)}, \\
a_{12} &= -\frac{3\left[1-(1-4\rho_0\nu_0)\,h\right]}{2h^3\left[1-(1-\rho_0\nu_0)\,h\right]}\,q^{(1)} - \frac{3}{2h^2\,(h-1)^2}\Bigg[4-2\,(2-\rho_0\nu_0)\,h \\
&\qquad -\frac{\left[1-(1-2\rho_0\nu_0)\,h\right]\left[4-(4-\rho_0\nu_0)\,h\right]}{1-(1-\rho_0\nu_0)\,h}\Bigg]\,q^{(2)}, \\
a_{21} &= \frac{3}{h\left[1-(1-\rho_0\nu_0)\,h\right]}\,q^{(1)} - \frac{3\left[2-(2-\rho_0\nu_0)\,h\right]}{(h-1)^2\left[1-(1-\rho_0\nu_0)\,h\right]}\,q^{(2)}, \\
a_{22} &= -\frac{9}{2h\,(h-1)\left[1-(1-\rho_0\nu_0)\,h\right]}\,q^{(1)} + \frac{3\left[4-(4-\rho_0\nu_0)\,h\right]}{2\,(h-1)^3\left[1-(1-\rho_0\nu_0)\,h\right]}\,q^{(2)}.
\end{aligned}
$$

Substituting these approximations into (2.50) leads to the system

$$
\begin{aligned}
&\frac{\partial h}{\partial t_\kappa}+\frac{\partial q^{(1)}}{\partial x_\kappa}=0, \\
&\frac{\partial q^{(1)}}{\partial t_\kappa}+\frac{\partial}{\partial x_\kappa}\left(\frac{a_{11}^2}{3}h^3+\frac{a_{11}a_{12}}{2}h^4+\frac{a_{12}^2}{5}h^5\right)=-h\frac{\partial p^{(2)}}{\partial x_\kappa}+\frac{1}{5\delta_p\beta}h\frac{\partial^3 h}{\partial x_\kappa^3}+\frac{2}{5\delta_p\beta}a_{12}h, \\
&\frac{\partial q^{(2)}}{\partial t_\kappa}-\frac{\partial}{\partial x_\kappa}\left(\frac{a_{21}^2}{3}(h-1)^3+\frac{a_{21}a_{22}}{2}(h-1)^4+\frac{a_{22}^2}{5}(h-1)^5\right) \\
&\quad=-\frac{1-h}{\rho_0}\frac{\partial p^{(2)}}{\partial x_\kappa}-\frac{2\nu_0}{5\delta_p\beta}a_{22}\,(h-1)\,, \\
&q^{(1)}+q^{(2)}=1.
\end{aligned}
$$

The last equation allows $q^{(2)}$ in the third equation to be eliminated, then the two momentum equations can be resolved for two derivatives: $\dfrac{\partial q^{(1)}}{\partial t_\kappa}$ and $\dfrac{\partial p^{(2)}}{\partial x_\kappa}$. Finally, the evolution system for the first layer thickness and flow rate in the first layer is given by

$$
\begin{aligned}
&\frac{\partial h}{\partial t_\kappa}+\frac{\partial q^{(1)}}{\partial x_\kappa}=0, \\
&\left(\frac{1}{h}+\frac{\rho_0}{1-h}\right)\frac{\partial q^{(1)}}{\partial t_\kappa}+\frac{1}{h}\frac{\partial}{\partial x_\kappa}\left(\frac{a_{11}^2}{3}h^3+\frac{a_{11}a_{12}}{2}h^4+\frac{a_{12}^2}{5}h^5\right)
\end{aligned}
\tag{2.51}
$$

$$+\frac{\rho_0}{1-h}\frac{\partial}{\partial x_\kappa}\left(\frac{a_{21}^2}{3}(h-1)^3+\frac{a_{21}a_{22}}{2}(h-1)^4+\frac{a_{22}^2}{5}(h-1)^5\right)$$
$$=\frac{1}{5\delta_p\beta}\frac{\partial^3 h}{\partial x_\kappa^3}+\frac{2}{5\delta_p\beta}\left(a_{12}-\rho_0\nu_0 a_{22}\right),$$

and the local pressure gradient is calculated as

$$\left(h+\frac{1-h}{\rho_0}\right)\frac{\partial p^{(2)}}{\partial x_\kappa}=\frac{1}{5\delta_p\beta}h\frac{\partial^3 h}{\partial x_\kappa^3}+\frac{2}{5\delta_p\beta}\left[a_{12}h-\nu_0 a_{22}(h-1)\right] \tag{2.52}$$
$$-\frac{\partial}{\partial x_\kappa}\left(\frac{a_{11}^2}{3}h^3+\frac{a_{11}a_{12}}{2}h^4+\frac{a_{12}^2}{5}h^5\right)$$
$$+\frac{\partial}{\partial x_\kappa}\left(\frac{a_{21}^2}{3}(h-1)^3+\frac{a_{21}a_{22}}{2}(h-1)^4+\frac{a_{22}^2}{5}(h-1)^5\right).$$

The evolution equations (2.51) describe how the location of the interface and the first layer flow rate develop in space and time, and are comparable to the evolution system for the gravity-driven case.

In the case of the waveless flow, $h=H=\text{const}$, the flow rates $q^{(1)}=Q^{(1)}=\text{const}$ and $q^{(2)}=Q^{(2)}=\text{const}$ have to satisfy the equations

$$a_{12}\left(\rho_0\nu_0,H,Q^{(1)},Q^{(2)}\right)-\rho_0\nu_0 a_{22}\left(\rho_0\nu_0,H,Q^{(1)},Q^{(2)}\right)=0, \tag{2.53}$$
$$Q^{(1)}+Q^{(2)}=1,$$

following from (2.51). Equations (2.53) allow the calculation of the flow rates

$$Q^{(1)}=-H^2\frac{3-2H-(1-\rho_0\nu_0)H^2}{12\varphi_2\left[1-(1-\rho_0\nu_0)H\right]},\quad Q^{(2)}=1-Q^{(1)}, \tag{2.54}$$

which is (2.44) re-written in another form. Then, the pressure gradient is calculated from (2.52),

$$\frac{dP^{(2)}}{dx_\kappa}=\frac{1}{5\delta_p\beta\varphi_2}, \tag{2.55}$$

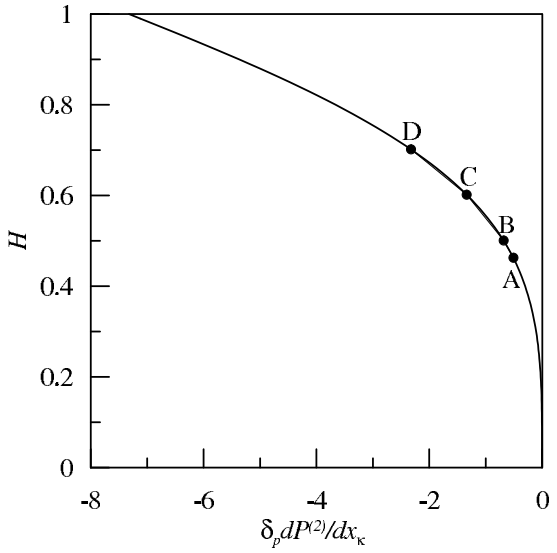

Figure 2.4: Dependence of the pressure gradient (2.55) on the interface location at $\mathrm{We}_{ws} = 0.1$ and $\mathrm{We}_{ks} = 0.1$ in experiments [67].
.

which is formula (2.46) re-written in the new variables.

Fig. 2.4 demonstrates the dependence of the pressure gradient in the second layer on the interface location. The full dots indicate the parameters in the cases A, B, C and D in Table 2.1. It is seen that the interface location is unique for a given pressure gradient.

2.3.7 Linear stability analysis

To investigate the linear stability of the waveless solution (2.53), a solution of (2.51) in the form

$$h\left(x_\kappa, t_\kappa\right) = H + \widehat{h}\left(x_\kappa, t_\kappa\right), \quad q^{(1)}\left(x_\kappa, t_\kappa\right) = Q^{(1)} + \widehat{q}^{(1)}\left(x_\kappa, t_\kappa\right),$$

is considered, where $\widehat{h}$ and $\widehat{q}^{(1)}$ denote small perturbations to the interface location and the first layer flow rate. Further linearisation leads to the equations

$$\frac{\partial \widehat{h}}{\partial t_\kappa} + \frac{\partial \widehat{q}^{(1)}}{\partial x_\kappa} = 0,$$

$$\left(\frac{1}{H}+\frac{\rho_0}{1-H}\right)\frac{\partial\widehat{q}^{(1)}}{\partial t_\kappa}+\frac{1}{H}\frac{\partial}{\partial x_\kappa}\left(I_{1,1}\widehat{h}+I_{1,2}\widehat{q}^{(1)}\right)+\frac{\rho_0}{1-H}\frac{\partial}{\partial x_\kappa}\left(I_{2,1}\widehat{h}+I_{2,2}\widehat{q}^{(1)}\right)$$
$$=\frac{1}{5\delta_p\beta}\frac{\partial^3\widehat{h}}{\partial x_\kappa^3}+\frac{2}{5\delta_p\beta}\left[\left(a_{12,1}-\rho_0\nu_0a_{22,1}\right)\widehat{h}+\left(a_{12,2}-\rho_0\nu_0a_{22,2}\right)\widehat{q}^{(1)}\right],$$

where the coefficients $I_{1,1}$, $I_{1,2}$, $I_{2,1}$, $I_{2,2}$, $a_{12,1}$, $a_{12,2}$, $a_{22,1}$ and $a_{22,2}$ are given in Appendix (A.1) for the sake of brevity. Substituting normal modes,

$$\left(\widehat{h},\widehat{q}^{(1)}\right)=\left(\breve{h},\breve{q}^{(1)}\right)e^{i\alpha_\kappa(x_\kappa-ct_\kappa)},$$

yields the characteristic equation for the complex velocity $c=c_r+ic_i$, depending on the wavenumber α_κ and the similarity parameters ρ_0, ν_0, δ_p and H,

$$\left(\frac{1}{H}+\frac{\rho_0}{1-H}\right)c^2-\left[\frac{2i}{5\delta_p\beta\alpha_\kappa}\left(a_{12,2}-\rho_0\nu_0a_{22,2}\right)+\frac{I_{1,2}}{H}+\frac{\rho_0I_{2,2}}{1-H}\right]c \qquad (2.56)$$
$$-\frac{\alpha_\kappa^2}{5\delta_p\beta}-\frac{2i}{5\delta_p\beta\alpha_\kappa}\left(a_{12,1}-\rho_0\nu_0a_{22,1}\right)-\frac{I_{1,1}}{H}-\frac{\rho_0I_{2,1}}{1-H}=0.$$

The equation (2.56) allows the neutral velocity c_n, when $c_i=0$, and the wavenumber $\alpha_{\kappa,n}$ to be found

$$c_n=-\frac{a_{12,1}-\rho_0\nu_0a_{22,1}}{a_{12,2}-\rho_0\nu_0a_{22,2}},$$
$$\alpha_{\kappa,n}^2=5\delta_p\beta\left[\left(\frac{1}{H}+\frac{\rho_0}{1-H}\right)c_n^2-\left(\frac{I_{1,2}}{H}+\frac{\rho_0I_{2,2}}{1-H}\right)c_n-\frac{I_{1,1}}{H}-\frac{\rho_0I_{2,1}}{1-H}\right].$$

Examples of wave velocities c_r and amplification factors $\alpha_\kappa c_i$ of small perturbations, are shown in Fig. 2.5. In all cases, the wave velocities c_r depend weakly on the wavenumber: $c_r=1.502$ (case B), $c_r=1.437$ (C) and $c_r=1.244$ (D).

In parallel with the results for the evolution equations (2.51), eigenvalues of the linearised problem for the full Navier-Stokes system (2.15) are also shown. It is seen that the integral method gives exact values of the wave velocities compared to the full Navier-

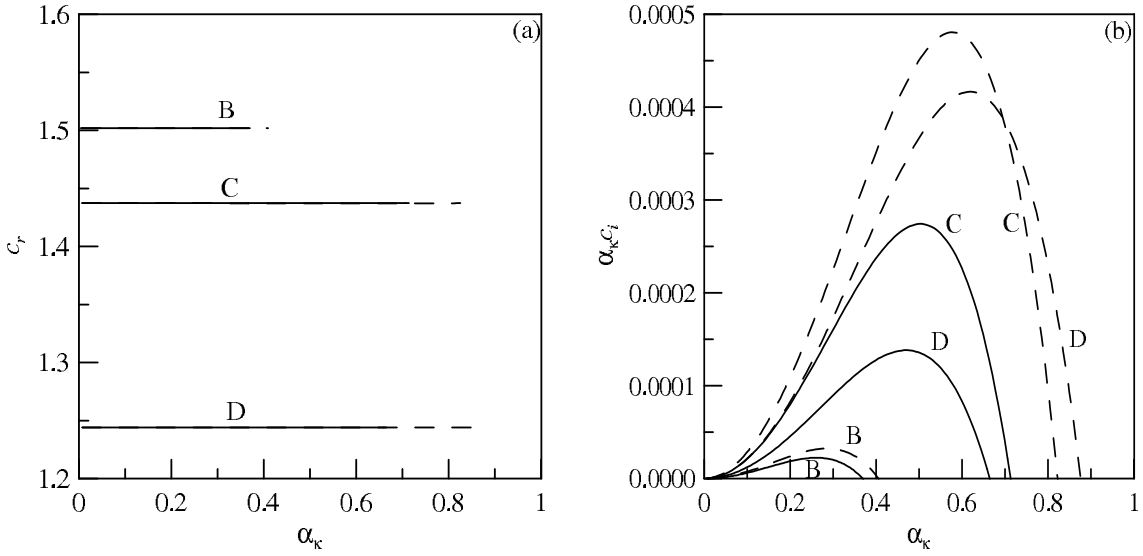

Figure 2.5: Velocities (a) and amplification factors (b) of small perturbations in cases B, C and D of Table 2.1. The solid curves denote solutions of the characteristic equation (2.56), and the dashed curves denote solutions of the linearised problem for (2.15).

Stokes problem. It is also seen that the regions of instability are approximated well, and that adequate amplification factors are obtained, which determine the stability of the numerical scheme. In case A of Table 2.1, both methods indicate stability of the waveless flow.

It is also noted that the amplification factors of the evolution system and the full system, become closer as the wavenumber α_κ is decreased. This situation is typical if similar approximations are used to model film flows, and numerous successful applications of the method have been based on the fact that relatively long waves are observed in experiments. For example, in the case of falling films, waves from the interval $\alpha \in (\alpha_{\kappa,n}/2, \alpha_{\kappa,n})$ were observed in very few experiments in contrast to numerous experiments demonstrating longer waves [46]. Using the integral method as the first approximation to the two-dimensional Navier-Stokes problem allows numerically unstable eigenmodes due to, for example, finite differences approximation and the three-dimensional pseudomodes

which appear [62], to be avoided.

Fig. 2.5 also reveals the role of the parameter δ_p: the evolution system (2.51) gives a better approximation at relatively low values of this parameter. Again, this is typically the case for evolution systems describing falling films. For example, the upper boundary of the equivalent parameter for falling films is about 0.4, and in fact, periodic steady travelling waves are not observed in experiments if the parameter exceeds this value. As follows from Fig. 2.5, for the microchannel flow studied by Zhao *et al.* [67], the model (2.51) is valid if the parameter δ_p does not exceed some value $\delta_{p,cr} \in (1.54, 2)$.

Below, examples of solutions existing for cases A and C as $\alpha_\kappa \to 0$, when the evolution system (2.51) provides a good approximation of the full Navier-Stokes system (2.15), are given.

Chapter 3

Solitary and Transitional Waves in Gravity-Driven Two-Layer Microchannel Flows

3.1 Steady travelling waves

A solitary wave is a wave which travels with constant speed, has infinite wavelength, is characterised locally by a prescribed number of oscillations, and tends to a constant at $\pm\infty$ [41, 28]. In many cases, a solitary wave can be considered as the limit long wave of a family of periodic waves of corresponding shape.

Leonid Shilnikov, a prolific Soviet scientist, proved the following theorem in a classic paper in 1965 [43]:

> *'A countable set of periodic trajectories exist in the neighbourhood of each homoclinic trajectory for a saddle-focus.'*

The aim in this chapter is to find solitary wave solutions to the evolution system, so that Shilnikov's theorem [43] may be applied, proving the existence of a countable set of periodic wave solutions existing within the neighbourhood of each solitary wave. It will

be shown that a much greater number of families of steady-travelling periodic waves exist than were found by Sisoev *et al.* [52].

The correlation between solitary waves in the physical space and homoclinic trajectories in the phase space, is discussed in more detail later in the chapter. Furthermore, in analysing the equilibrium points of the system, it is shown that only saddle-focus points are identified, corresponding to the necessary condition for Shilnikov's theorem.

In order to find steady travelling waves, a moving co-ordinate system is applied in order to maintain the same frame of reference as the wave. Therefore, solutions of (2.38) in the form $h(\xi)$ and $q^{(1)}(\xi)$ are sought, where ξ is given by

$$\xi = x_\kappa - ct_\kappa, \tag{3.1}$$

and the wave velocity c is to be found. Hence,

$$h(x_\kappa, t_\kappa) = h(\xi), \qquad q^{(1)}(x_\kappa, t_\kappa) = q^{(1)}(\xi),$$

and solitary wave solutions are found by considering $\xi \in (-\infty, \infty)$.

Substituting the replacement (3.1) into the continuity equation from (2.38) the following equation is attained,

$$-c\frac{dh}{d\xi} + \frac{dq^{(1)}}{d\xi} = 0,$$

and integrating with respect to ξ, leads to the following linear dependence of the flow rate of the first layer on its thickness,

$$q^{(1)} = q^{(1)}_\infty + ch, \tag{3.2}$$

where $q_\infty^{(1)}$ the constant of integration which arises and is determined by boundary conditions at $\pm\infty$.

Now substituting (3.1) into the second equation of (2.38), the equation for the first layer thickness h is found,

$$\begin{aligned}
&-c^2\left(1+\frac{\rho_0 h}{1-h}\right)\frac{dh}{d\xi}+\frac{d}{d\xi}\left(\frac{a_{11}^2}{3}h^3+\frac{a_{11}a_{12}}{2}h^4+\frac{a_{12}^2}{5}h^5\right)\\
&+\frac{\rho_0 h}{1-h}\frac{d}{d\xi}\left(\frac{a_{21}^2}{3}(h-1)^3+\frac{a_{21}a_{22}}{2}(h-1)^4+\frac{a_{22}^2}{5}(h-1)^5\right)\\
&=\frac{1}{5\delta b}\left[h\frac{d^3h}{d\xi^3}+\frac{2\left(a_{12}-\rho_0\nu_0 a_{22}\right)}{\gamma}h+\left(1-\rho_0\right)h\right]. \qquad (3.3)
\end{aligned}$$

3.2 Dynamical system

It is seen that equation (3.3) can be re-formulated in terms of a dynamical system if the following new variables are introduced

$$w_1=h,\quad w_2=\frac{dh}{d\xi},\quad w_3=\frac{d^2h}{d\xi^2}.$$

The equation may now be re-written in the form

$$\begin{aligned}
&\frac{dw_1}{d\xi}=w_2,\quad \frac{dw_2}{d\xi}=w_3,\quad \frac{dw_3}{d\xi}=W, \qquad (3.4)\\
&W=-\frac{2\left(a_{12}-\rho_0\nu_0 a_{22}\right)}{\gamma}-1+\rho_0+\frac{5\delta b}{w_1}\left[\frac{dW_a}{d\xi}+\frac{\rho_0 w_1}{1-w_1}\frac{dW_b}{d\xi}-c^2\left(1+\frac{\rho_0 w_1}{1-w_1}\right)w_2\right],
\end{aligned}$$

where,

$$\begin{aligned}
W_a&=\frac{a_{11}^2}{3}w_1^3+\frac{a_{11}a_{12}}{2}w_1^4+\frac{a_{12}^2}{5}w_1^5,\\
W_b&=\frac{a_{21}^2}{3}(w_1-1)^3+\frac{a_{21}a_{22}}{2}(w_1-1)^4+\frac{a_{22}^2}{5}(w_1-1)^5.
\end{aligned}$$

Using the chain rule, the derivatives which appear in the function W from (3.4) are calculated

$$\frac{dW_a}{d\xi} = \left(\frac{\partial W_a}{\partial h} + c\frac{\partial W_a}{\partial q^{(1)}}\right) w_2, \quad \frac{dW_b}{d\xi} = \left(\frac{\partial W_b}{\partial h} + c\frac{\partial W_b}{\partial q^{(1)}}\right) w_2,$$

where,

$$\begin{aligned}
\frac{\partial W_a}{\partial h} &= \frac{2a_{11}}{3}\frac{\partial a_{11}}{\partial h}w_1^3 + a_{11}^2 w_1^2 + \frac{1}{2}\left(a_{12}\frac{\partial a_{11}}{\partial h} + a_{11}\frac{\partial a_{12}}{\partial h}\right) w_1^4 + 2a_{11}a_{12}w_1^3 \\
&\quad + \frac{2a_{12}}{5}\frac{\partial a_{12}}{\partial h}w_1^5 + a_{12}^2 w_1^4, \\
\frac{\partial W_a}{\partial q^{(1)}} &= \frac{2a_{11}}{3}\frac{\partial a_{11}}{\partial q^{(1)}}w_1^3 + \frac{1}{2}\left(a_{12}\frac{\partial a_{11}}{\partial q^{(1)}} + a_{11}\frac{\partial a_{12}}{\partial q^{(1)}}\right) w_1^4 + \frac{2a_{12}}{5}\frac{\partial a_{12}}{\partial q^{(1)}}w_1^5, \\
\frac{\partial W_b}{\partial h} &= \frac{2a_{21}}{3}\frac{\partial a_{21}}{\partial h}\left(w_1-1\right)^3 + a_{21}^2\left(w_1-1\right)^2 + \frac{1}{2}\left(a_{22}\frac{\partial a_{21}}{\partial h} + a_{21}\frac{\partial a_{22}}{\partial h}\right)\left(w_1-1\right)^4 \\
&\quad + 2a_{21}a_{22}\left(w_1-1\right)^3 + \frac{2a_{22}}{5}\frac{\partial a_{22}}{\partial h}\left(w_1-1\right)^5 + a_{22}^2\left(w_1-1\right)^4, \\
\frac{\partial W_b}{\partial q^{(1)}} &= \frac{2a_{21}}{3}\frac{\partial a_{21}}{\partial q^{(1)}}\left(w_1-1\right)^3 + \frac{1}{2}\left(a_{22}\frac{\partial a_{21}}{\partial q^{(1)}} + a_{21}\frac{\partial a_{22}}{\partial q^{(1)}}\right)\left(w_1-1\right)^4 \\
&\quad + \frac{2a_{22}}{5}\frac{\partial a_{22}}{\partial q^{(1)}}\left(w_1-1\right)^5,
\end{aligned}$$

which include the following terms depending on $w_1 = h$,

$$\frac{\partial a_{11}}{\partial h}, \quad \frac{\partial a_{11}}{\partial q^{(1)}}, \quad \frac{\partial a_{12}}{\partial h}, \quad \frac{\partial a_{12}}{\partial q^{(1)}}, \quad \frac{\partial a_{21}}{\partial h}, \quad \frac{\partial a_{21}}{\partial q^{(1)}}, \quad \frac{\partial a_{22}}{\partial h}, \quad \frac{\partial a_{22}}{\partial q^{(1)}}.$$

These terms are given in Appendix (A.2), for the sake of brevity.

3.3 Homoclinic and heteroclinic trajectories

Considering the dynamical system (3.4), a fixed point $h = h_f$ is found when all derivatives vanish, leading to the right-hand-side attaining a value of zero.

A homoclinic trajectory is a solution which originates from, and returns to, the same

fixed point $h = h_f$. In the physical space, a homoclinic trajectory corresponds to a solitary wave satisfying the boundary conditions,

$$\xi \to \pm\infty : \quad h \to h_f, \quad q^{(1)} \to q_f^{(1)}.$$

A heteroclinic trajectory on the other hand, is a solution which originates from one fixed point $S_l = (h_{f,l}, 0, 0)$ and is attracted to a different fixed point $S_r = (h_{f,r}, 0, 0)$ as ξ varies from $-\infty$ to ∞, or vice versa. In the physical space, heteroclinic solutions correspond to transitional waves satisfying the following boundary conditions,

$$\begin{aligned} \xi \to -\infty : \quad & h \to h_{f,l}, \quad q^{(1)} \to q_{f,l}^{(1)}, \\ \xi \to +\infty : \quad & h \to h_{f,r}, \quad q^{(1)} \to q_{f,r}^{(1)}, \end{aligned}$$

where subscript l and r refer to the fixed point on the left- and right-hand-side of the physical space respectively. These waves are characterised by their obvious change in fluid layer thickness ahead of the wavefront, compared to behind the wave. The first layer thickness may increase or decrease depending on the course of the trajectory in the phase space. Considering the first layer, a transitional wave will be called a wave of thickening if $h_{f,l} > h_{f,r}$ since the travelling wave increases the first layer thickness. Inversely, if $h_{f,l} < h_{f,r}$ the transitional wave will be referred to as a wave of thinning.

It has already been established that the dynamical system (3.4) possesses a fixed point corresponding to the waveless flow solution (2.16). When the first layer thickness remains constant, all derivatives vanish: $w_2 = 0$, $w_3 = 0$, and $W = 0$ or equivalently,

$$\frac{2\left(a_{12} - \rho_0 \nu_0 a_{22}\right)}{\gamma} + 1 - \rho_0 = 0, \tag{3.5}$$

and according to (2.39) the solution $S_0 = (w_{1,0}, w_{2,0}, w_{3,0}) = (H, 0, 0)$, where H is the

relative thickness of the first layer for the steady flow solution (2.16), satisfies the equation (3.5). Hence the roots of the real valued function (3.5) may be found numerically using the Newton-Raphson method [2] for this specific case, and hence determine the constant $q_\infty^{(1)}$. Since $h \to H$ and $q^{(1)} \to Q^{(1)}$ as $\xi \to \pm\infty$ from (3.2), it is seen that

$$q_\infty^{(1)} = Q^{(1)} - cH, \tag{3.6}$$

and so replacing into (3.2) it is seen that

$$q^{(1)} = c\,(h - H) + Q^{(1)}. \tag{3.7}$$

In general, the non-linear equation (3.5) may have additional waveless solutions $(w_{1,f}, w_{2,f}, w_{3,f}) \equiv (h_f, 0, 0)$ where $h_f \neq H$.

To investigate asymptotic solutions in the neighbourhood of a fixed point $S_f \equiv (w_{1,f}, w_{2,f}, w_{3,f})$ of the dynamical system (3.4), solutions of the form

$$w_1 = h_f + \widehat{w}_1, \quad w_2 = \widehat{w}_2, \quad w_3 = \widehat{w}_3,$$

are sought, where the hats denote small perturbations. Substituting this solution into the dynamical system (3.4) and linearising with regards to the small perturbations, means that the system may now be written in the form

$$\frac{d\widehat{w}_1}{d\xi} = \widehat{w}_2, \quad \frac{d\widehat{w}_2}{d\xi} = \widehat{w}_3, \quad \frac{d\widehat{w}_3}{d\xi} = -k_0\widehat{w}_1 - k_1\widehat{w}_2, \tag{3.8}$$

where the coefficients k_0 and k_1, depending on the value of h_f, are given in Appendix

(A.3). The system may be written in matrix form thus,

$$\frac{d}{d\xi}\begin{pmatrix}\widehat{w}_1\\ \widehat{w}_2\\ \widehat{w}_3\end{pmatrix} = \begin{pmatrix}0 & 1 & 0\\ 0 & 0 & 1\\ -k_0 & -k_1 & 0\end{pmatrix}\begin{pmatrix}\widehat{w}_1\\ \widehat{w}_2\\ \widehat{w}_3\end{pmatrix}. \tag{3.9}$$

Hence the characteristic equation of system (3.8) is found from the determinant

$$\begin{vmatrix}-\lambda & 1 & 0\\ 0 & -\lambda & 1\\ -k_0 & -k_1 & -\lambda\end{vmatrix} = \lambda^3 + k_1\lambda + k_0 = 0. \tag{3.10}$$

Due to the absence of a quadratic term in this equation, there only exists two possible configurations for its roots: three real roots, or a real root with complex conjugate pair. In the computations below, the properties of the coefficients k_1 and k_0 indicate the second scenario:

$$\lambda_1 = \beta_r + i\beta_i, \quad \lambda_2 = \beta_r - i\beta_i, \quad \lambda_3 = -2\beta_r,$$

where the sign of β_r coincides with the sign of k_0. It is seen that the case of one real eigenvalue, with sign opposite to that of the sign of the complex pair of eigenvalues, corresponds to a saddle focus equilibrium. The general solution is given by

$$\widehat{w}_1 = E_1 e^{(\beta_r + i\beta_i)\xi} + E_2 e^{(\beta_r - i\beta_i)\xi} + E_3 e^{-2\beta_r\xi}.$$

Using Euler's formula $e^{ix} = \cos x + i\sin x$,

$$\widehat{w}_1 = E_1 e^{\beta_r\xi}\left(\cos(\beta_i\xi) + i\sin(\beta_i\xi)\right) + E_2 e^{\beta_r\xi}\left(\cos(\beta_i\xi) - i\sin(\beta_i\xi)\right) + E_3 e^{-2\beta_r\xi}$$

$$= (E_1 + E_2)e^{\beta_r \xi}\cos(\beta_i \xi) + i(E_1 - E_2)e^{\beta_r \xi}\sin(\beta_i \xi) + E_3 e^{-2\beta_r \xi}$$
$$= e^{\beta_r \xi}\left[(E_1 + E_2)\cos(\beta_i \xi) + i(E_1 - E_2)\sin(\beta_i \xi)\right] + E_3 e^{-2\beta_r \xi}.$$

Now, using the following technique,

$$a\cos x + b\sin x = \sqrt{a^2 + b^2}\left(\frac{a}{\sqrt{a^2 + b^2}}\cos x + \frac{b}{\sqrt{a^2 + b^2}}\sin x\right),$$

and letting $\cos\phi = \dfrac{a}{\sqrt{a^2 + b^2}}$ and $\sin\phi = \dfrac{b}{\sqrt{a^2 + b^2}}$ so that $\phi = \arctan\left(\dfrac{a}{b}\right)$, it is seen that

$$a\cos x + b\sin x = \sqrt{a^2 + b^2}\left(\cos\phi\cos x + \sin\phi\sin x\right)$$
$$= \sqrt{a^2 + b^2}\cos(x - \phi).$$

Hence, using the above technique, the general solution may be written as

$$\widehat{w}_1 = e^{\beta_r \xi}\sqrt{(E_1 + E_2)^2 + (E_1 - E_2)^2}\cos\left(\beta_i \xi - \phi\right) + E_3 e^{-2\beta_r \xi},$$

and reassigning the constants $\sqrt{(E_1 + E_2)^2 + (E_1 - E_2)^2}$ as E_1, and E_3 as E_2, the general solution is finally given by

$$\widehat{w}_1 = E_1 e^{\beta_r \xi}\cos\left(\beta_i \xi - \phi\right) + E_2 e^{-2\beta_r \xi}. \tag{3.11}$$

3.3.1 Homoclinic trajectories

The asymptotic behaviour of a homoclinic trajectory, is given as follows,

$$\text{For} \quad \beta_r < 0: \quad \text{if} \quad \xi \to -\infty, \quad w_1 = h \tag{3.12}$$
$$= h_f + \widehat{w}_1$$

$$
\begin{aligned}
&&&&&= h_f + E_l e^{-2\beta_r \xi}, \\
&&\text{if} \quad \xi \to +\infty, \quad & w_1 = h \\
&&&= h_f + \widehat{w}_1 \\
&&&= h_f + E_r e^{\beta_r \xi} \cos\left(\beta_i \xi - \phi\right), \\
\text{For} \quad \beta_r > 0: \quad &\text{if} \quad \xi \to -\infty, \quad & w_1 = h \\
&&&= h_f + \widehat{w}_1 \\
&&&= h_f + E_l e^{\beta_r \xi} \cos\left(\beta_i \xi - \phi\right), \\
&&\text{if} \quad \xi \to +\infty, \quad & w_1 = h \\
&&&= h_f + \widehat{w}_1 \\
&&&= h_f + E_r e^{-2\beta_r \xi}.
\end{aligned}
$$

This is an asymptotic solution, so only terms which tend to zero as $\xi \to \pm\infty$ are of interest. Terms which tend to $\pm\infty$ as $\xi \to \pm\infty$ are therefore neglected. It is seen that for β_r positive and negative, the solution exhibits different behaviour as $\xi \to \pm\infty$. In each case, one side exhibits exponentially oscillating behaviour and the other exponential behaviour.

For both cases, $\beta_r < 0$ and $\beta_r > 0$, the trajectory depends on four variables E_l, E_r, ϕ and c, where subscript l and r refer to the left-hand-side and right-hand-side versions of the variable, with three equations to satisfy: $[h] = 0$, $[h'] = 0$ and $[h''] = 0$. However, since the problem is invariant with regard to a shift along the ξ-axis, one of the variables E_l or E_r is redundant. Therefore, three variables E_l or E_r, ϕ and c may be satisfied by the three equations.

The three values have to be found from matching, at some point ξ_m, variables w_1, w_2 and w_3. Two separate numerical solutions are found using the fourth-order Runge-Kutta method, since a high accuracy is required, by integrating in the positive ξ direction from

the vicinity of the fixed point at $\xi = -\infty$, and integrating in the negative ξ direction from the vicinity of the fixed point at $\xi = +\infty$. These separate solutions are then joined at the point ξ_m.

3.3.2 Heteroclinic trajectories

In the case of a heteroclinic trajectory, the constant of integration $q_\infty^{(1)}$ from (3.2) is determined by the asymptotic conditions at $-\infty$ and ∞,

$$q_{f,l}^{(1)} = q_\infty^{(1)} + ch_{f,l},$$
$$q_{f,r}^{(1)} = q_\infty^{(1)} + ch_{f,r}.$$

Eliminating $q_\infty^{(1)}$, the wave velocity is found,

$$c = \frac{q_{f,l}^{(1)} - q_{f,r}^{(1)}}{h_{f,l} - h_{f,r}}. \tag{3.13}$$

Thus, in the case of a heteroclinic solution, the wave velocity c is found from (3.13), where the parameters of the fixed points S_l and S_r are calculated from (3.5).

Since the sign of β_r has to be taken into account for both fixed points, there are twice the number of possible cases for asymptotic behaviour of (3.11):

$$\begin{aligned}
\text{For} \quad \beta_{r,l} < 0, \quad \beta_{r,r} < 0 \quad : \qquad \text{if} \quad \xi \to -\infty, \quad w_1 &= h \\
&= h_{f,l} + \widehat{w}_1 \\
&= h_{f,l} + E_l e^{-2\beta_{r,l}\xi}, \\
\text{if} \quad \xi \to +\infty, \quad w_1 &= h \\
&= h_{f,r} + \widehat{w}_1 \\
&= h_{f,r} + E_r e^{\beta_{r,r}\xi} \cos\left(\beta_{i,r}\xi - \phi_r\right),
\end{aligned} \tag{3.14}$$

$$
\begin{aligned}
\text{For} \quad \beta_{r,l} < 0, \quad \beta_{r,r} > 0 \quad : \qquad \text{if} \quad \xi \to -\infty, \quad w_1 &= h \\
&= h_{f,l} + \widehat{w}_1 \\
&= h_{f,l} + E_l e^{-2\beta_{r,l}\xi}, \\
\text{if} \quad \xi \to +\infty, \qquad w_1 &= h \\
&= h_{f,r} + \widehat{w}_1 \\
&= h_{f,r} + E_r e^{-2\beta_{r,r}\xi}, \\
\text{For} \quad \beta_{r,l} > 0, \quad \beta_{r,r} < 0 \quad : \qquad \text{if} \quad \xi \to -\infty, \quad w_1 &= h \\
&= h_{f,l} + \widehat{w}_1 \\
&= h_{f,l} + E_l e^{\beta_{r,l}\xi} \cos\left(\beta_{i,l}\xi - \phi_l\right), \\
\text{if} \quad \xi \to +\infty, \quad w_1 &= h \\
&= h_{f,r} + \widehat{w}_1 \\
&= h_{f,r} + E_r e^{\beta_{r,r}\xi} \cos\left(\beta_{i,r}\xi - \phi_r\right), \\
\text{For} \quad \beta_{r,l} > 0, \quad \beta_{r,r} > 0 \quad : \qquad \text{if} \quad \xi \to -\infty, \quad w_1 &= h \\
&= h_{f,l} + \widehat{w}_1 \\
&= h_{f,l} + E_l e^{\beta_{r,l}\xi} \cos\left(\beta_{i,l}\xi - \phi_l\right), \\
\text{if} \quad \xi \to +\infty, \quad w_1 &= h \\
&= h_{f,r} + \widehat{w}_1 \\
&= h_{f,r} + E_r e^{-2\beta_{r,r}\xi}.
\end{aligned}
$$

So, for the case of a heteroclinic solution, there are four equations to satisfy: $[h] = 0$, $[h'] = 0$, $[h''] = 0$ and (3.13). Therefore, four variables are required in order to satisfy them. It can be seen that the case when $\beta_{r,l} > 0$ and $\beta_{r,r} < 0$ is the only feasible way to achieve this, since there are five variables, E_l, E_r, ϕ_l, ϕ_r and c, of which either E_l, E_r is redundant due to the invariance with regard to a shift in ξ. Therefore, for $\beta_{r,l} > 0$ and

$\beta_{r,r} < 0$, there are four variables which must satisfy four equations. Again, these values are found by matching the functions w_1, w_2 and w_3 at some point ξ_m.

It is seen that the other cases for $\beta_{r,l}$ and $\beta_{r,l}$ are impossible, however at some specific values of the parameters, further heteroclinic solutions may also exist.

3.4 Results

3.4.1 Similarity parameters

The similarity parameters ρ_0 and ν_0 characterize the relative properties of the fluids, and are therefore constant for a given liquid-liquid system. Below, results are presented for a water-benzene system. The combination of these two fluids yields typical ratios of densities and viscosities. The properties are as follows,

$$\rho_w = 1 \text{ g cm}^{-3}, \qquad \nu_w = 1.138 \text{ cm}^2 s^{-1},$$
$$\rho_b = 0.881 \text{ g cm}^{-3}, \qquad \nu_b = 0.829 \text{ cm}^2 s^{-1},$$

which gives the following values for the ratios of densities and viscosities, and the Kapitza number,

$$\rho_0 = 0.881, \qquad \nu_0 = 0.728, \qquad \text{Ka} = 2850.$$

The relative thickness of the first layer belongs to the interval $h_0 \equiv H \in (0, 1)$, and the film parameter δ is bounded by the condition $\kappa^2 \ll 1$, see (2.21), for given values of Ka and h_0. The dependence $\kappa^2(\delta)$ for a range of values of h_0 is shown in Fig. 3.1a. Considering the bottom right vicinity of Fig. 3.1(a), it is seen that $\kappa^2 \leqslant 0.2$ if $\delta \leqslant 2$ and $h_0 \geqslant 0.4$. In the case of a falling film [46, 48], similar values of the stretching parameter κ^2 provide good agreement with experiments, and it is expected that the model (2.38) is

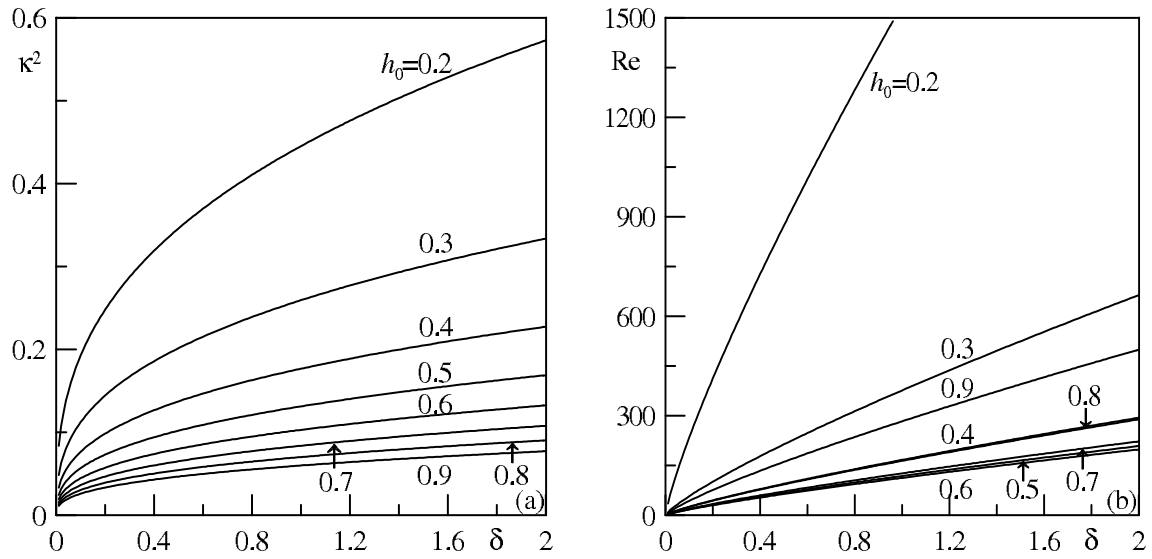

Figure 3.1: Dependence of the stretching parameter κ^2 (a) and the Reynolds number Re (b) on the film parameter δ.

also an adequate approximation of the full Navier-Stokes system (2.15) for such values of κ^2. Decreasing h_0 leads to a shortening of the interval of values of δ where the evolution model (2.38) is applicable.

Dependence of the Reynolds number Re on the film parameter δ, is given in Fig. 3.1(b), and it is seen that the evolution model can be applied up to $\mathrm{Re} \leqslant 300$. For instance, if $\delta = 2$ and $h_0 = 0.4$, then the value $\kappa^2 = 0.23$ is received at $\mathrm{Re} = 294$, and this case corresponds to a microchannel of width $H_c = 0.082$ cm, where the first layer thickness $H_c^{(1)} = 0.033$ cm and the average velocity $U_c = 36$ cm/s.

3.4.2 Fixed points

Examples of fixed points of the dynamical system (3.4), for different first layer thicknesses and different regions of the parameter δ, are shown in Figs. 3.2 and 3.3. It is seen that the stability depends on the sign of β_r, see (3.11), and determines the type of behaviour seen as $\xi \to \pm\infty$, either exponentially oscillating or exponential.

In parallel with the fixed points $S_0 = (h_0, 0, 0)$, which are independent of the ve-

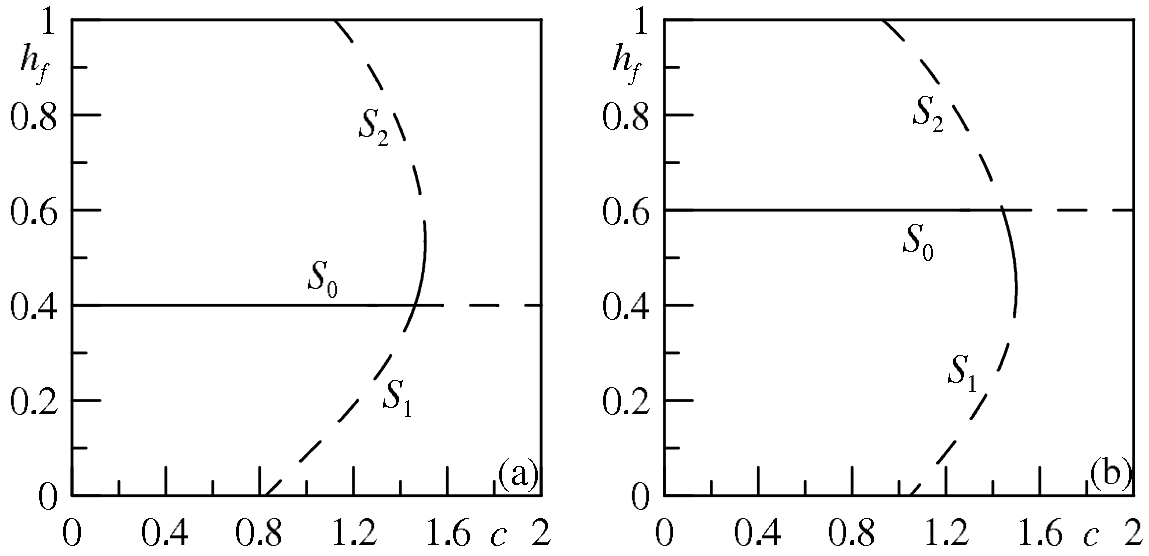

Figure 3.2: Fixed points at $\delta = 1$: (a) $H = 0.4$, (b) $H = 0.6$. Solid and dashed curves denote branches corresponding to $\beta_r < 0$ and $\beta_r > 0$ respectively.

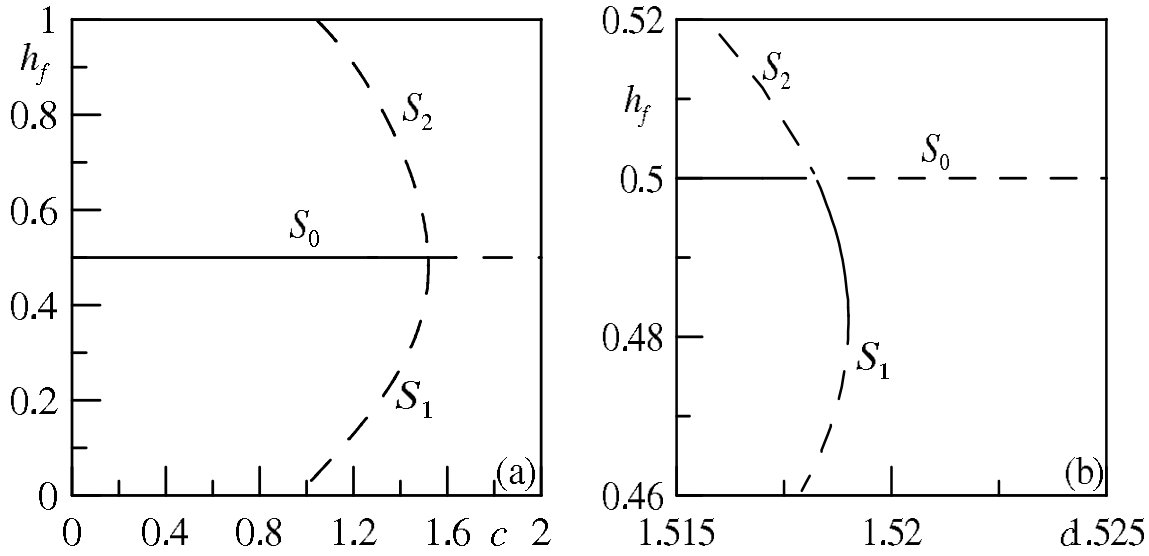

Figure 3.3: Fixed points at $\delta = 1$ and $H = 0.5$: (a) $\delta \in [0, 2]$, (b) $\delta \in [1.515, 1.525]$. Solid and dashed curves denote the fixed points with $\beta_r > 0$ and $\beta_r < 0$ respectively.

locity c, there are fixed points on the curve $S_1 \cup S_2$ in the plane (c, h_f), where $S_1 = \{(h_1, 0, 0), h_1 \in (0, h_m)\}$ and $S_2 = \{(h_2, 0, 0), h_2 \in (h_m, 1)\}$ are two sets of the fixed points, and (c_m, h_m) is the fixed point with the maximum velocity c in $S_1 \cup S_2$.

In the plane (c, h_f), the curves S_0, S_1 and S_2 are shown by solid and dashed pieces corresponding to positive and negative values of β_r respectively. It is seen that for the curve S_0, $\beta_r > 0$ and $\beta_r < 0$ for the cases $c < c_0$ and $c > c_0$ respectively, where the point (c_0, h_0) is an intersection of the curves S_0 and $S_1 \cup S_2$. The sign of β_r changes twice along the curve $S_1 \cup S_2$.

3.4.3 Solitary and transitional waves

In this section, homoclinic and heteroclinic trajectories of the dynamical system (4.3) are presented for the case $\delta = 1$ and $H = 0.5$ (Fig. 3.3). In parallel, the corresponding solitary and transitional waves in the physical space are discussed.

Solitary waves in falling films were first described in an experimental context by Kapitza and Kapitza [25], and as further publications on the topic [7, 46, 47] revealed more examples, a classification of the types of solitary waves was introduced. All solitary waves on the surface of a falling film can be separated into two groups: slow waves and fast waves. Their classification depends on whether their velocity is smaller or larger than the velocity of the neutral linear wave[1], which has double the liquid velocity at the free surface in the case of the waveless flow [48]. The slowest and fastest waves are traditionally referred to as waves of the first and second families, respectively, and the solitary wave of the so-called first family was first calculated by Shkadov [45].

Since the two-layer microchannel flow can be reduced to the case of the falling film by variation of the physical or similarity parameters, the solitary waves found in falling films

[1]The neutral linear wave is a periodic wave with velocity of the form $c = c_r + ic_i$, when the complex part $c_i = 0$. Shorter waves, such as periodic waves, are more stable than long waves since capillarity dampens them. There exists a wavelength where perturbations neither grow or decay, and this wave length is described as 'neutral'.

may also exist in microchannel flows. However, there is a critical difference between the two flows since the falling film case exhibits only two fixed points, S_0 and S_1, or, S_0 and S_2, which can exist at any value of the velocity c under the condition $h_1 > 0$ or $h_2 > 0$ [7], and the homoclinic and heteroclinic trajectories appear as a balance of attracting and repelling properties of these two fixed points. In the case of the two-layer microchannel flow, three fixed points exist for $c < c_m$ but only one exists for $c > c_m$, therefore different solitary and transitional waves are expected to be computed for the microchannel flow in comparison with the falling film case.

3.4.4 Trajectories originating from the fixed point S_0

Firstly, trajectories leaving the neighbourhood of the fixed point S_0 for velocities $c < c_0$ are discussed. Since $\beta_r > 0$ for these values of c, according to (3.12) the asymptotics of the trajectories belong to the two-parametric surface at $\xi \to -\infty$ and the one-parametric curve at $\xi \to \infty$.

The minimum value of the velocity c at which a homoclinic trajectory exists has been found to be $c = 1.480934$. With the argument ξ increasing from $-\infty$ to ∞, the trajectory shown in Fig. 3.4(a) passes a loop in the phase space which is approximately bounded by the values h_1 and h_0 along the h-axis. This indicates that the trajectory is primarily controlled by the fixed points S_0 and S_1.

In the physical space, the wave shape shown in Fig. 3.5(a) is typical of a solitary wave of the first family [45] (see also [48]), where the velocity of this wave is denoted as $c_{-1,1}$. Furthermore, a wave comparable to a slow solitary wave of velocity $c_{-1,2}$ in the falling film [48], has been calculated for the microchannel flow. This wave is shown in Fig. 3.5(d), and exists for the velocity $c = 1.481022$ and possesses a second large oscillation in comparison with the wave in Fig. 3.5(a). In the phase space, see Fig. 3.4(d), the trajectory passes along two closed loops before returning to the fixed point S_0. Similar to the case of

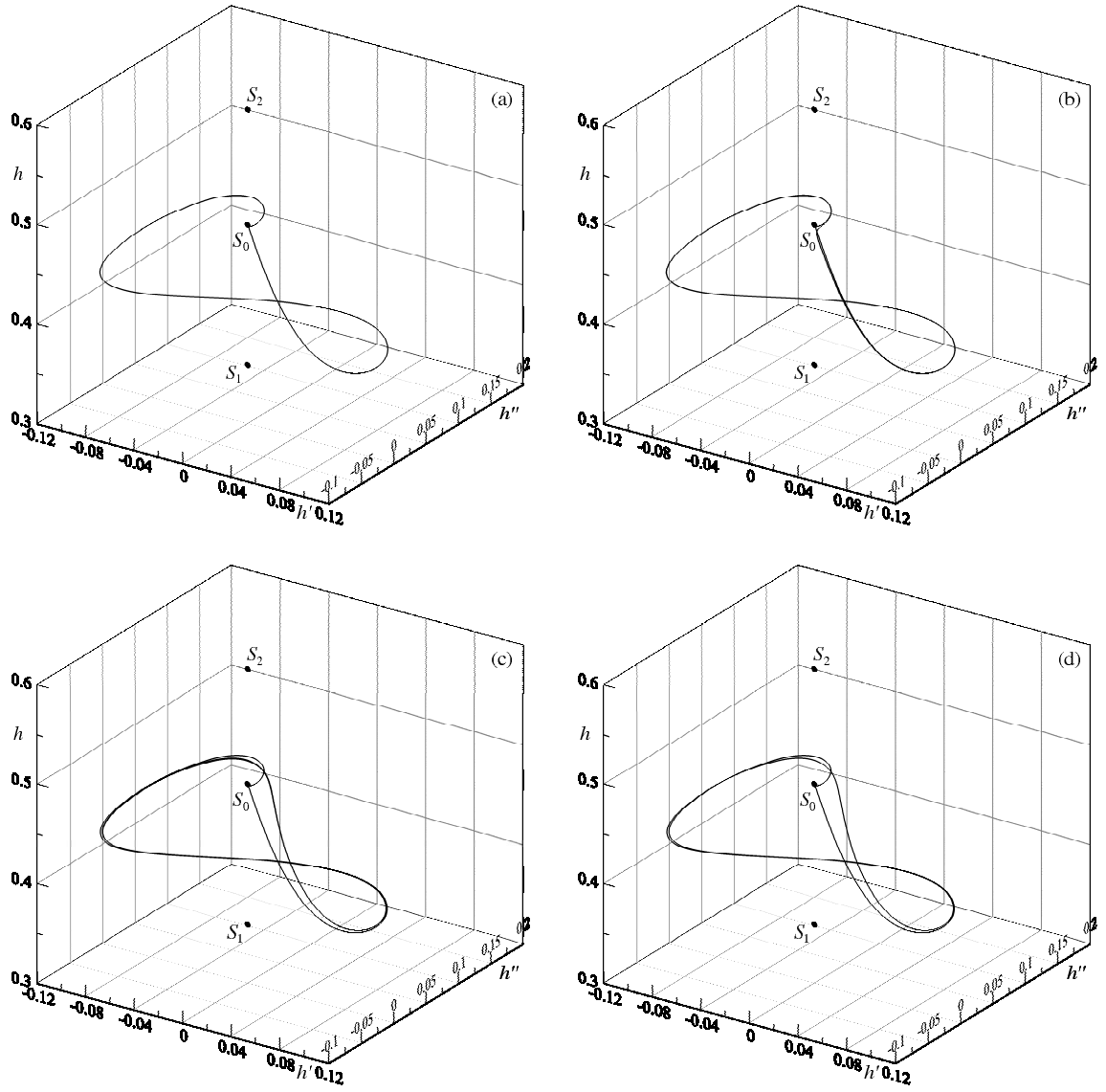

Figure 3.4: Homoclinic trajectories for the fixed point S_0: (a) $c = 1.480934$, (b) $c = 1.480934$, (c) $c = 1.481020$, (d) $c = 1.481022$.

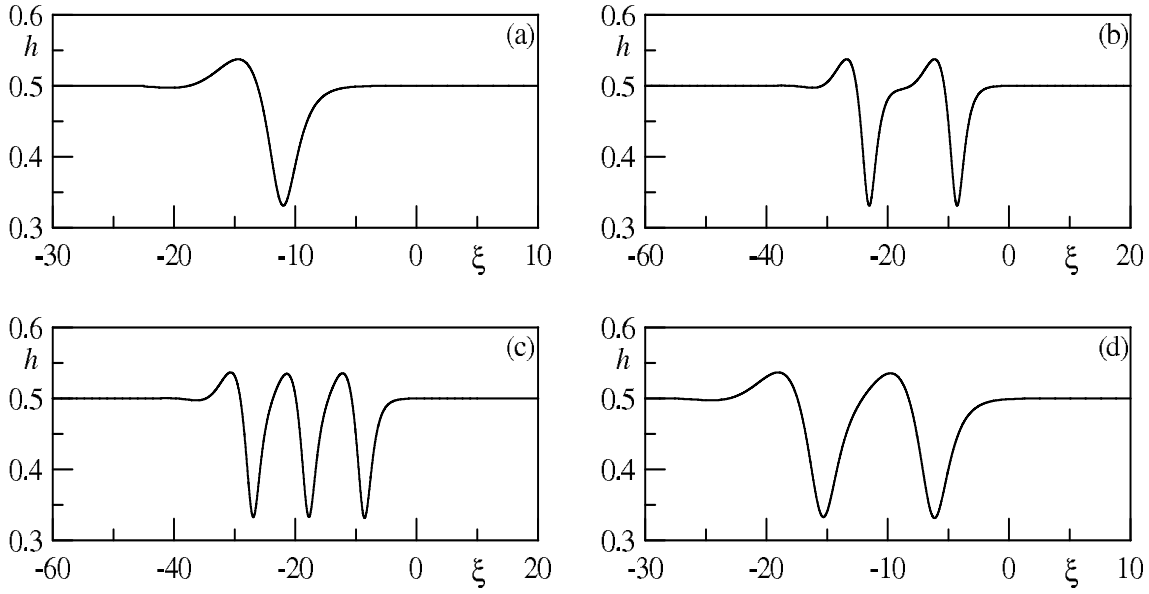

Figure 3.5: Solitary waves for the homoclinic trajectories shown in the panels of Fig. 3.4, respectively.

the falling film, there are additional solitary waves attaining velocities between those of the waves shown in Figs. 3.5(a) and (d). These more complex waves have intermediate oscillations, examples of which are plotted in Figs. 3.5(b) and (c).

It is seen that the solution shown in panels (b) of Fig. 3.4 and Fig. 3.5, which is computed for a velocity c close to that of the solutions shown in panels (a) of Fig. 3.4 and Fig. 3.5, display two almost identical oscillations. This can be seen from the phase space diagram in Fig. 3.4(b), where the trajectory follows an almost duplicate path on the second loop as the first. On the other hand, the solution given in panels (c) of Fig. 3.4 Fig. 3.5 is close to the solution given in panels (d) of Fig. 3.4 and Fig. 3.5, but has an additional loop of the trajectory, and in the physical space, a corresponding oscillation of the wave shape.

By increasing the velocity c, the fixed points S_2 and S_1 approach the fixed point S_0, see Fig. 3.2 and Fig. 3.3. The trajectories originating from the fixed point S_0 are now more likely to be attracted to either S_1 or S_2, resulting in a heteroclinic trajectory. Two

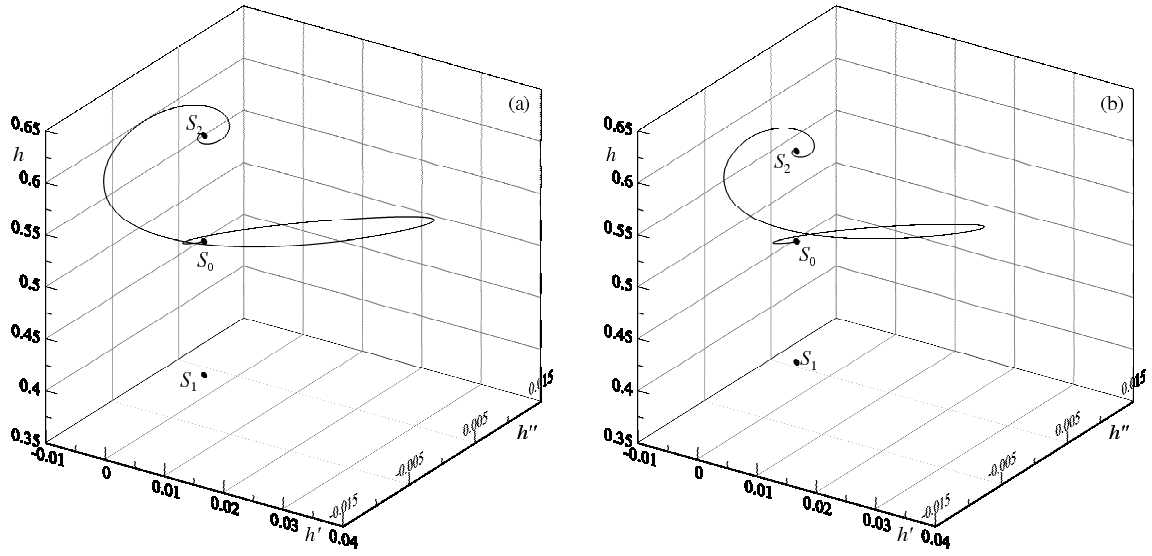

Figure 3.6: Heteroclinic trajectories from the fixed point S_0 to the fixed point S_2: (a) $c = 1.488254$, (b) $c = 1.495018$.

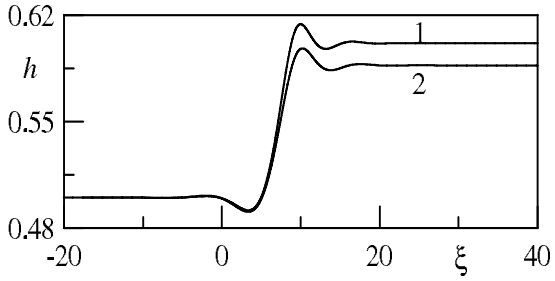

Figure 3.7: Transitional waves for the heteroclinic trajectories shown in panel a (curve 1) panel (b) (curve 2) of Fig. 3.6.

examples of trajectories from S_0 to S_2 are shown in Fig. 3.6.

Similar to the homoclinic trajectories discussed above, heteroclinic trajectories leave the neighborhood of S_0 along the 2D-unstable surface but, are attracted into the stable spiral of the fixed point S_2. However, these trajectories traverse it in the opposite direction compared with the homoclinic trajectories. It is also seen that the heteroclinic trajectories are primary located between the surfaces $h = h_0$ and $h = h_2$, in contrast to the homoclinic trajectories in Fig. 3.4. The corresponding transitional wave shapes of the heteroclinic trajectories discussed above, are presented in the physical space in Fig. 3.7.

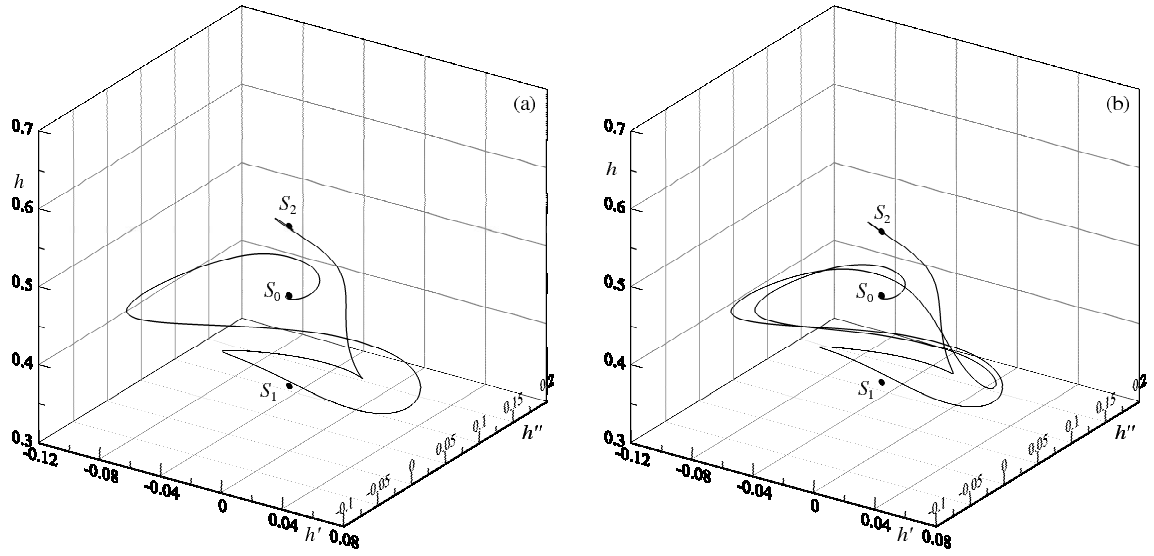

Figure 3.8: Heteroclinic trajectories from the fixed point S_0 to the fixed point S_2: (a) $c = 1.494813$, (b) $c = 1.497202$.

These transitional waves correspond to a displacement of the more viscous and more dense first layer liquid by the second layer liquid. This type of wave is often referred to as a 'shock wave in a microchannel' [34]. However, the term 'transitional wave' seems more appropriate as the problem has a linear scale based on the channel width, and the transition interval between the limit values of the interface, in particular the cases h_0 and h_1, is on a much larger scale than that of a shock wave.

There are other, more complicated types of heteroclinic trajectories which appear as a result of a balance of the attracting and repelling properties of all three fixed points. Two of such solutions are given in Fig. 3.8. The trajectory in Fig. 3.8(a) leaves the neighbourhood of the fixed point S_0 and passes a loop in a manner similar to that of the homoclinic trajectory in Fig. 3.4(a) but closer to the fixed point S_1, and then after two turns, approaches the fixed point S_2. The shape of this wave, plotted in the physical space in Fig. 3.9(a), is very similar to the solitary wave of velocity $c_{-2,1}$ in the falling film [48], except when the variable ξ attains large values.

The trajectory in Fig. 3.8(b) passes along an additional large loop around the fixed

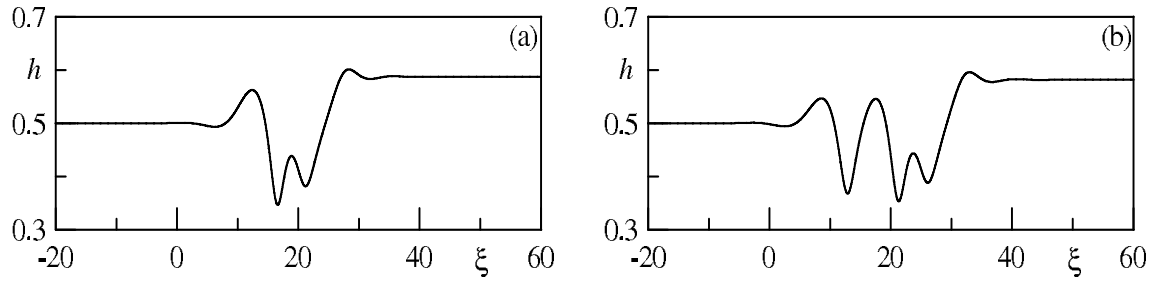

Figure 3.9: Transitional waves for the heteroclinic trajectories shown shown in the panels of Fig. 3.8, respectively.

point S_0 before approaching S_1, and after a further two turns, arrives within the neighbourhood of the fixed point S_2. The initial stage of the trajectory in Fig. 3.8(b) is similar to the homoclinic trajectory in Fig. 3.4(d), and further comparisons can be made with the shape of the wave with velocity $c_{-2,2}$ in the falling film case [48] when considering the physical space in Fig. 3.9(b).

There are also examples of trajectories which originate from the fixed point S_0 and arrive within a small neighbourhood of the fixed point S_2, similar to Fig. 3.6, but are not fully attracted to the fixed point. The majority of these trajectories do not form homoclinic or heteroclinic trajectories, however, some of them do find their way to the fixed point S_1 as a result of the intersection of the 1D unstable manifold of the fixed point S_2 and the 2D stable manifold of the fixed point S_1. Two examples of such trajectories are presented in Fig. 3.10.

Again, the trajectory in Fig. 3.10(a) initially traces the path of a more simple heteroclinic trajectory. As in Fig. 3.6(a), the trajectory is firstly attracted to the small vicinity around S_2, before leaving this neighbourhood and arriving at the fixed point S_1, which is a stable focus on the corresponding surface containing this point. In the physical plane, the solution given in Fig. 3.11(a) is in very close agreement with the wave given in Fig. 3.7 when ξ varies from $-\infty$ to some intermediate value $\xi < \infty$, but instead of retaining the increased first layer thickness, there is a steep wavefront with preceding ripples due to the

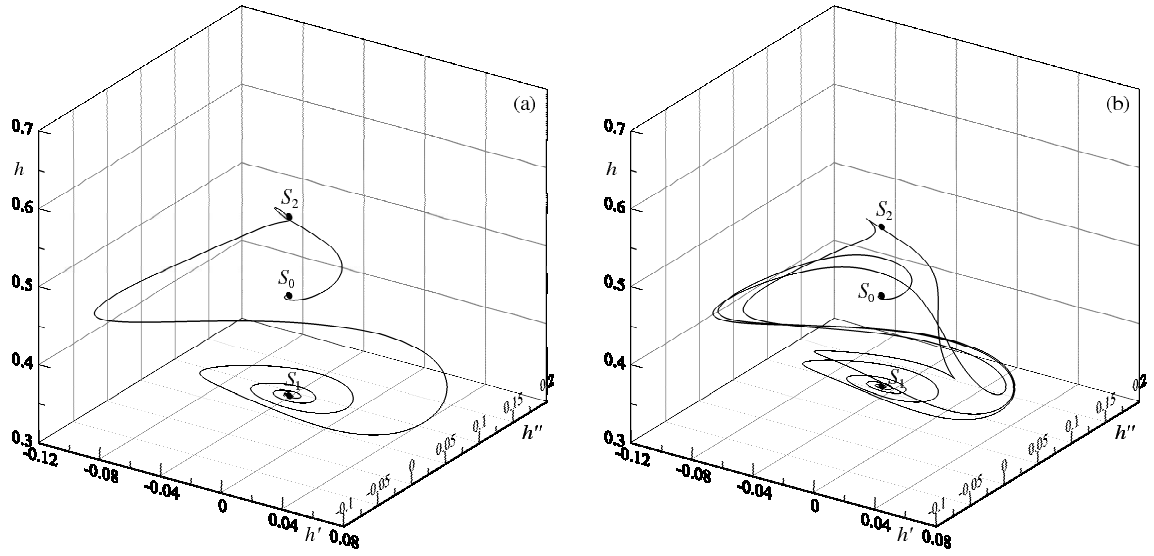

Figure 3.10: Heteroclinic trajectories from the fixed point S_0 to the fixed point S_1: (a) $c = 1.488254$, (b) $c = 1.494568$.

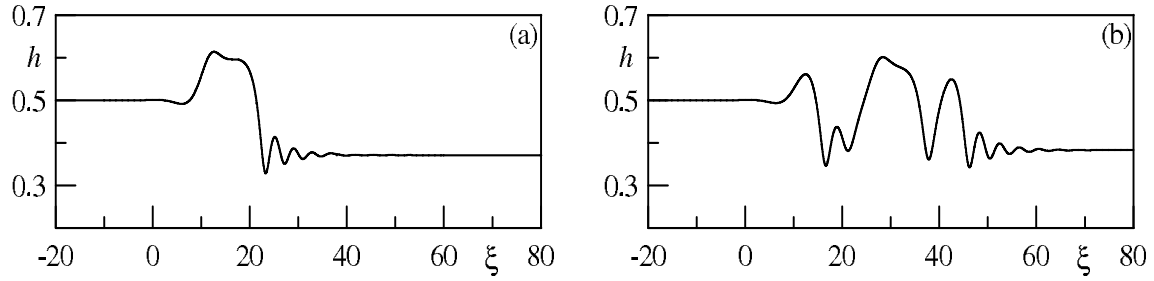

Figure 3.11: Transitional waves for the heteroclinic trajectories shown shown in the panels of Fig. 3.10, respectively.

attraction of the fixed point S_1. It is seen that although the wave shapes initially look similar, these two trajectories result in drastically different wave profiles, namely a wave of thickening and a wave of thinning, respectively.

Another example of a trajectory passing within a small neighbourhood of the fixed point S_2 before arriving at the fixed point S_1, is shown in Fig. 3.10(b). This trajectory closely follows the trajectory in Fig. 3.8(a) for the first section from S_0 up to S_2 travelling along the 1D unstable manifold, but then is attracted to the 2D stable manifold of the fixed point S_1. As an augmentation of the case given in Fig. 3.10(a), the trajectory displays an

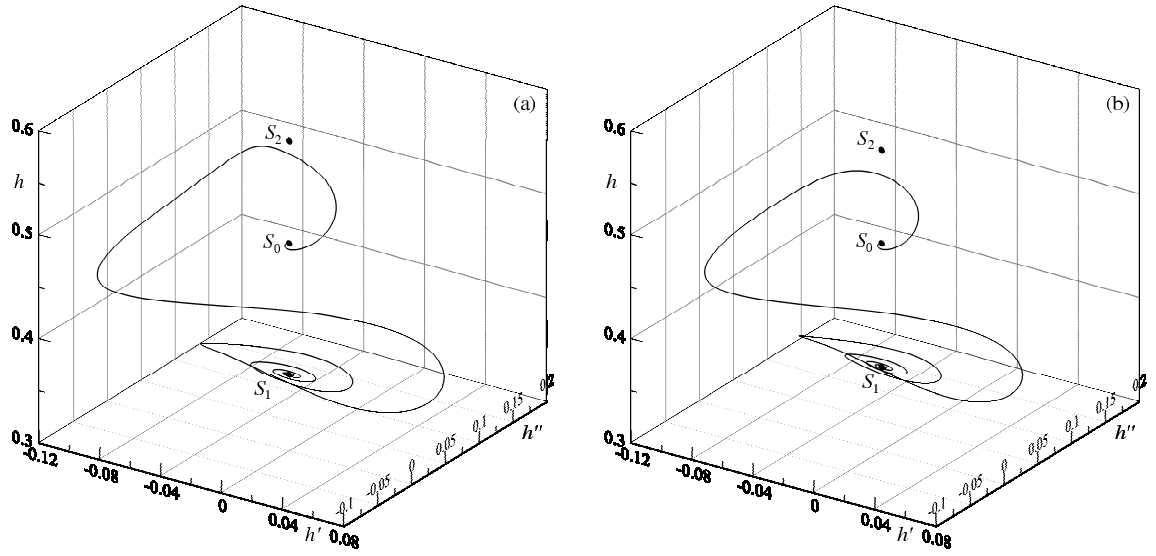

Figure 3.12: Heteroclinic trajectories from the fixed point S_0 to the fixed point S_1: (a) $c = 1.489767$, (b) $c = 1.493753$.

additional large loop around S_0 and S_1, before approaching the fixed point S_1. The wave shape given in Fig. 3.11(b) is similar to the wave in Fig. 3.9(a) for $\xi \in (-\infty, 30)$, but has a large front hump and preceding ripples.

The alternative case for heteroclinic trajectories, namely those traversing between the fixed points S_0 and S_1 are presented in Fig. 3.12. In both cases, the trajectories leave the 2D unstable manifold of the fixed point S_0, and are attracted to the 2D stable manifold of the fixed point S_1 traversing a spiral, without visiting the 1D unstable manifold of the fixed point S_2. The transitional waves plotted in Fig. 3.13 have a large sharp front with preceding ripples. Physically, these transitional waves describe the displacement of the less viscous and less dense second liquid by the first.

Heteroclinic trajectories from S_0 to S_1 may also display features as a result of the combined influence of all fixed points. Examples of trajectories with one and two additional large loops are shown in Fig. 3.14.

In the physical space Fig. 3.15, the wave shapes include one or two large humps with preceding ripples.

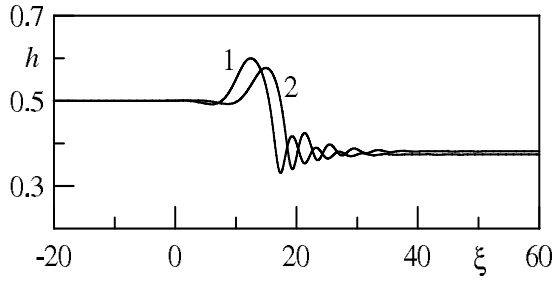

Figure 3.13: Transitional waves for the heteroclinic trajectories shown in panel a (curve 1) panel (b) (curve 2) of Fig. 3.12.

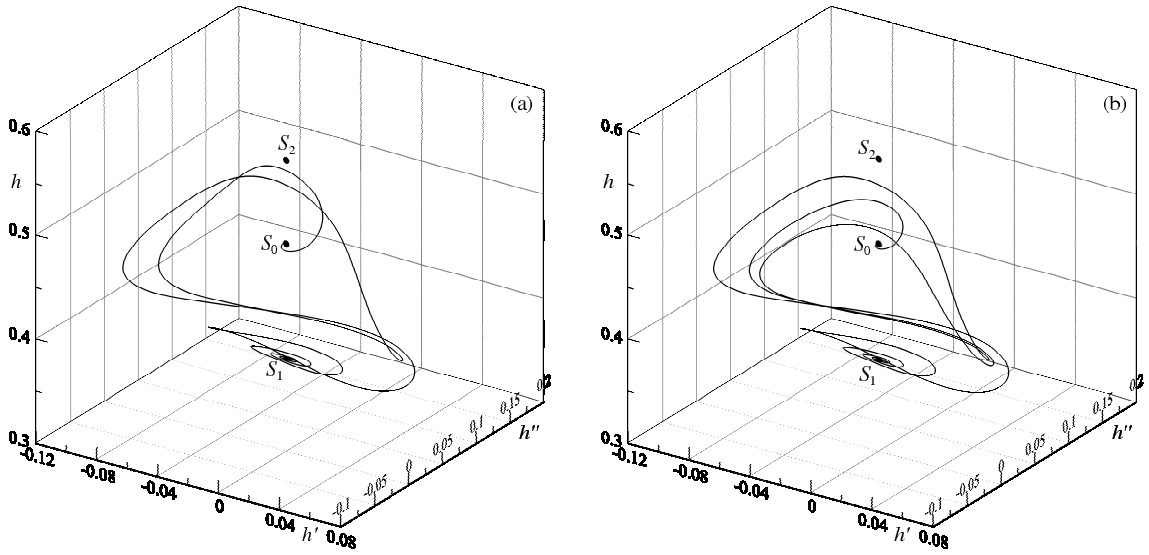

Figure 3.14: Heteroclinic trajectories from the fixed point S_0 to the fixed point S_1: (a) $c = 1.497711$, (b) $c = 1.497257$.

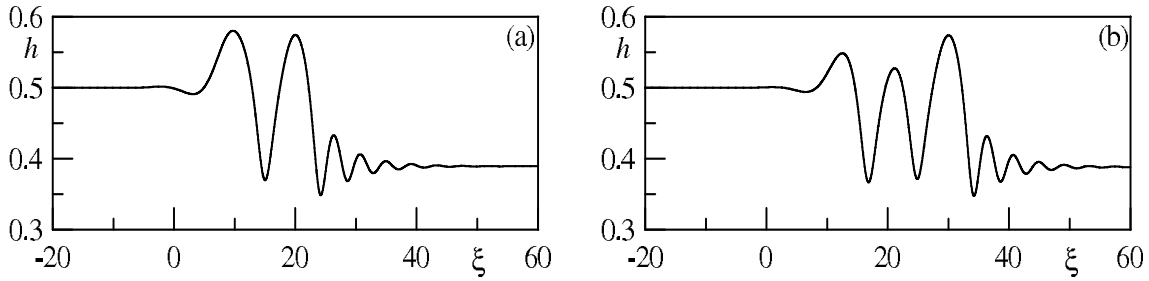

Figure 3.15: Transitional waves for the heteroclinic trajectories shown shown in the panels of Fig. 3.14, respectively.

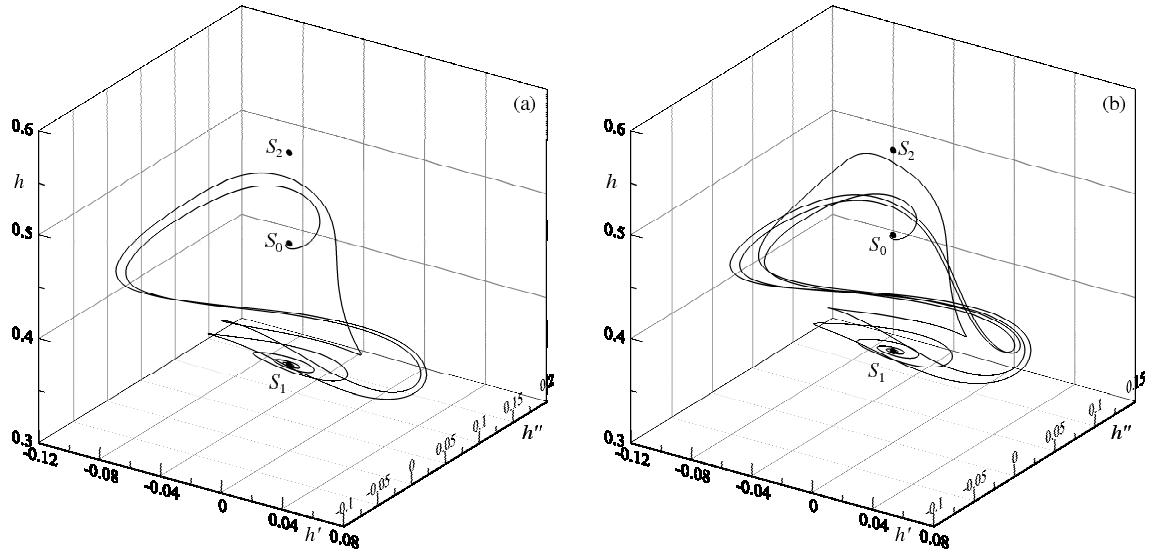

Figure 3.16: Heteroclinic trajectories from the fixed point S_0 to the fixed point S_1: (a) $c = 1.494759$, (b) $c = 1.497204$.

The delicate balance between the attracting and repelling properties of the fixed points leads to many more complicated trajectories. For example, there are heteroclinic trajectories which occur at values of the velocity c from the interval bounded by velocities corresponding to trajectories with and without large loops, Fig. 3.14 and Figs. 3.10 and 3.12, respectively. Two examples of such trajectories are given in Fig. 3.16.

The trajectory shown in Fig. 3.16(a) has an additional small loop in the neighbourhood of the fixed point S_1 in comparison with the trajectory in Fig. 3.14(a). The trajectory in Fig. 3.16(a) also displays an additional large loop due to its path through the domain of influence of the three fixed points.

Furthermore, comparing the trajectory in Fig. 3.16(a) with that in Fig. 3.8(a), it is seen that both trajectories initially approach the neighbourhood of S_1, however the latter trajectory is attracted to the fixed point S_2 and the former trajectory, after passing through additional loops, is attracted to the stable spiral S_1. This behaviour is also demonstrated in the physical plane Figs. 3.9(a) and 3.17(a). The shape of the wave corresponding to the trajectory in Fig. 3.16(b) exhibits a complicated combination of

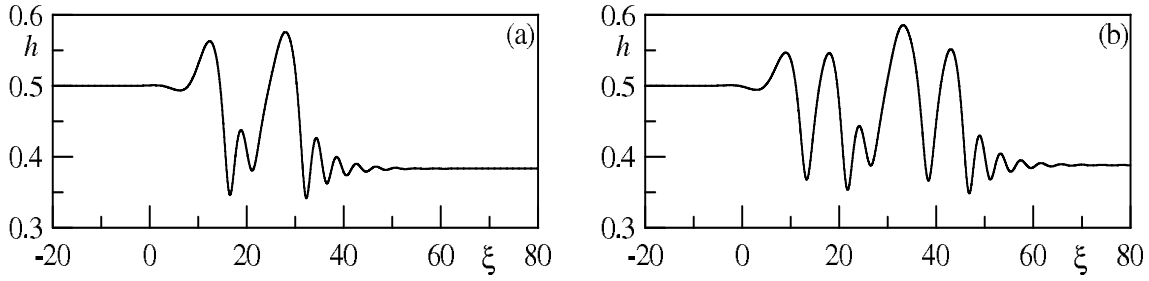

Figure 3.17: Transitional waves for the heteroclinic trajectories shown shown in the panels of Fig. 3.16, respectively.

large and small oscillations, providing transition from h_0 to h_1.

All velocities of the presented heteroclinic trajectories originating from S_0, belong to the interval $c \in (1.488254, 1.497711)$. For such values of the velocity, solitary waves have not been found. Despite this, increasing the velocity further leads to the formation many new solitary waves. Trajectories of these waves may be grouped together based on their oscillations.

Four examples of similar trajectories are shown in Fig. 3.18. In all cases, the trajectory leaves the saddle-focus S_0 along the 2D unstable manifold and passes a large loop around the fixed point S_0, each time returning to within the neighbourhood of the fixed point S_2. Following this, the trajectory traverses a path to the neighbourhood of the fixed point S_1, and after two oscillations, returns to the fixed point S_0.

The trajectories are reminiscent of the heteroclinic trajectory from S_0 to S_2 shown in Fig. 3.8(b) but differ at the final stage. Comparing the solitary waves in Figs. 3.19 and the transitional wave in Fig. 3.9(b), it is seen that although the velocities of the regimes are close and the initial waves shapes are very similar, it is possible for the corresponding trajectory to differ in the final stage.

Four examples of homoclinic trajectories with two large loops are presented in Fig. 3.20. All trajectories pass three times within the neighbourhood of the fixed point S_2, and after passing through two turns on the 2D unstable manifold of the fixed point S_1, arrive back

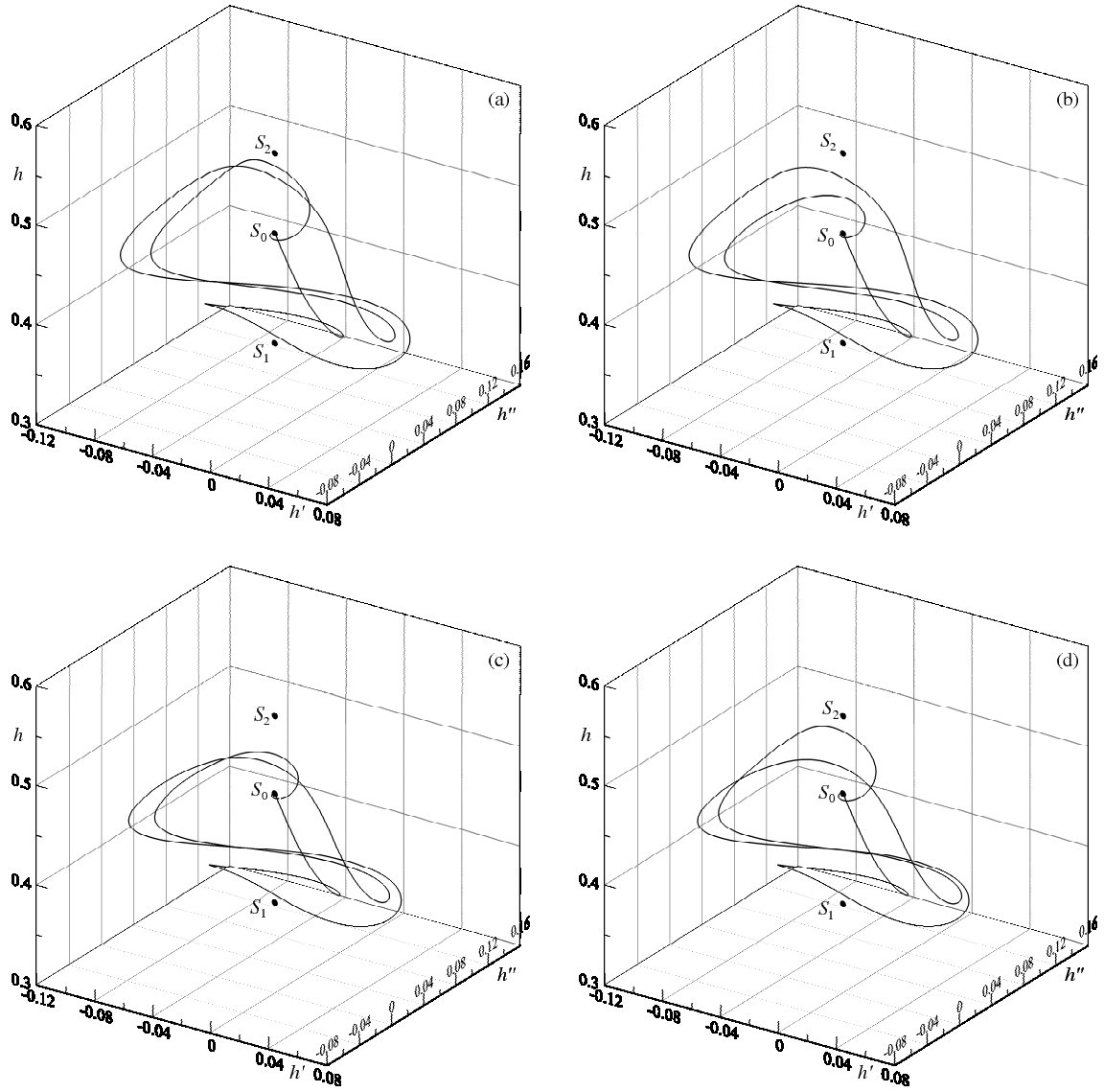

Figure 3.18: Homoclinic trajectories for the fixed point S_0: (a) $c = 1.497830$, (b) $c = 1.497860$, (c) $c = 1.498509$, (b) $c = 1.498557$.

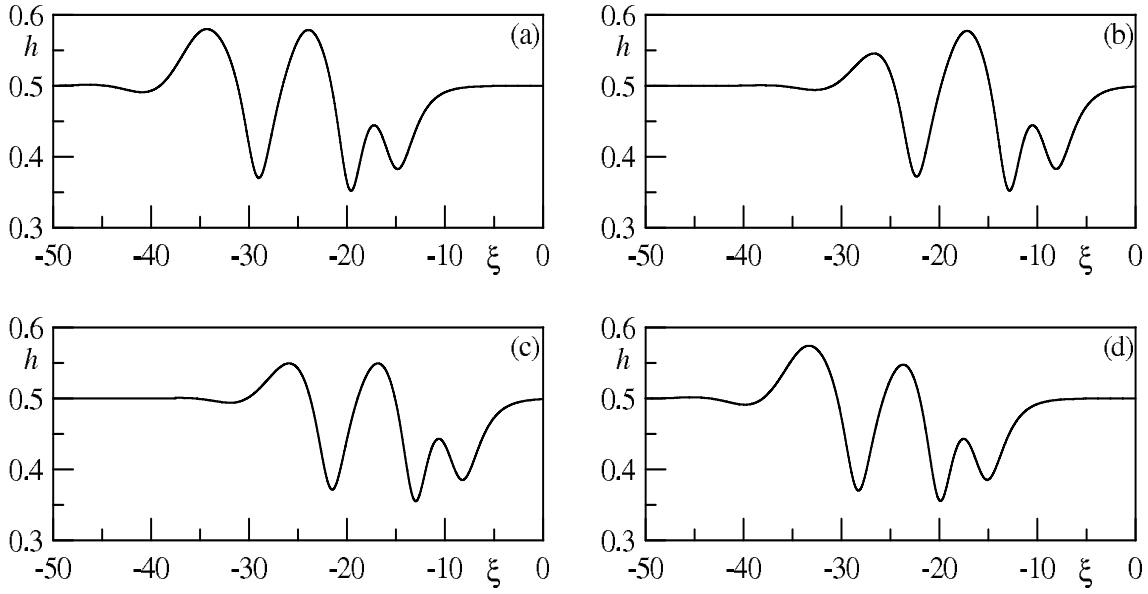

Figure 3.19: Solitary waves for the homoclinic trajectories shown in the panels of Fig. 3.18, respectively.

at the saddle point S_0. The trajectories shown here are very similar to the heteroclinic trajectory in Fig. 3.14(b), but lack the two final turns in the neighbourhood of the fixed point S_1, which describes a stable spiral, as they are this time attracted to fixed point S_0. The similarity is confirmed by comparing the wave shapes in Fig. 3.21 and Fig. 3.15(b): in all examples, two large humps are observed.

In parallel with the homoclinic trajectories shown in Figs. 3.18 and 3.20, there are many other homoclinic trajectories with close values of velocity c, some of which are given in Fig. 3.22. All examples have similar structures including large loops around the saddle point S_0 under the influence of the fixed points S_1 and S_2, and turns within the neighbourhood of S_1, before returning back to S_0. In the physical space, see Fig. 3.23, the solutions have varying combinations of large and small oscillations.

By increasing the velocity c up to c_0, the trajectories and corresponding wave shapes become more diverse. For example, both heteroclinic trajectories shown in Fig. 3.24 are confined to the domain between the fixed points S_0 and S_2. Although both trajectories

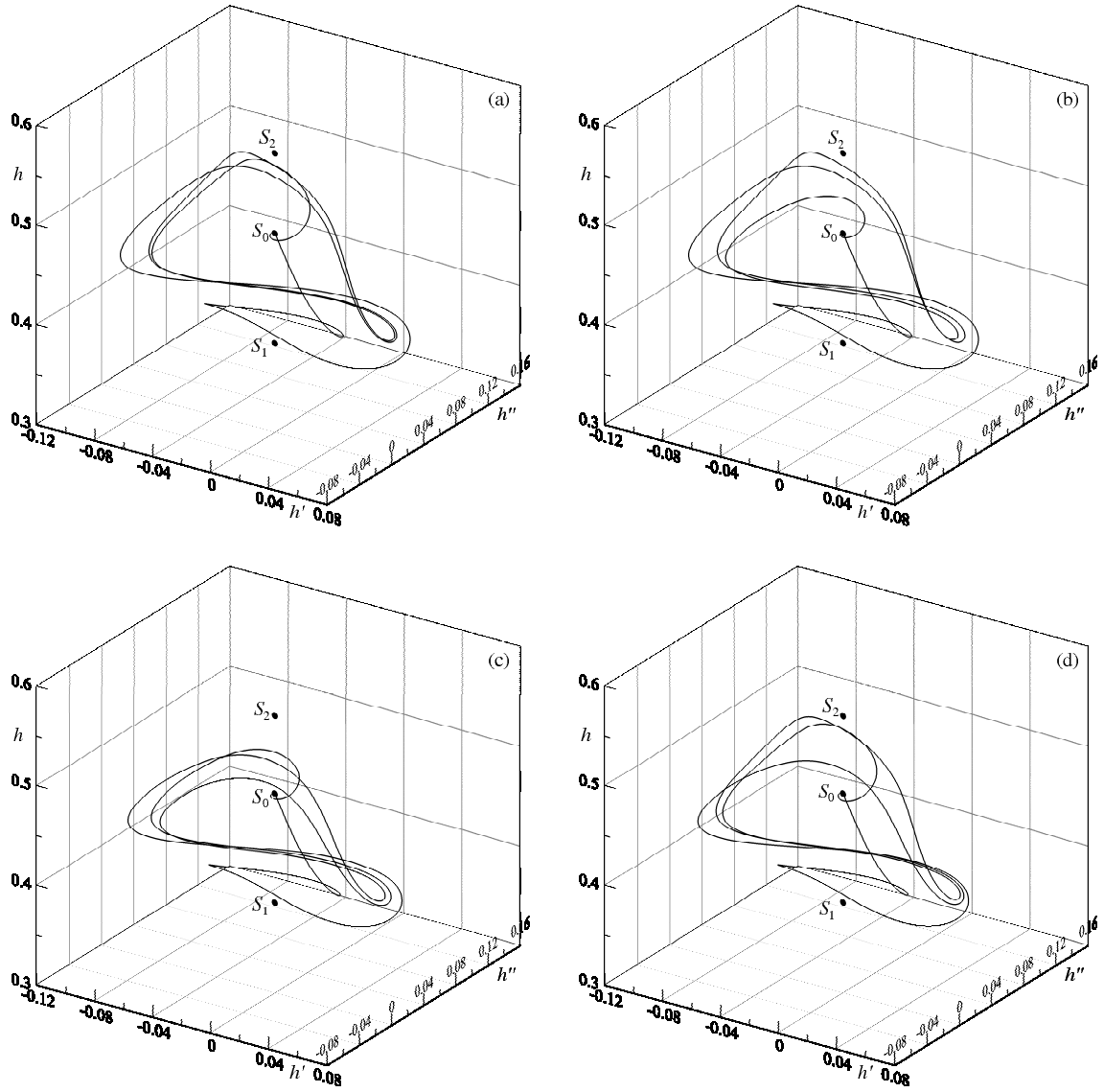

Figure 3.20: Homoclinic trajectories for the fixed point S_0: (a) $c = 1.497819$, (b) $c = 1.497820$, (c) $c = 1.498453$, (b) $c = 1.498557$.

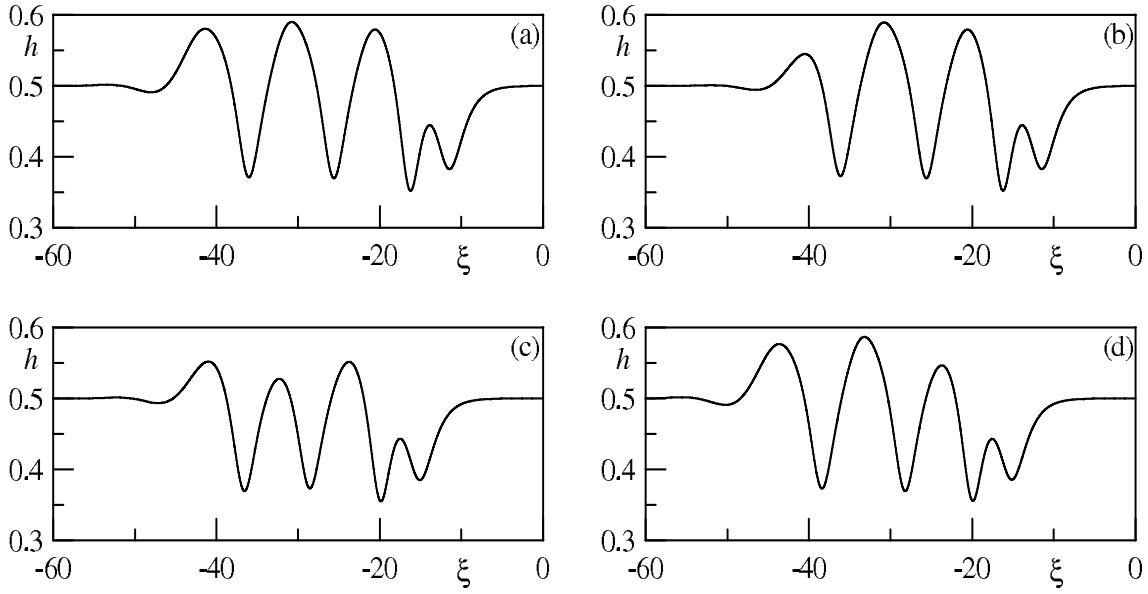

Figure 3.21: Solitary waves for the homoclinic trajectories shown in the panels of Fig. 3.20, respectively.

experience many loops within this domain, the trajectory in panel (a) looks chaotic in contrast to the trajectory in panel (b) which looks to be inscribed within an ellipsoid. The corresponding waves in Fig. 3.25 demonstrate oscillations of irregular amplitudes in the first case, and monotonically increasing-decreasing amplitudes in the second case.

3.4.5 Trajectories originating from the fixed point S_2

The homoclinic trajectories originating from the fixed point S_2 can be divided into two groups.

The first set of solutions exists for $c \in (1.494014, 1.495507)$, and 6 examples of such trajectories are shown in Fig. 3.26. Note the narrow nature of the interval in which these six solutions exist, and hence the accuracy required to specify them. It is seen that the trajectories are affected by the attractive and repelling properties of the all three fixed points. In all cases, the trajectories leave the fixed point S_2 along the 1D unstable manifold and pass large loops around S_0, as in panel (c). Additional smaller loops around

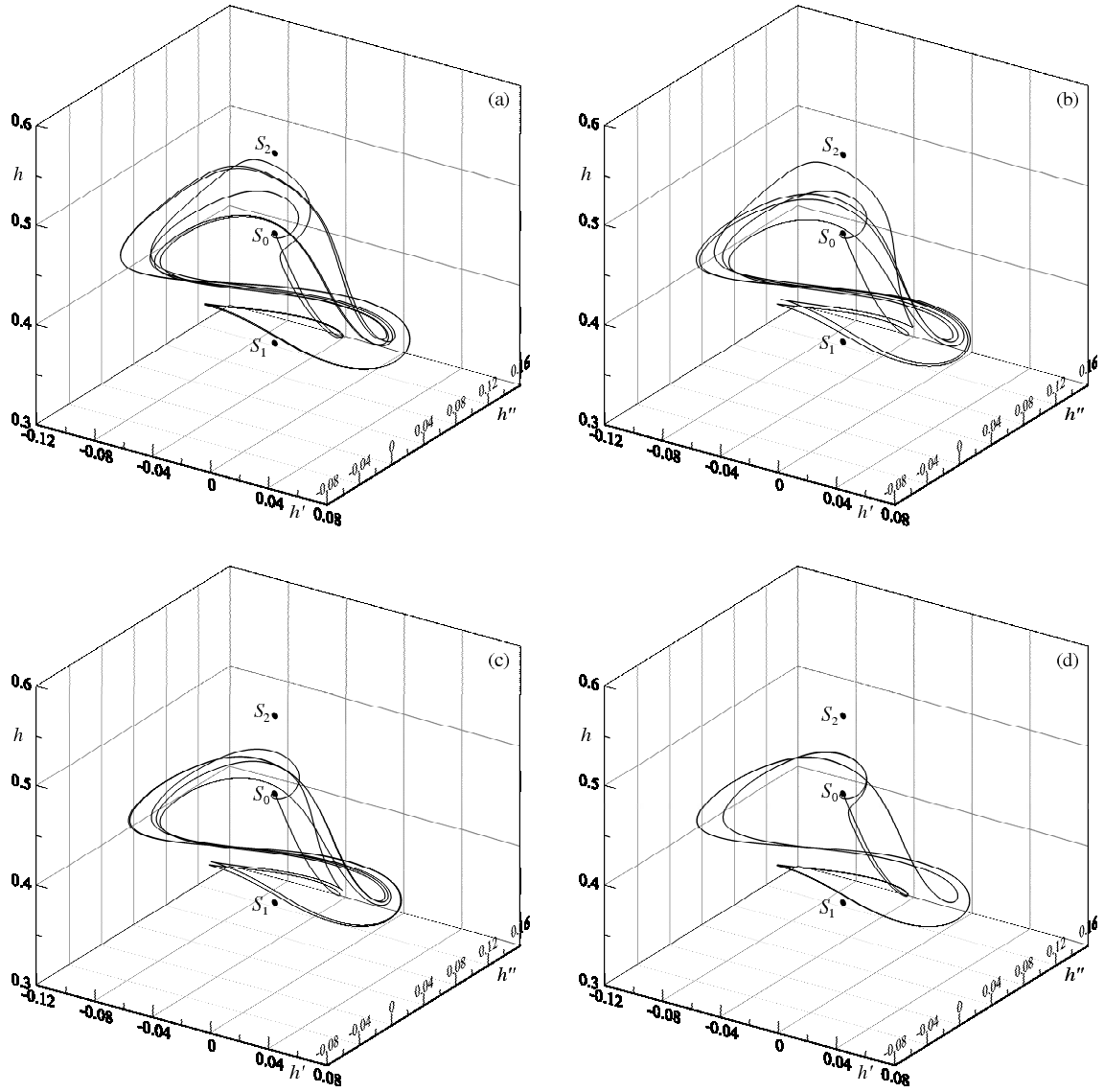

Figure 3.22: Homoclinic trajectories for the fixed point S_0: (a) $c = 1.497830$, (b) $c = 1.498447$, (c) $c = 1.498492$, (b) $c = 1.498508$.

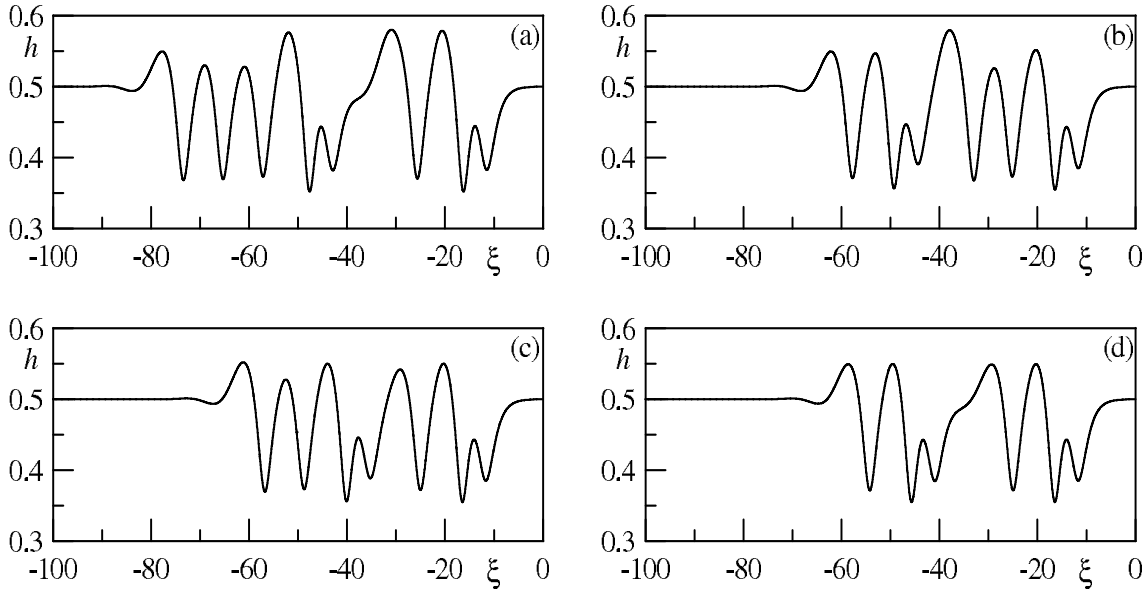

Figure 3.23: Solitary waves for the homoclinic trajectories shown in the panels of Fig. 3.22, respectively.

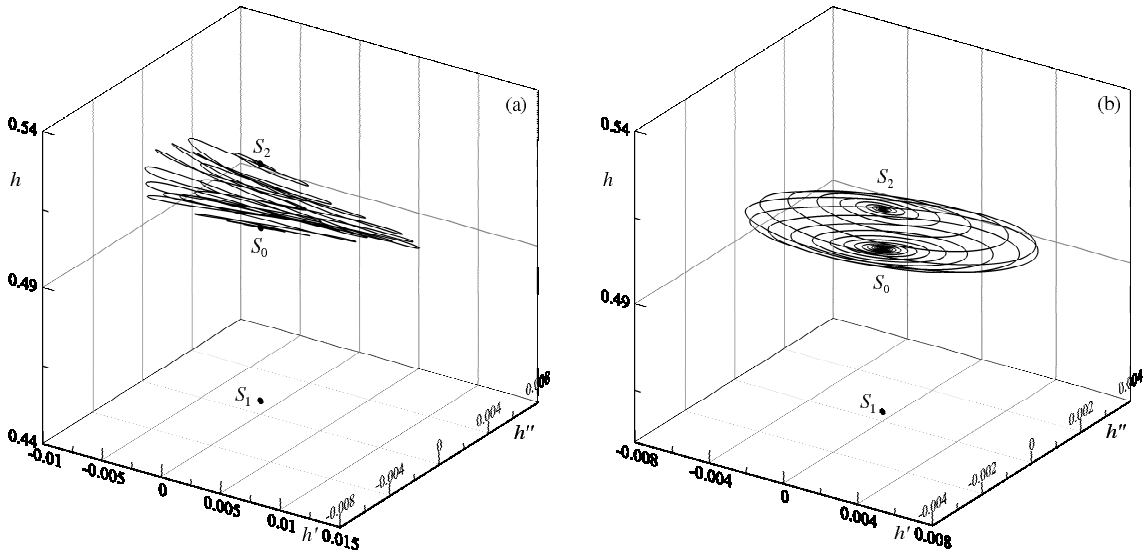

Figure 3.24: Heteroclinic trajectories from the fixed point S_0 to the fixed point S_2: (a) $c = 1.515607$, (b) $c = 1.516961$.

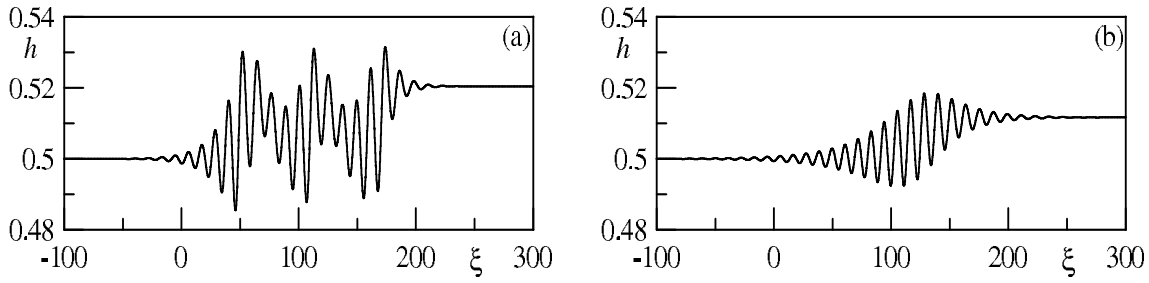

Figure 3.25: Transitional waves for the heteroclinic trajectories shown shown in the panels of Fig. 3.24, respectively.

S_1 are displayed, before the trajectories all return back to S_2 along the stable focus on the surface containing the point S_2. The wave shapes corresponding to these solutions, presented in Fig. 3.27, contain both large and small oscillations. The small oscillations in panel (c) correspond to the loops around the point S_1, where as the large oscillations seen in all panels is a consequence of the trajectory's attempt to return to the point S_2, but falling short of the stable region of this point.

The second group of solutions have trajectories and wave shapes comparable to the slow solitary waves found in the case of the falling film. Velocities of all solutions belong to the interval $c \in (1.512125, c_0)$ and the number of solutions in this range is believed to be infinite. Six examples of phase trajectories corresponding to solutions with velocity c from this interval, are given in Fig. 3.28. It is seen that all trajectories are restricted to the region between S_0 and S_2: the trajectories leave the fixed point S_2 along the 1D unstable manifold, approach the point S_0 and then return to S_2 along spiral curves of different amplitudes. The waves corresponding to these solutions are shown in Fig. 3.29.

The wave forms seen here are reminiscent of the slow solitary waves found in falling films, but the exponential and oscillating segments of the trajectories are inversely oriented.

As an example of how an infinite number of solutions may be found, four examples of solutions from the sub-interval $c \in (1.515076, 1.515128)$ are shown in Fig. 3.30.

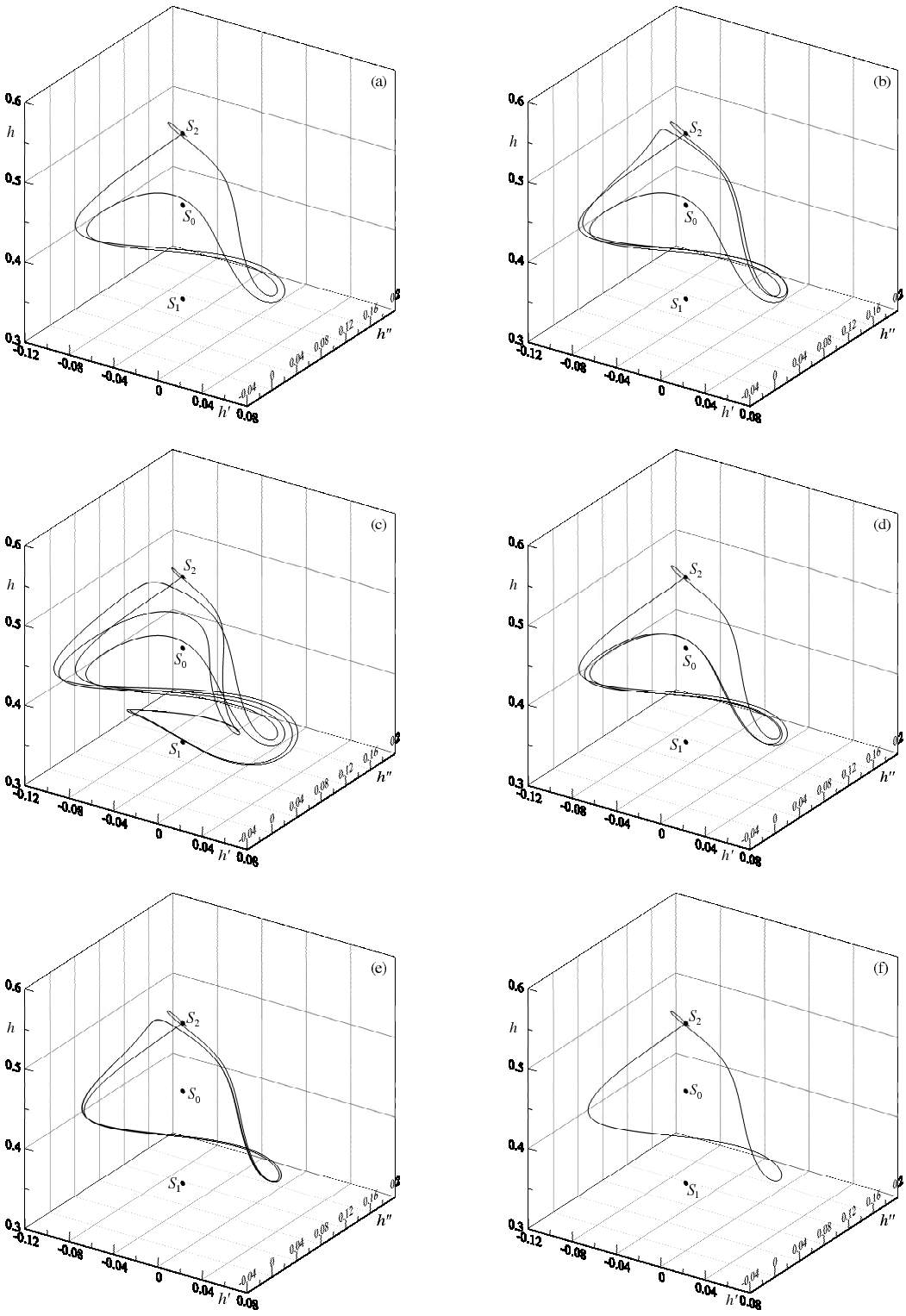

Figure 3.26: Homoclinic trajectories for the fixed point S_2: (a) $c = 1.494014$, (b) $c = 1.494019$, (c) $c = 1.494026$, (d) $c = 1.494092$, (e) $c = 1.495395$, (f) $c = 1.495507$.

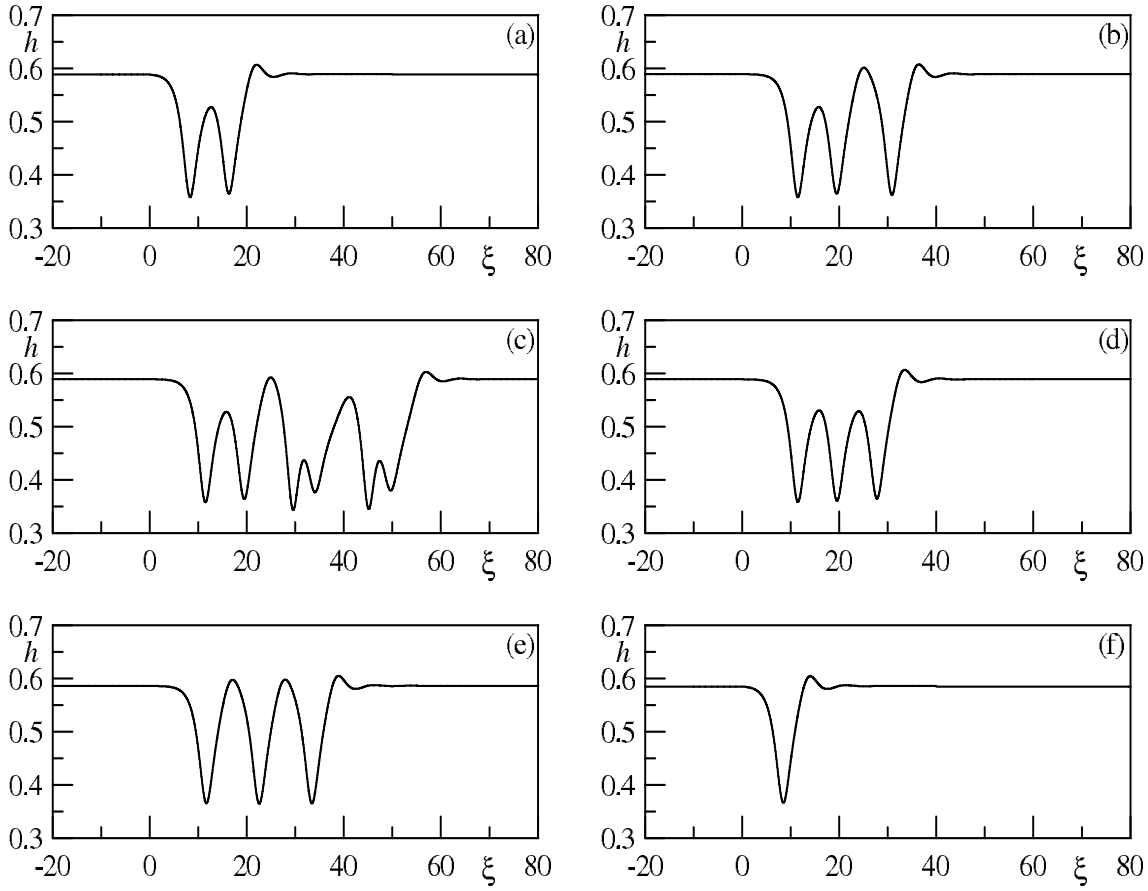

Figure 3.27: Solitary waves for the homoclinic trajectories shown in the panels of Fig. 3.26, respectively.

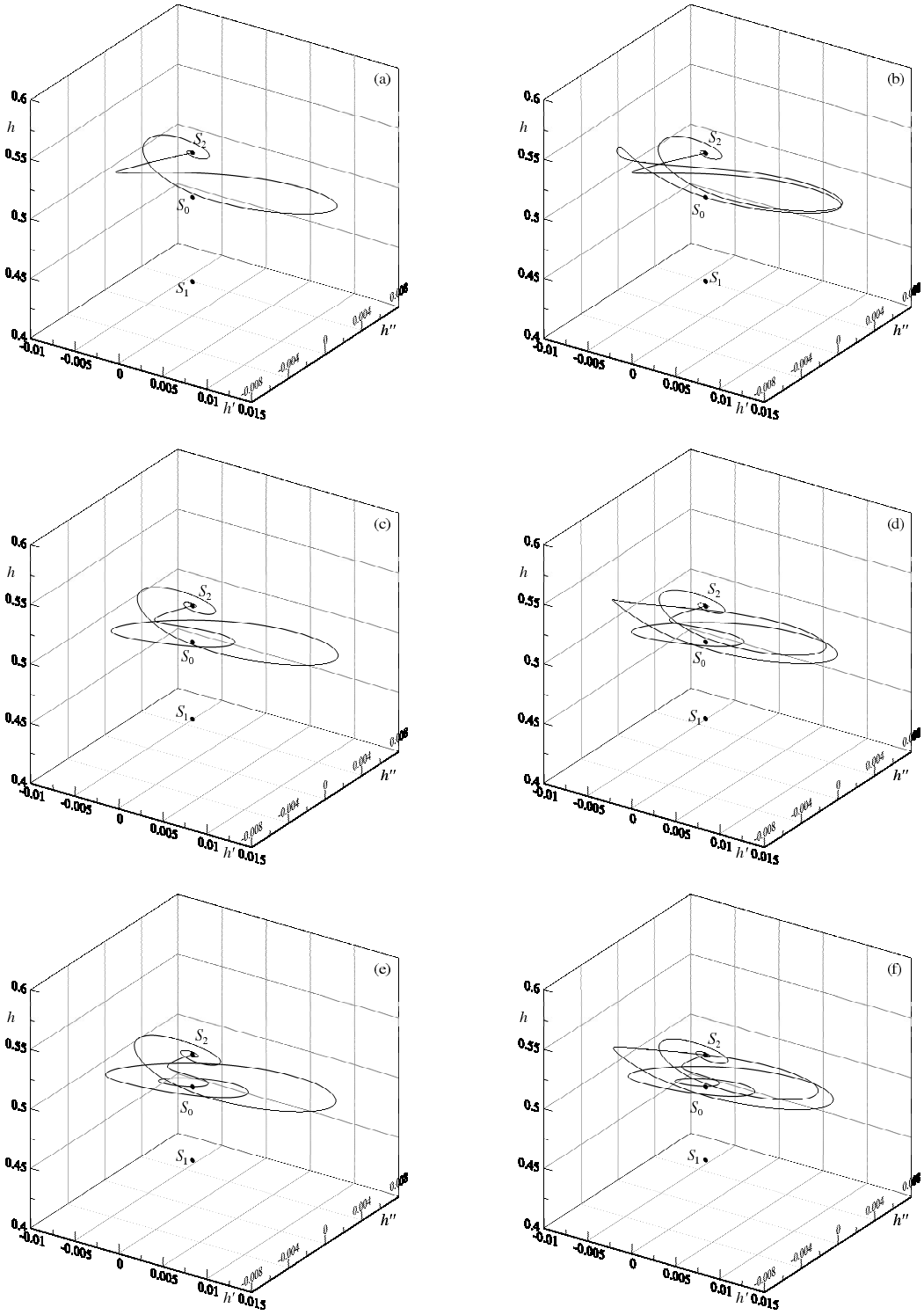

Figure 3.28: Homoclinic trajectories for the fixed point S_2: (a) $c = 1.512125$, (b) $c = 1.512231$, (c) $c = 1.513689$, (d) $c = 1.513775$, (e) $c = 1.514379$, (f) $c = 1.514448$.

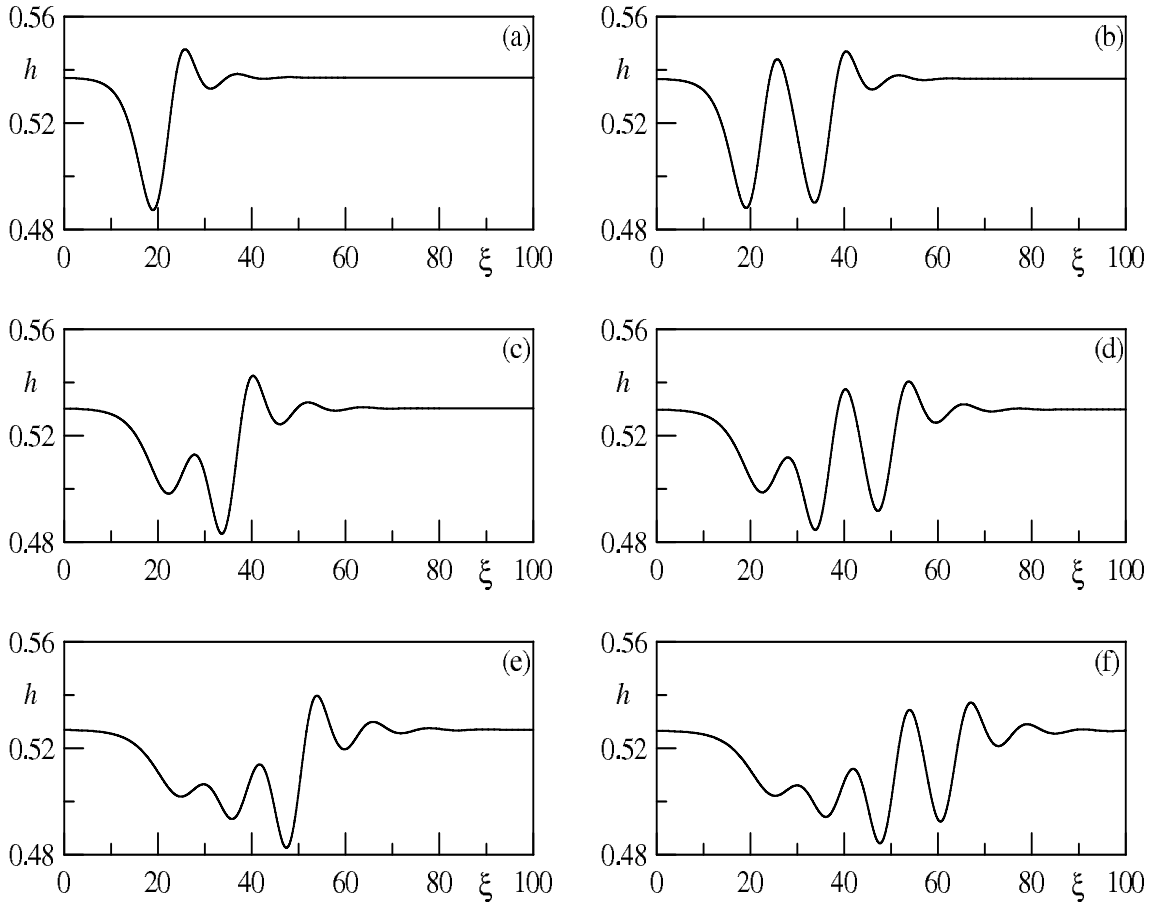

Figure 3.29: Solitary waves for the homoclinic trajectories shown in the panels of Fig. 3.28, respectively.

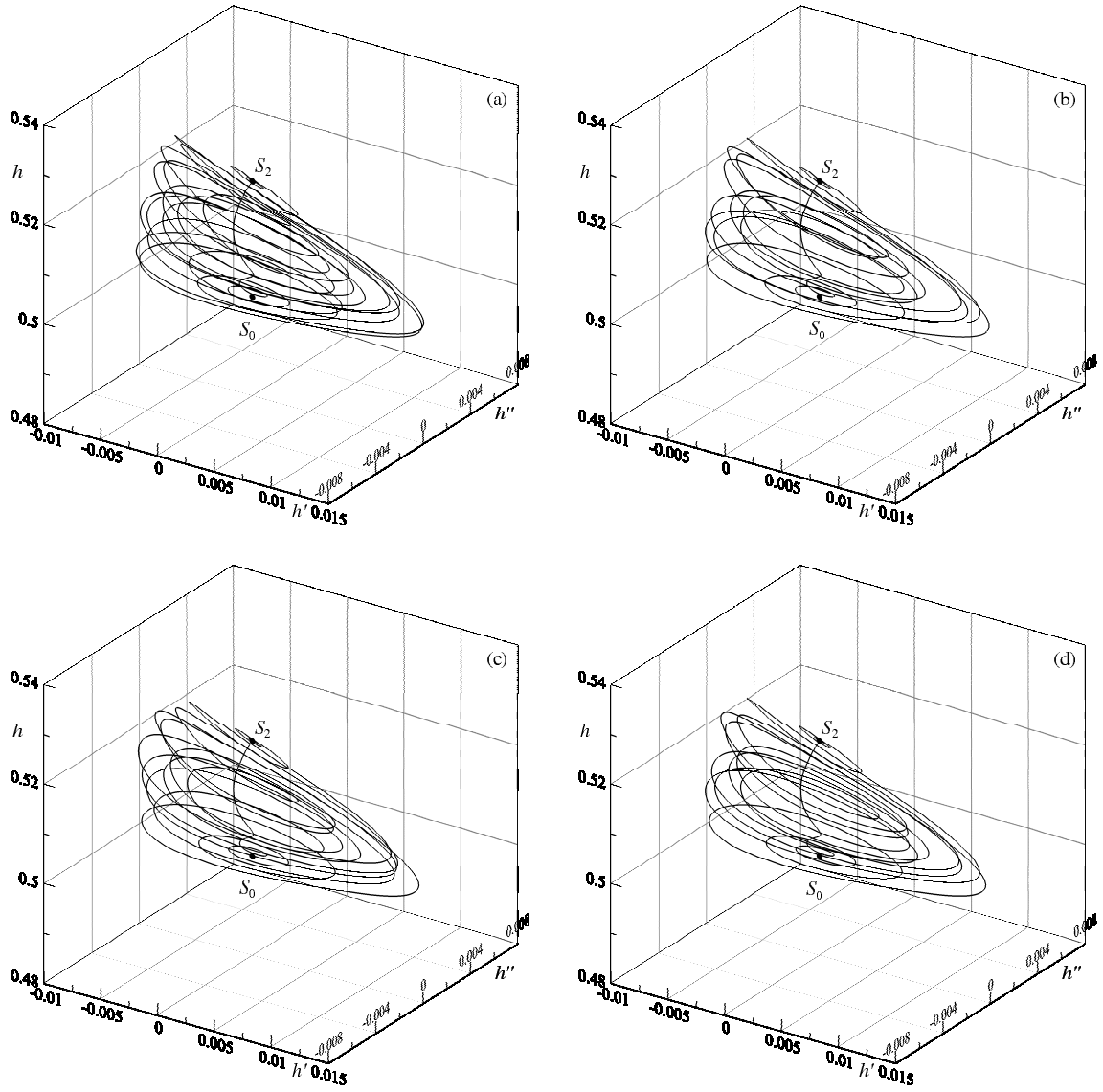

Figure 3.30: Homoclinic trajectories for the fixed point S_2: (a) $c = 1.515093$, (b) $c = 1.515094$, (c) $c = 1.515101$, (d) $c = 1.515103$.

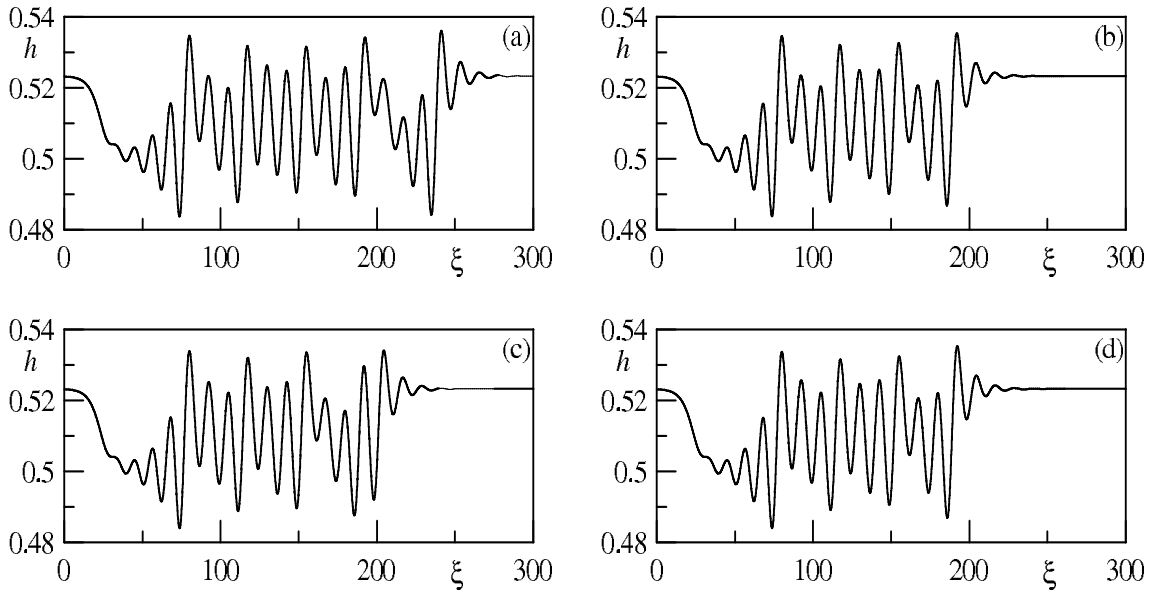

Figure 3.31: Solitary waves for the homoclinic trajectories shown in the panels of Fig. 3.30, respectively.

In all cases there are transitions from S_2 to S_1 along one-dimensional manifolds, and paths returning to S_2 along complex spiral trajectories. The wave shapes shown in Fig. 3.31 have very complicated forms. Note that the wave shapes in panels (b) and (d) are very similar but differ in the interval $\xi \in (80, 120)$.

The trajectory shown in Fig. 3.26(c), which passes near to the point S_1, hints at the existence of heteroclinic trajectories from S_2 to S_1. Examples of such trajectories have been found, and are given in Fig. 3.32.

Since $\beta_{r,l} < 0$ and $\beta_{r,r} < 0$ for the cases shown in panels (a)-(c), in accordance with Fig. 3.14, such trajectories are solutions of ill-posed problems. At values of c in the small neighbourhood of c_0, where $\beta_{r,l} > 0$ and $\beta_{r,r} < 0$, the problem is well-posed and an example of such a trajectory is given in panel (d) (the point S_0 is not shown in this panel). In the physical space Fig. 3.33, the solutions are transitional waves with varying numbers of large humps and preceding ripples in the cases (a)-(c), and a purely oscillating transitional wave in case (d).

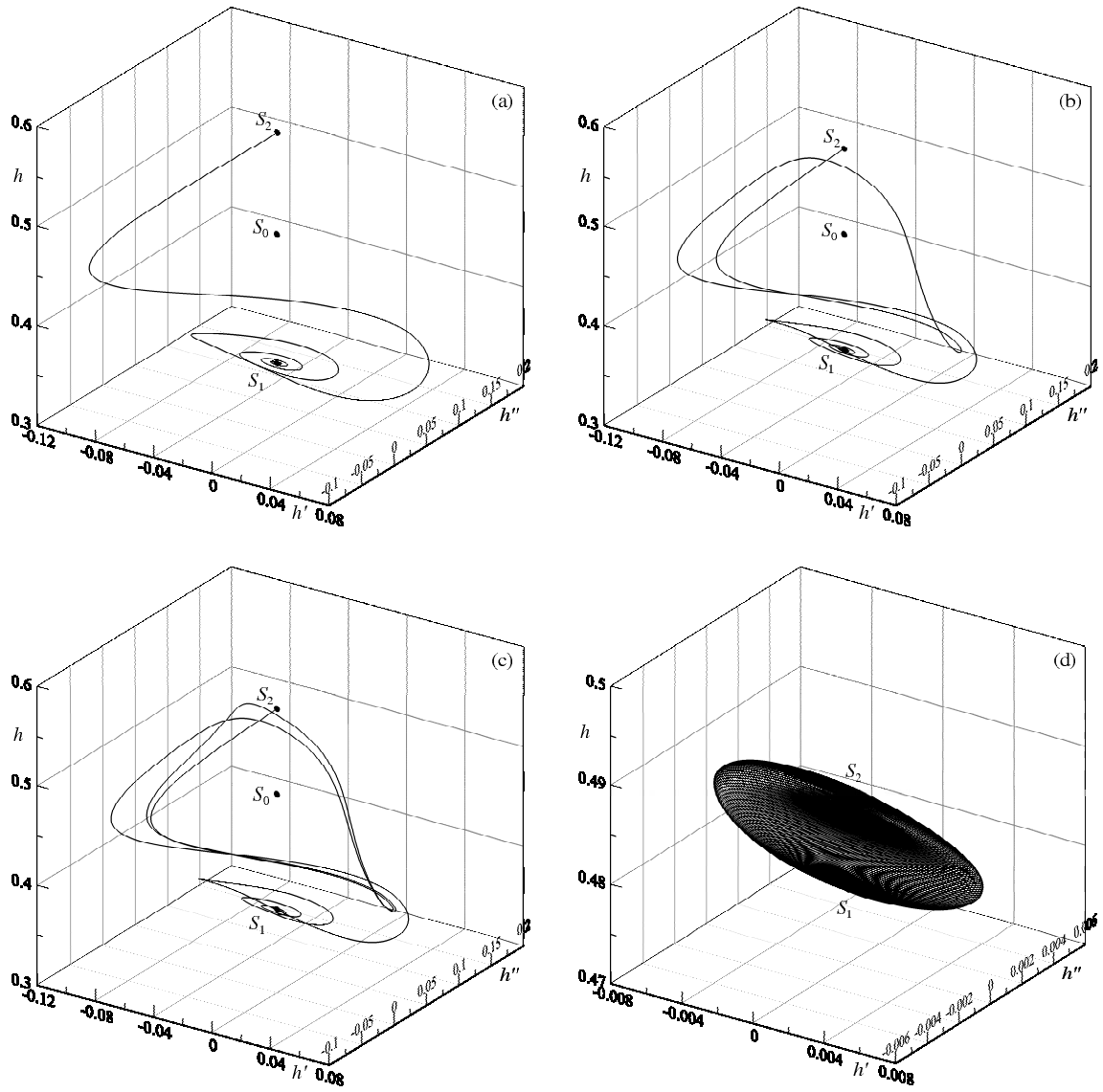

Figure 3.32: Heteroclinic trajectories from the fixed point S_2 to the fixed point S_1: (a) $c = 1.487872$, (b) $c = 1.495194$, (c) $c = 1.495391$, (c) $c = 1.51895$.

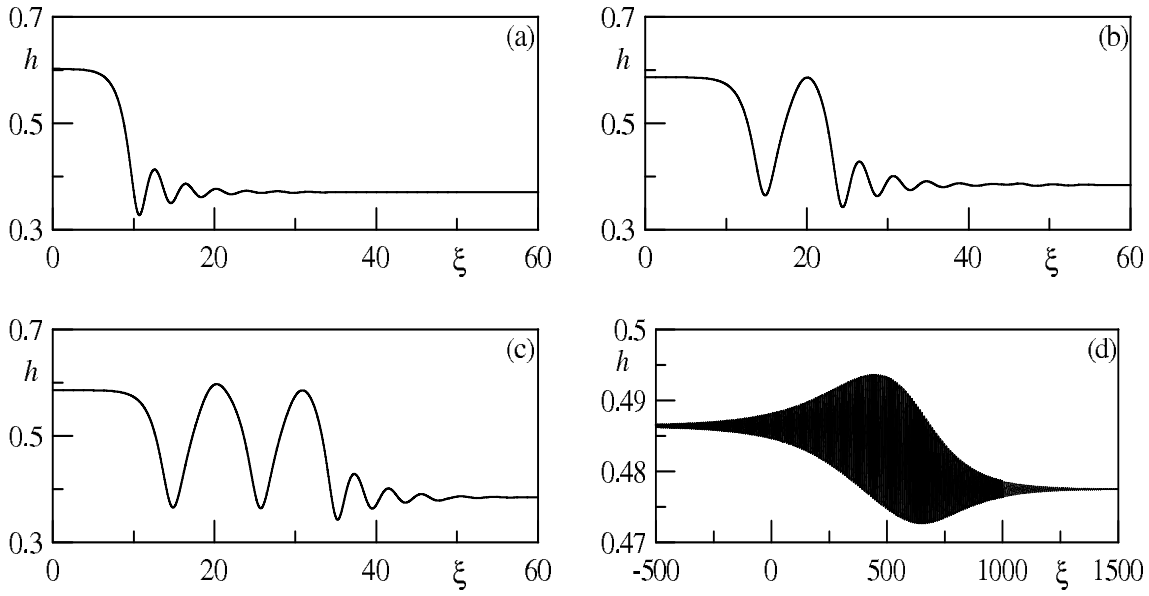

Figure 3.33: Transitional waves for the heteroclinic trajectories shown in the panels of Fig. 3.32, respectively.

Heteroclinic trajectories from the fixed point S_2 to the fixed point S_0 are solutions of the ill-posed problem since $\beta_{r,l} < 0$ and $\beta_{r,r} > 0$ in this case. In fact, such trajectories correspond to the intersection of two one-dimensional manifolds: the unstable manifold of S_2 and the stable manifold of S_0. An example of such a trajectory is given in Fig. 3.34 (the point S_1 is not shown in this panel).

In the physical plane, the wave shape (Fig. 3.35) consists of two exponential parts at $\xi \to -\infty$ and $\xi \to \infty$, connected by a nonlinear part.

3.4.6 Trajectories originating from the fixed point S_1

Heteroclinic trajectories from the fixed point S_1 to the fixed point S_2 are ill-posed in all cases. Two examples of such solutions are given in Fig. 3.36.

The trajectory in panel (a), computed in the case $\beta_{r,l} < 0$ and $\beta_{r,r} < 0$, leaves the fixed point S_1 along the unstable 1D manifold and passes within the neighbourhood of the fixed point S_0, before arriving at the point S_2, a focus on the stable 2D manifold.

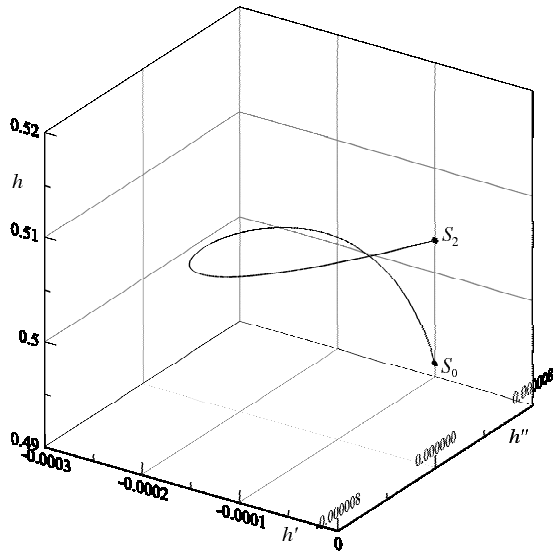

Figure 3.34: Heteroclinic trajectory from the fixed point S_2 to the fixed point S_0 at $c = 1.516956$.

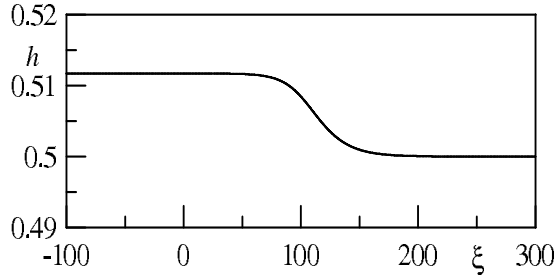

Figure 3.35: Transitional wave for the heteroclinic trajectory shown in the panels of Fig. 3.34, respectively.

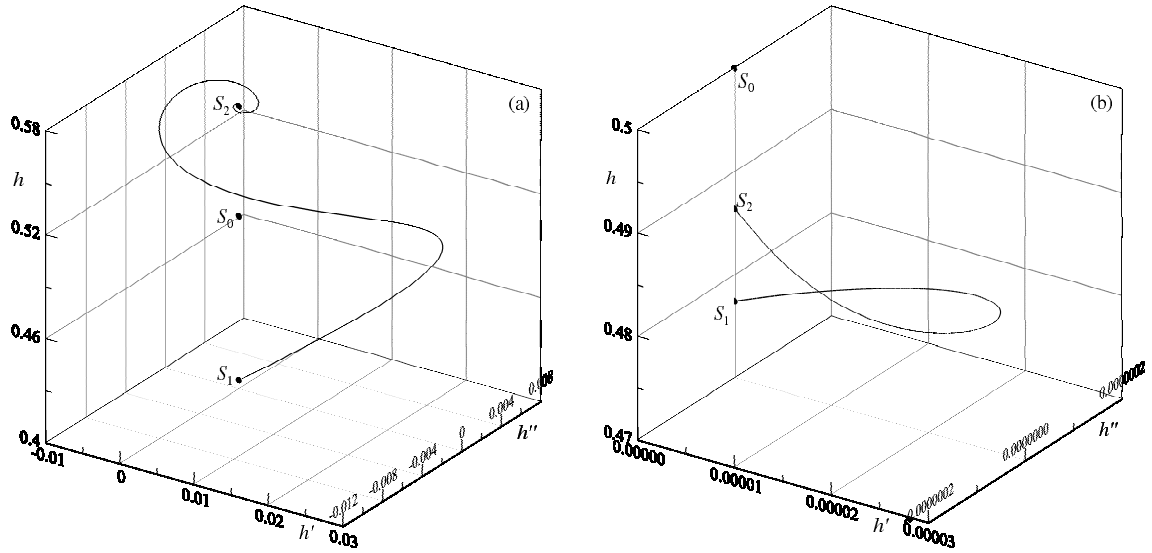

Figure 3.36: Heteroclinic trajectory from the fixed point S_1 to the fixed point S_2: (a) $c = 1.504376$, (b) $c = 1.51895$.

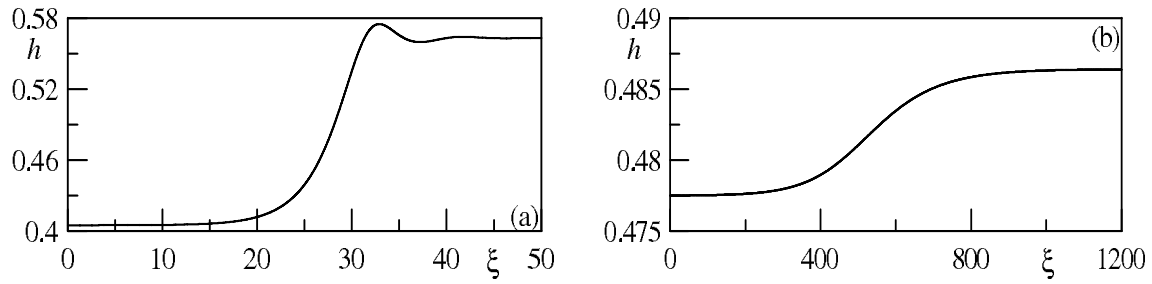

Figure 3.37: Transitional wave for the heteroclinic trajectory shown in the panels of Fig. 3.36, respectively.

In the physical plane, the exponential behaviour for small values of ξ lead to oscillations tending to $h = h_2$ (Fig. 3.37).

The trajectory in Fig. 3.36(b) exists at a velocity value which is very close to the velocity corresponding to Fig. 3.32(d). In this case $\beta_{r,l} < 0$ and $\beta_{r,r} > 0$ which corresponds to the case of an ill-posed problem with two exponential asymptotics, matched by the non-linear part of the trajectory. This is illustrated in the physical plane Fig. 3.37(b).

Two trajectories from S_1 to S_0 are presented in Fig. 3.38. In both cases $\beta_{r,l} < 0$ and $\beta_{r,r} < 0$, and so these trajectories are also solutions of the ill-posed problem. In addition

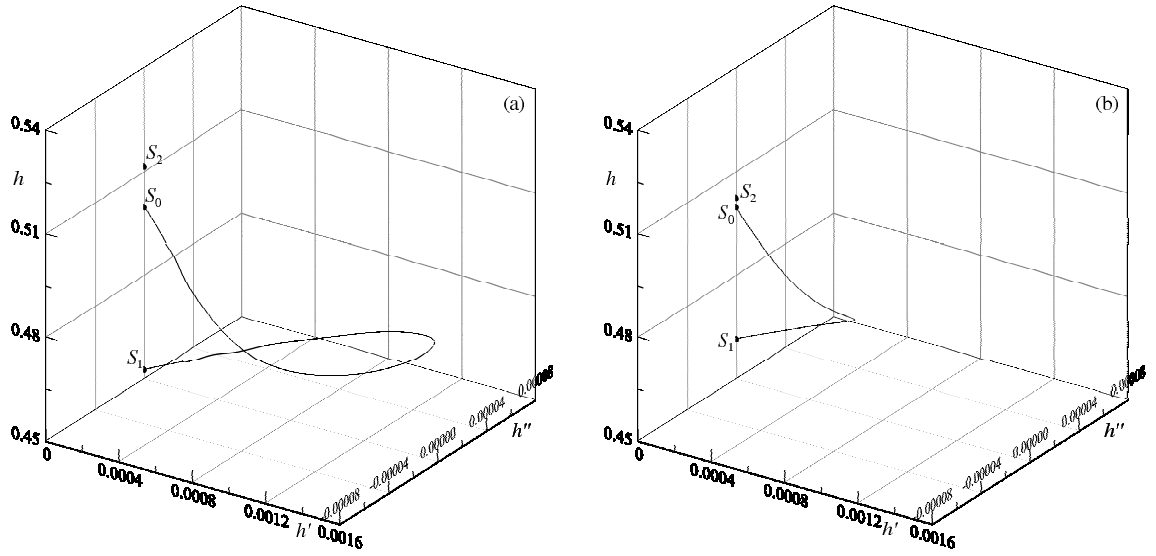

Figure 3.38: Heteroclinic trajectory from the fixed point S_1 to the fixed point S_0: (a) $c = 1.516960$, (b) $c = 1.518006$.

to similar cases shown above, the wave shapes include exponential asymptotics.

Homoclinic trajectories for the fixed point S_1 have not been found. In all computed cases the trajectories leaving S_0 reached a domain boundary, $w_1 = 1$ or $w_1 = 0$, before returning to the neighbourhood of this fixed point. Nevertheless, heteroclinic trajectories may potentially exist in these cases, for instance, when the velocity c is close to the heteroclinic trajectories from S_1 to S_0 or S_2.

It is also worth noting that all solutions found in the three subsections above, have wave velocities which fall within a relatively narrow interval. All regimes shown here attain a non-dimensional velocity c between 1.48 and 1.52, which means that all waves travel roughly 50% faster than the liquids themselves. Despite the confined range of velocities, the waves regimes vary considerably. Examples have been found to have any number of oscillations from one to several hundred, and the amplitudes of these oscillations vary considerably too. The largest wave amplitudes were found to be roughly 20% of the width of the channel, and the smallest are but infinitesimal ripples.

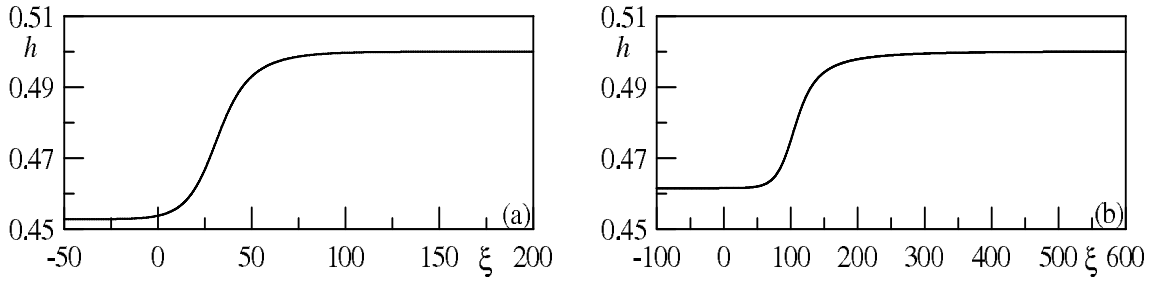

Figure 3.39: Transitional wave for the heteroclinic trajectory shown in the panels of Fig. 3.38, respectively.

Chapter 4

Solitary and Transitional Waves in Pressure-Driven Two-Layer Microchannel Flows

4.1 Steady travelling waves

A wave travelling steadily with velocity c, is a solution of the evolution system (2.51) for the pressure-driven case. This type of solution has the form $h(\xi)$, $q^{(1)}(\xi)$ and $q^{(2)}(\xi)$, where ξ is given by the same change of co-ordinates (3.1), as in the gravity-driven case. Substituting this solution into (2.51) leads to two ordinary differential equations. The first equation can be integrated so that the following system, for the functions $h(\xi)$, $q^{(1)}(\xi)$ and $q^{(2)}(\xi)$, is found

$$\begin{aligned} &-c^2\left(\frac{1}{h}+\frac{\rho_0}{1-h}\right)\frac{dh}{d\xi}+\frac{1}{h}\frac{d}{d\xi}\left(\frac{a_{11}^2}{3}h^3+\frac{a_{11}a_{12}}{2}h^4+\frac{a_{12}^2}{5}h^5\right)\\ &\quad+\frac{\rho_0}{1-h}\frac{d}{d\xi}\left(\frac{a_{21}^2}{3}(h-1)^3+\frac{a_{21}a_{22}}{2}(h-1)^4+\frac{a_{22}^2}{5}(h-1)^5\right)\\ &\quad=\frac{1}{5\delta_p\beta}\frac{d^3h}{d\xi^3}+\frac{2}{5\delta_p\beta}\left(a_{12}-\rho_0\nu_0a_{22}\right), \qquad (4.1)\\ &q^{(1)}=ch+q_\infty^{(1)},\quad q^{(1)}+q^{(2)}=1, \end{aligned}$$

or,

$$
\begin{aligned}
&-c^2\left(1+\frac{\rho_0 h}{1-h}\right)\frac{dh}{d\xi}+\frac{d}{d\xi}\left(\frac{a_{11}^2}{3}h^3+\frac{a_{11}a_{12}}{2}h^4+\frac{a_{12}^2}{5}h^5\right)\\
&\quad+\frac{\rho_0 h}{1-h}\frac{d}{d\xi}\left(\frac{a_{21}^2}{3}(h-1)^3+\frac{a_{21}a_{22}}{2}(h-1)^4+\frac{a_{22}^2}{5}(h-1)^5\right)\\
&\quad=\frac{1}{5\delta_p\beta}\left[h\frac{d^3h}{d\xi^3}+2\left(a_{12}-\rho_0\nu_0 a_{22}\right)h\right]\\
&q^{(1)}=ch+q_\infty^{(1)},\quad q^{(1)}+q^{(2)}=1,
\end{aligned}
$$

where $q_\infty^{(1)}$ is the integration constant to be found. For each solution of (4.1) the pressure distribution along the wave is calculated from the equation

$$
\begin{aligned}
&\left(h+\frac{1-h}{\rho_0}\right)\frac{dp^{(2)}}{d\xi}=\frac{1}{5\delta_p\beta}h\frac{d^3h}{d\xi^3}+\frac{2}{5\delta_p\beta}\left[a_{12}h-\nu_0 a_{22}(h-1)\right]\\
&\quad-\frac{d}{d\xi}\left(\frac{a_{11}^2}{3}h^3+\frac{a_{11}a_{12}}{2}h^4+\frac{a_{12}^2}{5}h^5\right)\\
&\quad+\frac{d}{d\xi}\left(\frac{a_{21}^2}{3}(h-1)^3+\frac{a_{21}a_{22}}{2}(h-1)^4+\frac{a_{22}^2}{5}(h-1)^5\right),
\end{aligned}
\tag{4.2}
$$

following from (2.52).

4.2 Dynamical system

It is seen that, similar to the gravity-driven case, the equation (4.2) can be re-formulated in terms of a dynamical system. Introducing the following variables

$$
w_1=h,\quad w_2=\frac{dh}{d\xi},\quad w_3=\frac{d^2h}{d\xi^2},
$$

equation (4.2) may be re-written in the form

$$
\frac{dw_1}{d\xi}=w_2,\quad \frac{dw_2}{d\xi}=w_3,\quad \frac{dw_3}{d\xi}=W,
\tag{4.3}
$$

$$W = -2\left(a_{12} - \rho_0\nu_0 a_{22}\right) + \frac{5\delta b}{w_1}\left[\frac{dW_a}{d\xi} + \frac{\rho_0 w_1}{1-w_1}\frac{dW_b}{d\xi} - c^2\left(1 + \frac{\rho_0 w_1}{1-w_1}\right)w_2\right]$$

where,

$$\begin{aligned}
W_a &= \frac{a_{11}^2}{3}w_1^3 + \frac{a_{11}a_{12}}{2}w_1^4 + \frac{a_{12}^2}{5}w_1^5, \\
W_b &= \frac{a_{21}^2}{3}\left(w_1 - 1\right)^3 + \frac{a_{21}a_{22}}{2}\left(w_1 - 1\right)^4 + \frac{a_{22}^2}{5}\left(w_1 - 1\right)^5.
\end{aligned}$$

Using the chain rule, the derivatives which appear in the function W of (4.3) are calculated as

$$\frac{dW_a}{d\xi} = \left(\frac{\partial W_a}{\partial h} + c\frac{\partial W_a}{\partial q^{(1)}}\right)w_2, \quad \frac{dW_b}{d\xi} = \left(\frac{\partial W_b}{\partial h} + c\frac{\partial W_b}{\partial q^{(1)}}\right)w_2,$$

where,

$$\begin{aligned}
\frac{\partial W_a}{\partial h} &= \frac{2a_{11}}{3}\frac{\partial a_{11}}{\partial h}w_1^3 + a_{11}^2 w_1^2 + \frac{1}{2}\left(a_{12}\frac{\partial a_{11}}{\partial h} + a_{11}\frac{\partial a_{12}}{\partial h}\right)w_1^4 + 2a_{11}a_{12}w_1^3 \\
&\quad + \frac{2a_{12}}{5}\frac{\partial a_{12}}{\partial h}w_1^5 + a_{12}^2 w_1^4, \\
\frac{\partial W_a}{\partial q^{(1)}} &= \frac{2a_{11}}{3}\frac{\partial a_{11}}{\partial q^{(1)}}w_1^3 + \frac{1}{2}\left(a_{12}\frac{\partial a_{11}}{\partial q^{(1)}} + a_{11}\frac{\partial a_{12}}{\partial q^{(1)}}\right)w_1^4 + \frac{2a_{12}}{5}\frac{\partial a_{12}}{\partial q^{(1)}}w_1^5, \\
\frac{\partial W_b}{\partial h} &= \frac{2a_{21}}{3}\frac{\partial a_{21}}{\partial h}\left(w_1 - 1\right)^3 + a_{21}^2\left(w_1 - 1\right)^2 + \frac{1}{2}\left(a_{22}\frac{\partial a_{21}}{\partial h} + a_{21}\frac{\partial a_{22}}{\partial h}\right)\left(w_1 - 1\right)^4 \\
&\quad + 2a_{21}a_{22}\left(w_1 - 1\right)^3 + \frac{2a_{22}}{5}\frac{\partial a_{22}}{\partial h}\left(w_1 - 1\right)^5 + a_{22}^2\left(w_1 - 1\right)^4, \\
\frac{\partial W_b}{\partial q^{(1)}} &= \frac{2a_{21}}{3}\frac{\partial a_{21}}{\partial q^{(1)}}\left(w_1 - 1\right)^3 + \frac{1}{2}\left(a_{22}\frac{\partial a_{21}}{\partial q^{(1)}} + a_{21}\frac{\partial a_{22}}{\partial q^{(1)}}\right)\left(w_1 - 1\right)^4 \\
&\quad + \frac{2a_{22}}{5}\frac{\partial a_{22}}{\partial q^{(1)}}\left(w_1 - 1\right)^5,
\end{aligned}$$

which include the following terms depending on $w_1 = h$,

$$\frac{\partial a_{11}}{\partial h}, \quad \frac{\partial a_{11}}{\partial q^{(1)}}, \quad \frac{\partial a_{12}}{\partial h}, \quad \frac{\partial a_{12}}{\partial q^{(1)}}, \quad \frac{\partial a_{21}}{\partial h}, \quad \frac{\partial a_{21}}{\partial q^{(1)}}, \quad \frac{\partial a_{22}}{\partial h}, \quad \frac{\partial a_{22}}{\partial q^{(1)}}.$$

The partial derivatives are given in Appendix (A.2), for the sake of brevity.

4.3 Homoclinic and heteroclinic trajectories

The steady flow solution (2.54) is already known to be a solution of the system (4.1) and hence allows the integration constant, $q_\infty^{(1)} = Q^{(1)} - cH$, to be found. Therefore, by replacing this back into the system (4.1) and considering an arbitrary fixed point, where the thickness of the first layer does not depend on ξ, it is seen that any fixed point satisfies the reduced system

$$\begin{aligned} &a_{12}\left(\rho_0\nu_0, h_f, q_f^{(1)}, q_f^{(2)}\right) - \rho_0\nu_0 a_{22}\left(\rho_0\nu_0, h_f, q_f^{(1)}, q_f^{(2)}\right) = 0, \\ &q_f^{(1)} = c\left(h_f - H\right) + Q_0^{(1)}, \quad q_f^{(1)} + q_f^{(2)} = 1, \end{aligned} \tag{4.4}$$

for the first layer thickness h_f, flow rates $q_f^{(1)}$ and $q_f^{(2)}$, and velocity c, where subscript f denotes variables corresponding to the fixed point. The system of three equations (4.4) contains four variables: h_f, $q_f^{(1)}$, $q_f^{(2)}$, and c. Hence it is seen that there must be at least one one-parametric family of solutions.

For each solution $\left(h_f, q_f^{(1)}, q_f^{(2)}, c\right)$, it follows from (4.2) that the pressure gradient in the second layer satisfies the equation

$$\delta_p \frac{dp_f^{(2)}}{d\xi} = \frac{2}{5\beta}\left[a_{12}h_f - \nu_0 a_{22}\left(h_f - 1\right)\right]\left(h_f + \frac{1-h_f}{\rho_0}\right)^{-1}.$$

There are two limit cases corresponding to small thicknesses of the first layer, or the second layer, and are examined by applying the Taylor series expansion firstly for h_f and then for $(h_f - 1)$, to consider cases where $h_f \to 0$ and $h_f \to 1$. If $h_f \to 0$ then

$$q_f^{(1)} = 3\rho_0\nu_0 h_f^2\left[1 + \left(\frac{10}{3} - 4\rho_0\nu_0\right)h_f + \left(7 - 23\rho_0\nu_0 + 16\rho_0^2\nu_0^2\right)h_f^2 + O\left(h_f^3\right)\right],$$

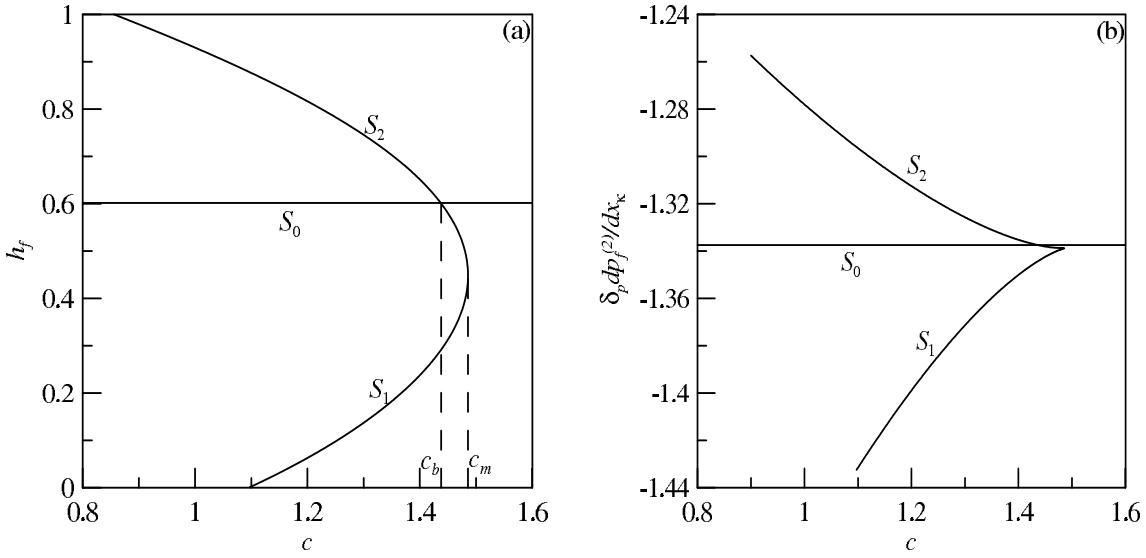

Figure 4.1: Dependencies of the thickness of the first layer (a) and the pressure gradient in the second layer (b) on the wave velocity at the fixed points in case C of Table 2.1.

$$\delta_p \frac{dp_f^{(2)}}{d\xi} = -\frac{12\rho_0\nu_0}{5\beta}\left[1 + 3\left(1 - \rho_0\nu_0\right)h_f + O\left(h_f^2\right)\right],$$

that is, the first layer flow rate tending to zero and the pressure gradient in the second layer tending to the constant. If $h_f \to 1$ then

$$q_f^{(1)} = 1 - \frac{6}{\rho_0\nu_0}\left(h_f - 1\right) - \frac{18 + 3\rho_0\nu_0}{\rho_0^2\nu_0^2}\left(h_f - 1\right)^2 + O\left(\left(h_f - 1\right)^3\right),$$
$$\delta_p \frac{dp_f^{(2)}}{d\xi} = -\frac{18}{5\beta\rho_0\left(h_f - 1\right)}\left[1 + \frac{h_f - 1}{\rho_0} + O\left(\left(h_f - 1\right)^2\right)\right],$$

that is, the first layer flow rate tending to 1 and the pressure gradient in the second layer tending to negative infinity.

For a given value $\rho_0\nu_0$, solutions of equations (4.4) are parametrised by the wave velocity c. Fig. 4.1 shows three families of fixed points for case C (Table 2.1). The family $S_0 = (h_0, 0, 0)$, where $h_0 = H$, corresponds to the waveless flow given by (2.54) and (2.55), and its fixed points do not depend on the velocity c. The fixed points of families S_1 and

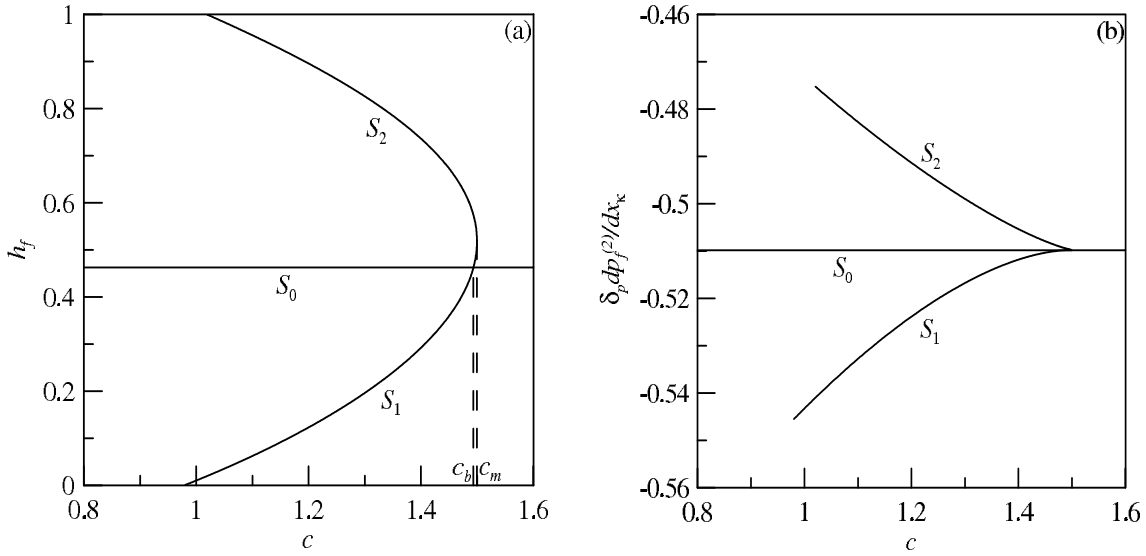

Figure 4.2: Dependencies of the thickness of the first layer (a) and the pressure gradient in the second layer (b) on the wave velocity at the fixed points in case A of Table 2.1.

S_2, which vary with the parameter c, belong to the smooth curve in Fig. 4.1(a) and the cusp curve in panel Fig. 4.1(b). The families S_1 and S_2 meet each other at the bifurcation point which has the maximum velocity $c = c_m$, noted in panel Fig. 4.1(a). On the other hand, the families S_0 and S_2 also bifurcate at the velocity $c = c_b < c_m$ shown in the same panel.

A similar bifurcation scheme appears for case A (Table 2.1), but the bifurcation point with velocity c_b belongs to the families S_0 and S_1 (Fig. 4.2) and is very close to the maximum velocity c_m.

To investigate solutions in the neighbourhood of a fixed point $\left(h_f, q_f^{(1)}, q_f^{(2)}, c\right)$ belonging to one of the families S_0, S_1 or S_2, a solution in the form $h = h_f + \widehat{h}$, $q^{(1)} = q_f^{(1)} + \widehat{q}^{(1)}$ and $q^{(2)} = q_f^{(2)} + \widehat{q}^{(2)}$ where $q_f^{(1)} = ch_f + q_\infty^{(1)}$, and $\widehat{h}$, $\widehat{q}^{(1)}$ and $\widehat{q}^{(2)}$ are small perturbations, is sought. Substituting such a solution into (4.1), linearising with regard to small perturbations and eliminating the perturbations of the flow rates, leads to the linear equation

for the first layer perturbation

$$\frac{d^3\widehat{h}}{d\xi^3} + k_1\frac{d\widehat{h}}{d\xi} + k_0\widehat{h} = 0, \tag{4.5}$$

where expressions of the coefficients k_0 and k_1 are given in Appendix (A.3) for the sake of brevity. Hence, the characteristic equation is given by

$$\lambda^3 + k_1\lambda + k_0 = 0,$$

which has the following roots

$$\begin{aligned}
\lambda_1 &= \beta_r + i\beta_i, \\
\lambda_2 &= \beta_r - i\beta_i, \\
\lambda_3 &= -2\beta_r,
\end{aligned}$$

where the sign of the parameter β_r coincides with the sign of k_0. Thus, there are two possible cases of asymptotic behaviour in the neighbourhood of the fixed point $\left(h_f, q_f^{(1)}, q_f^{(2)}, c\right)$:

$$\begin{aligned}
k_0 < 0, \quad \beta_r < 0 \quad &: \quad h = h_f + E_2 e^{-2\beta_r\xi}, \quad \xi \to -\infty, \\
&\qquad h = h_f + E_1 e^{\beta_r\xi}\cos\left(\beta_i\xi - \phi\right), \quad \xi \to +\infty \\
k_0 > 0, \quad \beta_r > 0 \quad &: \quad h = h_f + E_1 e^{\beta_r\xi}\cos\left(\beta_i\xi - \phi\right), \quad \xi \to -\infty \\
&\qquad h = h_f + E_2 e^{-2\beta_r\xi}, \quad \xi \to +\infty.
\end{aligned} \tag{4.6}$$

Considering ξ varying from $-\infty$ to $+\infty$ for the case $\beta_r < 0$, the fixed point is a saddle-focus with unstable one-dimensional manifold and stable two-dimensional manifold. For the case $\beta_r > 0$, the fixed point is a stable one-dimensional manifold and unstable two-dimensional manifold for a saddle-focus point.

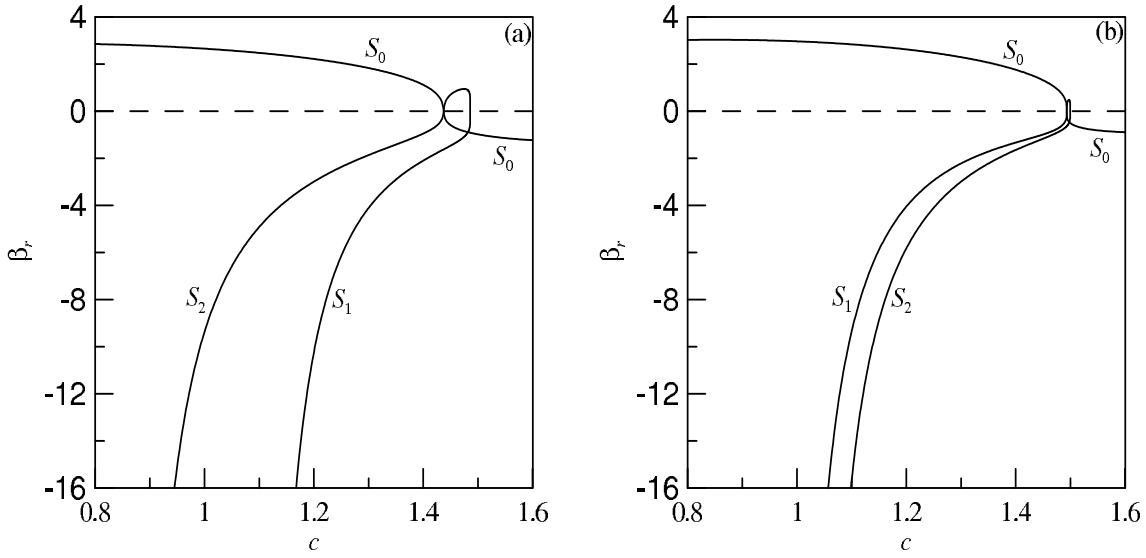

Figure 4.3: The stability parameter β_r in cases C (a) and A (b) of Table 2.1.

Examples of calculations for the stability parameter β_r are shown in Fig. 4.3. In both cases, for the family S_0, the stability parameter $\beta_r > 0$ if $c < c_b$, and $\beta_r < 0$ if $c > c_b$. For the families S_1 and S_2, the stability parameter $\beta_r < 0$ for all values of c outside of the interval (c_b, c_m) where $\beta_r > 0$. This interval belongs to the family S_2 in case C, and family S_1 in case A.

4.4 Results

4.4.1 Similarity parameters

The results for the pressure-driven flow are given for a dyed deionized water and kerosene system. The properties of the two fluids are given in Chapter 2. The relative thickness of the first layer is again considered to belong to the interval $h_0 \in (0, 1)$, and δ to be bounded by the condition $\kappa^2 \ll 1$.

4.4.2 Fixed points

It is seen that the fixed points of the dynamical system (4.3) depend on the sign of β_r, as in the gravity-driven case. This parameter determines the type of behaviour that is exhibited as $\xi \to \pm\infty$. Considering the asymptotics (4.6) it is obvious from the results given below, particularly in the physical space, which side of the solution corresponds to the exponentially oscillating behaviour, and the purely exponential behaviour.

4.4.3 Solitary and transitional waves

Firstly, in this section, solutions having asymptotic behaviour (4.6) in case C of Table 2.1, are demonstrated.

As discussed in detail in the previous chapter, a solitary wave is a steady travelling wave such that $h(\xi) \to h_f$ as $\xi \to \pm\infty$. It is seen that the second equation in (4.1) gives $q_\infty^{(1)} = q_f^{(1)} - ch_f$, and thus the flow rate in the first layer is $q^{(1)} = q_f^{(1)} + c\,(h - h_f)$. To find solitary wave solutions it is necessary to solve the first equation in (4.1) with the asymptotic boundary conditions given in (4.6). In both cases, namely $\beta_r > 0$ and $\beta_r < 0$, the solution depends on four variables which have to be found: c, E_1, E_2 and ϕ. As discussed in Chapter 3, since the problem is invariant with regard to a shift along ξ, this leaves just three values which have to be found from matching two numerical solutions with the initial conditions given in (4.6).

In the phase space (h, h', h''), a solitary wave corresponds to a homoclinic trajectory belonging to the intersection of the unstable (stable) one-dimensional manifold and stable (unstable) two-dimensional manifold of a fixed point $(h_f, 0, 0)$.

Heteroclinic trajectories corresponding to the unstable waveless flow are considered. These solutions correspond to transitional waves in the physical space when $h \to h_{f,l}$ as $\xi \to -\infty$, and $h \to h_{f,r}$ as $\xi \to +\infty$, where $h_{f,l}$ and $h_{f,r}$ are the first layer thicknesses at

different fixed points. Then the second equation in (4.1) can written for both fixed points

$$q_\infty^{(1)} = q_{f,l}^{(1)} - ch_{f,l} = q_{f,r}^{(1)} - ch_{f,r},$$

which gives the wave velocity

$$c = \frac{q_{f,l}^{(1)} - q_{f,r}^{(1)}}{h_{f,l} - h_{f,r}}. \tag{4.7}$$

In order to match two solutions starting from neighbourhoods of both points, continuity of the functions h, h' and h'' must be provided. Since the velocity is given by (4.7), and the problem is invariant with regard to a shift along ξ, these three conditions can only be provided when both solutions are oscillating at $\xi \to -\infty$ and $\xi \to +\infty$, that is, $\beta_r > 0$ for the fixed point $(h_{f,l}, c)$ and $\beta_r < 0$ for the fixed point $(h_{f,r}, c)$. This follows from analysis similar to the cases (3.14) for the gravity-driven case. Certainly, isolated solutions may exist in other cases.

4.4.4 Homoclinic trajectories of the fixed point S_0

Fig. 4.4 demonstrates solitary waves with velocity $c < c_b$. The shapes of these waves are similar to so-called slow waves in falling films [44, 7, 48], as discussed in Chapter 3, if the second layer is considered as the 'film'. All waves are grouped in pairs, where the shapes have one or two large peaks extending into the domain of the second layer. Each pair has the same number of small oscillations in front, and this number grows as the wave velocity approaches the value c_b. Fig. 4.4 shows three examples of these pairs of slow waves. It appears that there is a countable set of such solutions similar to the case of falling film flows. Some of the waves in Fig. 4.4 are also shown in the phase space in Fig. 4.5.

It is seen that by varying ξ from $-\infty$ to $+\infty$, the trajectories leave the neighbourhood of the fixed point S_0 along the two-dimensional unstable manifold, and are attracted to

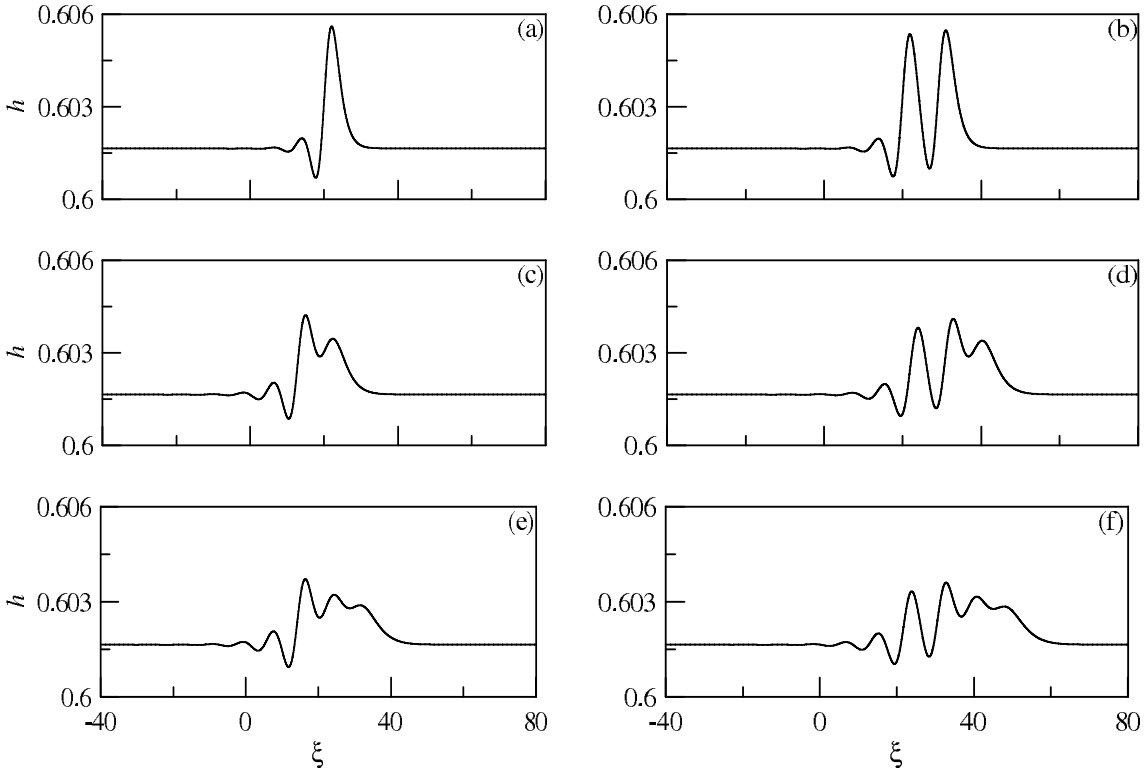

Figure 4.4: Slow solitary waves corresponding to the fixed point S_0: $c = 1.435261$ (a), 1.435308 (b), 1.436117 (c), 1.436145 (d), 1.436390 (e), 1.436411 (f).

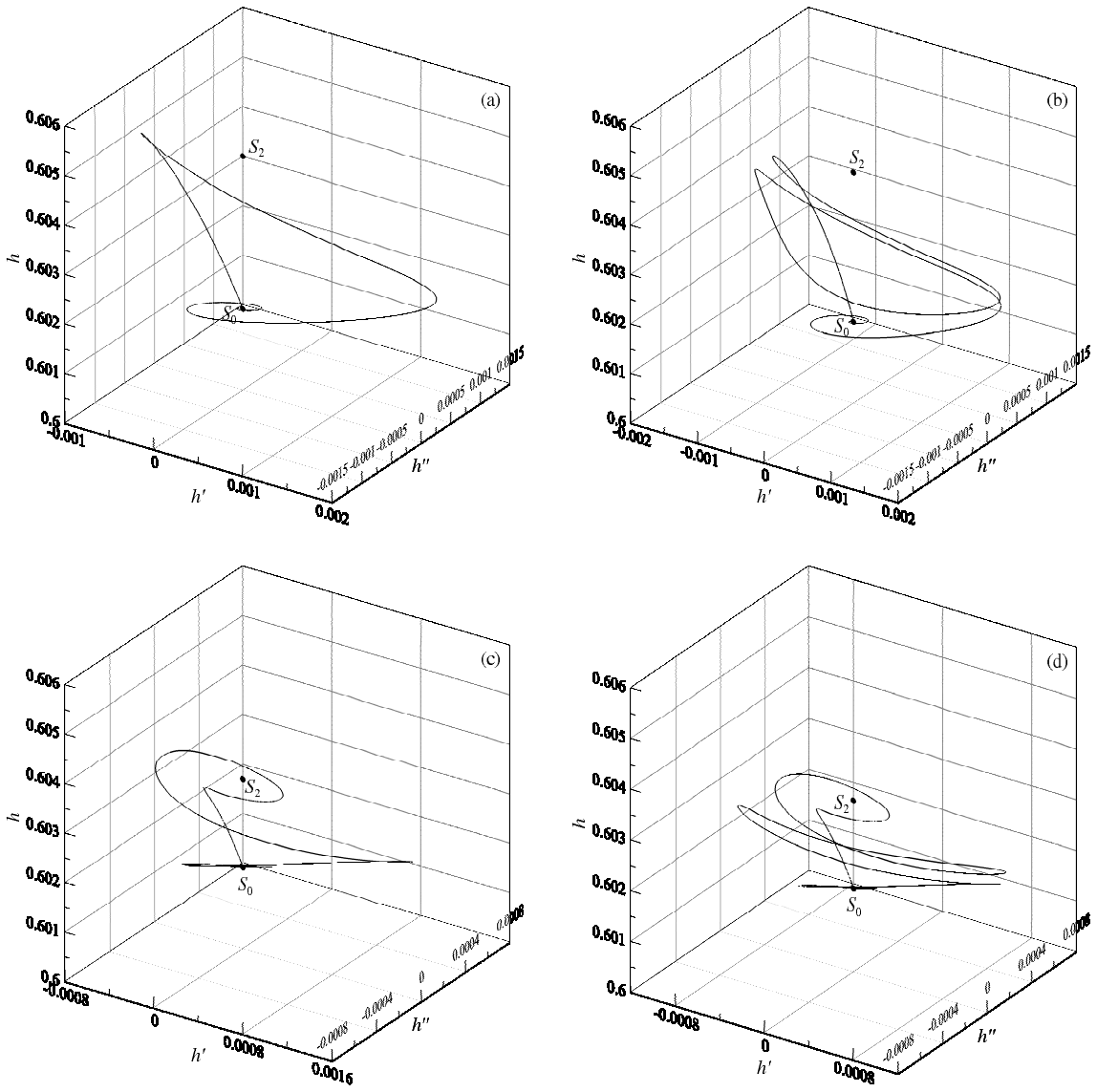

Figure 4.5: Phase trajectories corresponding to waves shown in Fig. 4.4 at $c = 1.435261$ (a), 1.435308 (b), 1.436117 (c), 1.436145 (d).

the domain surrounding the fixed point belonging to the family S_2. Then, the trajectories experience a varying number of oscillations around the fixed point S_2 and/or between the points S_0 and S_2, before finally returning to the point S_0 along the one-dimensional stable manifold. Such trajectories are also typically found for slow solitary waves in falling films.

As a solitary wave has been found, equation (4.2) can be used to find the pressure distribution along the wave. Fig. 4.6 demonstrates the pressure distributions for the waves shown in Fig. 4.4. As expected, these curves have phase shifts corresponding to the waves in the physical space in Fig. 4.4. As discussed in Chapter 1, the ability to work out the first layer thickness based on the pressure distribution at a given point, can potentially offer significant improvements to experimental studies. It may be easier and more accurate to identify and investigate long waves of small amplitude by detecting the pressure distribution along the flow, rather than more conventional methods such as using a high resolution cameras, and build up a profile of the wave shapes based on these measurements.

For each pair of solitary waves shown in Fig. 4.4, many solutions of different types can be found for intermediate velocities. For example, waves with velocities belonging to the interval $(1.436390, 1.436411)$, corresponding to the waves shown in panels Fig. 4.4(e) and 4.4(f), are presented in Fig. 4.7.

For these intermediate velocities, the waves demonstrate more complex patterns. However, it is seen that that the flow returns comprehensively to a parallel state after a prescribed number of oscillations. It is worth while noting that these longer and more complex regimes provide a large contact area between the liquids, intuitively offering greater heat or mass transfer. For each of the four cases shown in Fig. 4.7, by varying ξ from $-\infty$ to $+\infty$, the phase trajectories, see Fig. 4.8, leave the neighbourhood of the fixed point S_0, are attracted towards the neighbourhood of the fixed point S_2, and undergo numerous oscillations around this point. Following this, the trajectories arrive within the domain

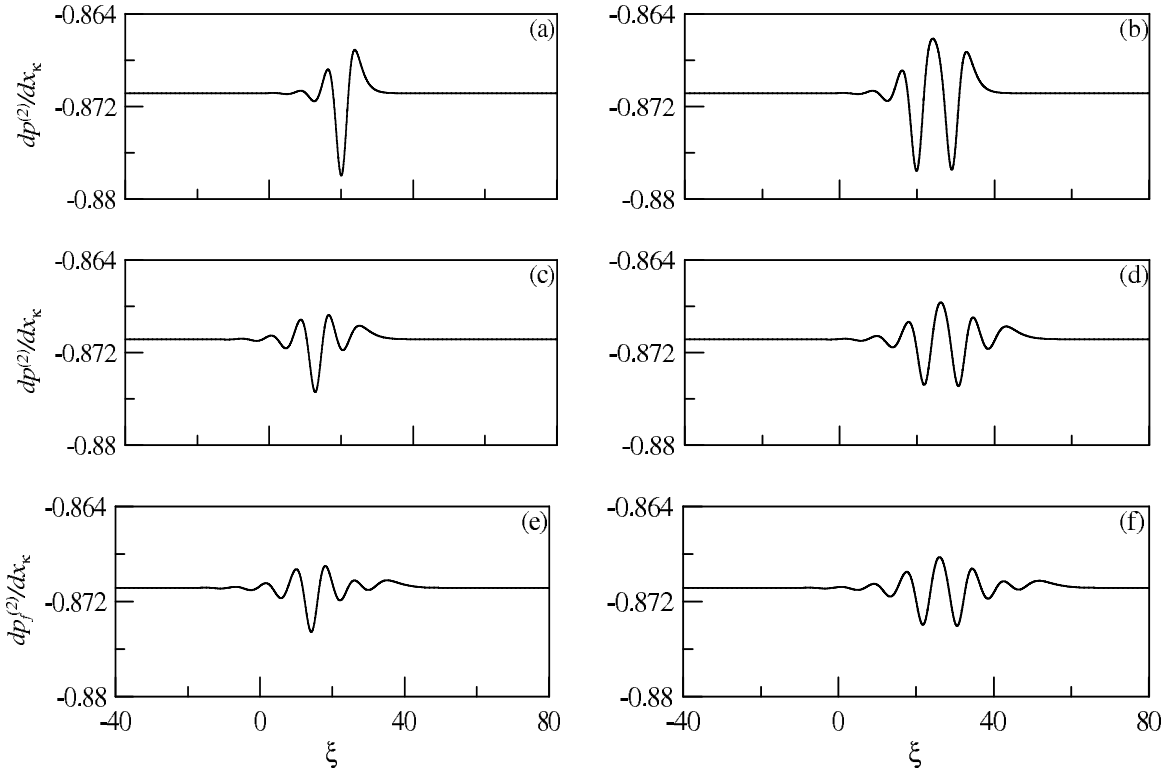

Figure 4.6: Pressure distribution in slow solitary waves corresponding to waves shown in Fig. 4.4 at $c = 1.435261$ (a), 1.435308 (b), 1.436117 (c), 1.436145 (d), 1.436390 (e), 1.436411 (f).

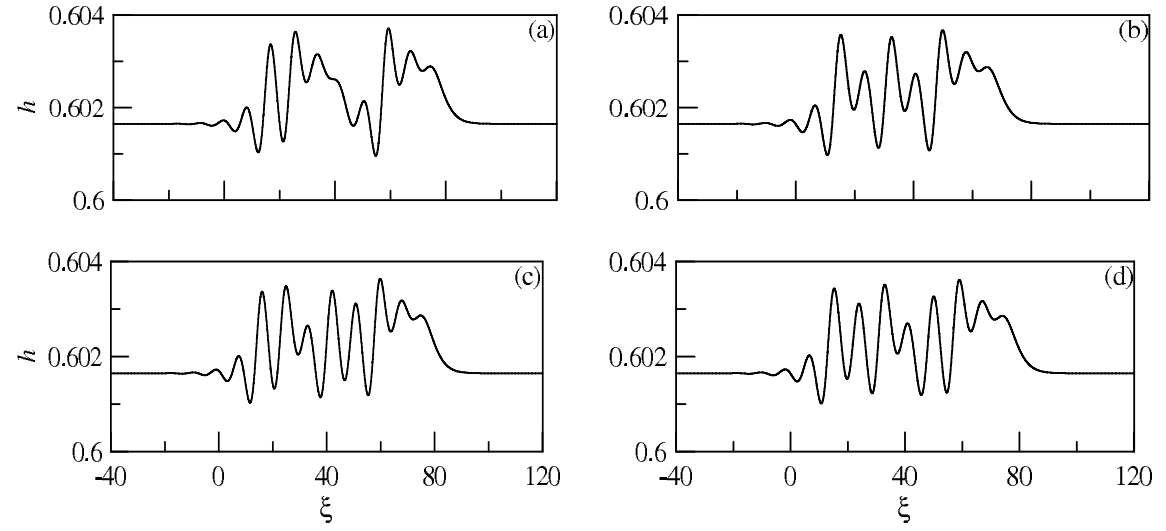

Figure 4.7: Slow solitary waves corresponding to S_0 solution: $c = 1.436391$ (a), 1.436398 (b), 1.436405 (c), 1.436409 (d).

bounded by two planes, corresponding to two-dimensional focus manifolds, stable or unstable, and containing the fixed points S_0 and S_2 respectively. Finally, the trajectories return to the point S_0 along stable one-dimensional manifold.

There is a further set of homoclinic trajectories originating from the fixed point S_0 for $c > c_b$. The corresponding solitary waves are shown in the physical space in Fig. 4.9.

In contrast to the slow waves, these waves are reminiscent of the fast solitary waves found in falling films, if the second layer is considered as the 'film'. These waves have one or two large troughs into the first layer liquid, preceded by small amplitude ripples. For each pair of regimes, the rear of the waves have monotonically decreasing shapes, firstly without oscillations (panels (a) and (b)), secondly with one oscillation (panels (c) and (d)), and finally with two oscillations (panels (e) and (f)). Similar to the slow waves described above, the number of pairs of fast waves whose velocities approach the velocity c_b, seems countable. The phase trajectories of these waves (Fig. 4.10) are comparable to those of the slow waves, but in this case, the fixed point S_2 is located below the fixed point S_0. Another difference is that the point S_0 has an unstable one-dimensional manifold and a stable two-dimensional manifold, as the independent variable ξ varies from $-\infty$ to $+\infty$.

Again, there are many fast solitary waves with velocities belonging to the interval bounded by the velocities of each pair. Four examples of solutions from the interval found in panels (a) and (b) of Fig. 4.9, $(1.438967, 1.439029)$, are demonstrated in Fig. 4.11.

In all cases, the rear sections of the waves are similar to those of the fast solutions shown in Fig. 4.9 panels (a) and (b) with no trailing oscillations. As the velocity is gradually increased from panel (a) to (d), the shape of the centre section of the wave varies from having regular large oscillations with roughly equal amplitudes, to large disturbances followed by smaller ripples.

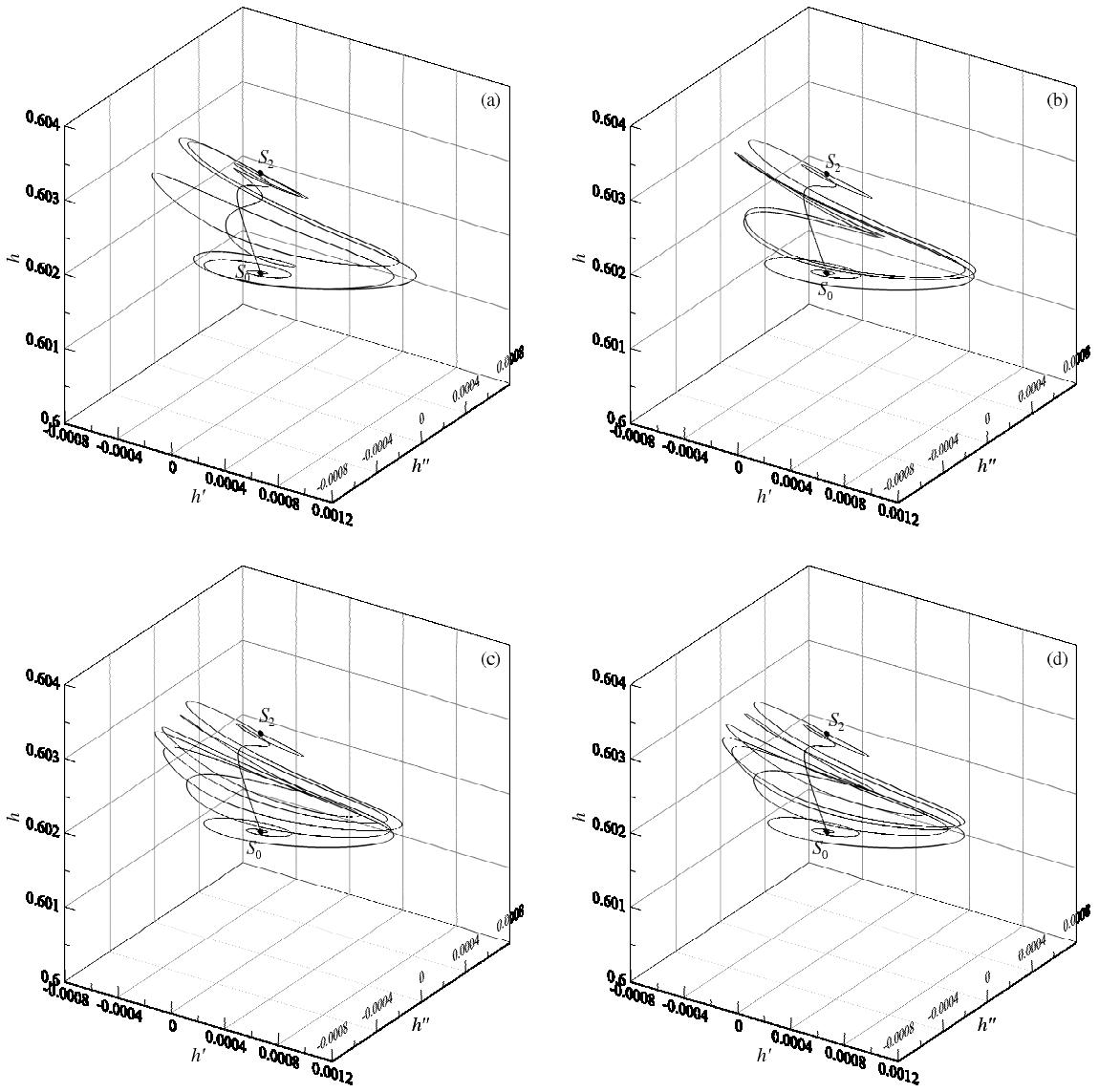

Figure 4.8: Phase trajectories corresponding to waves shown in Fig. 4.7 at $c = 1.436391$ (a), 1.436398 (b), 1.436405 (c), 1.436409 (d).

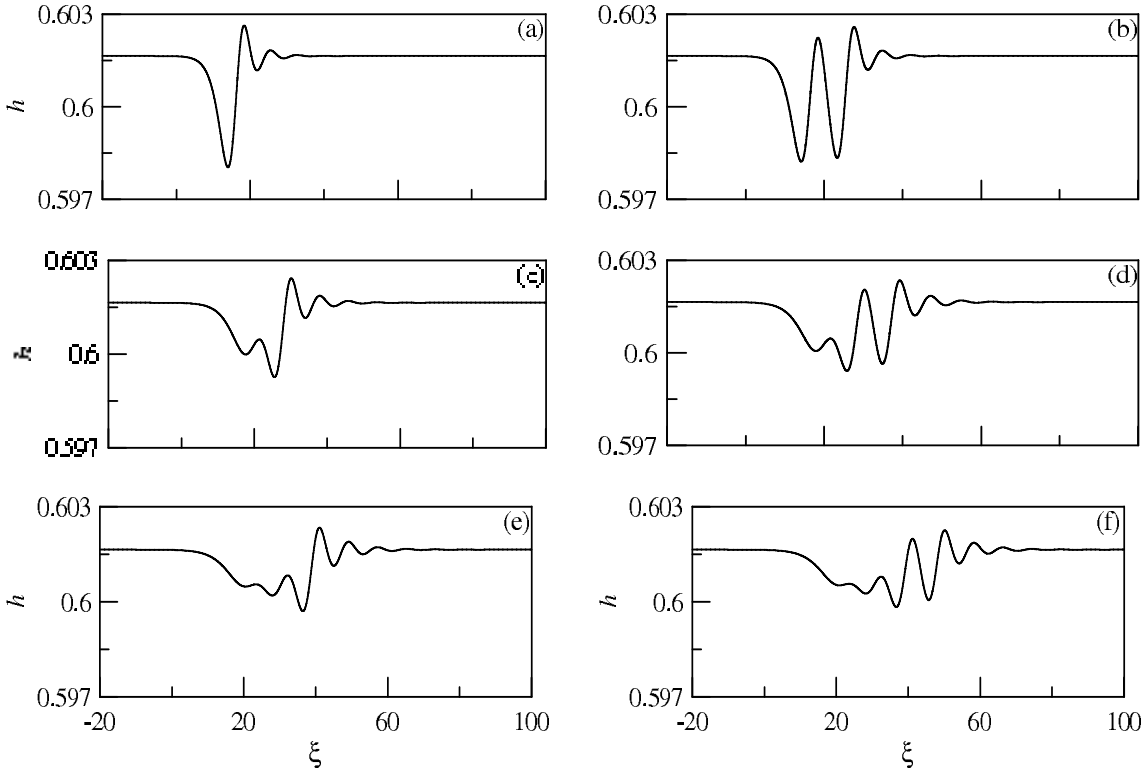

Figure 4.9: Fast solitary waves corresponding to S_0 solution: $c =$ 1.439029 (a), 1.438967 (b), 1.438302 (c), 1.438271 (d), 1.438068 (e), 1.438047 (f).

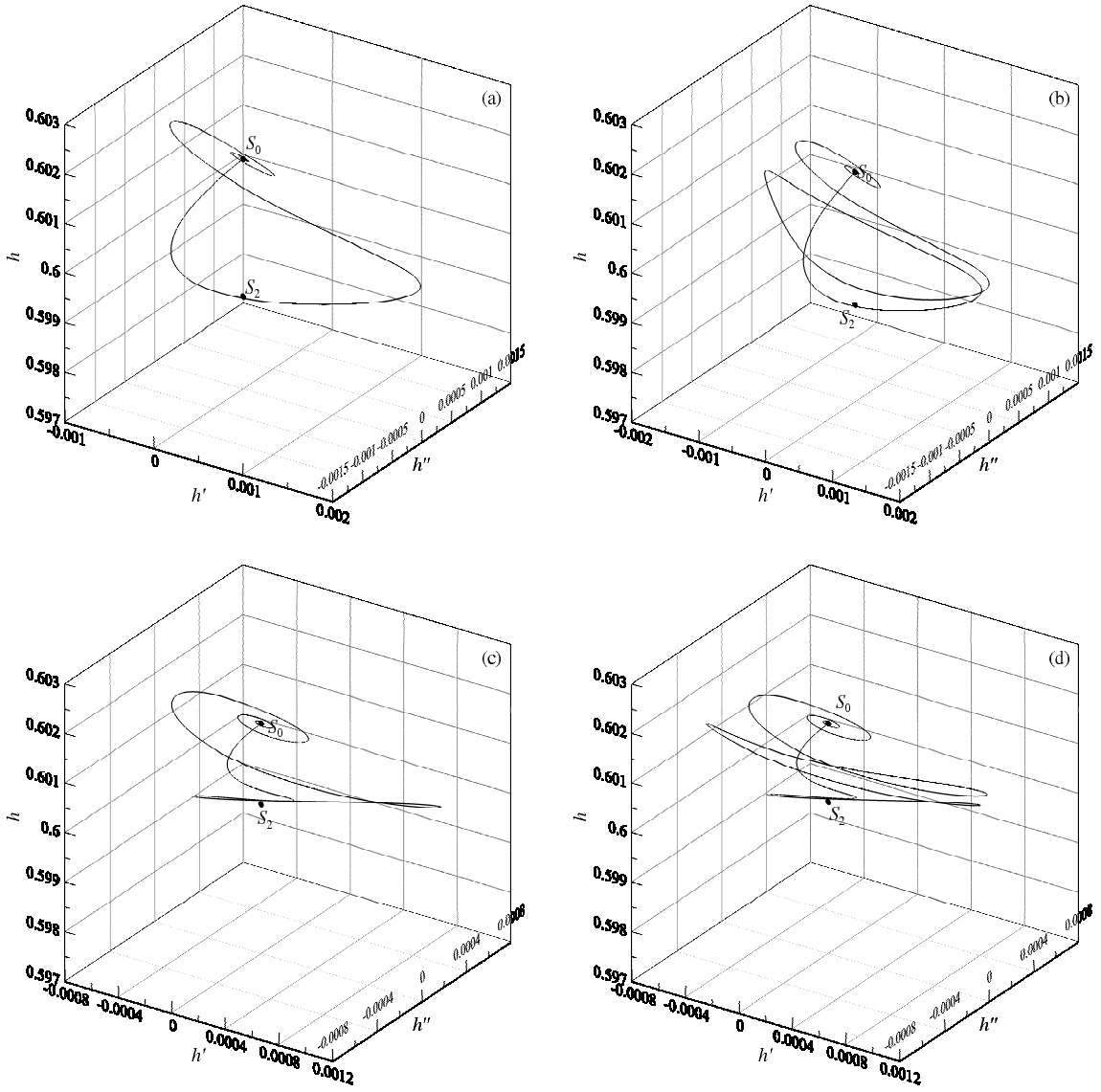

Figure 4.10: Phase trajectories corresponding to waves shown in Fig. 4.9 at $c = 1.439029$ (a), 1.438967 (b), 1.438302 (c), 1.438271 (d).

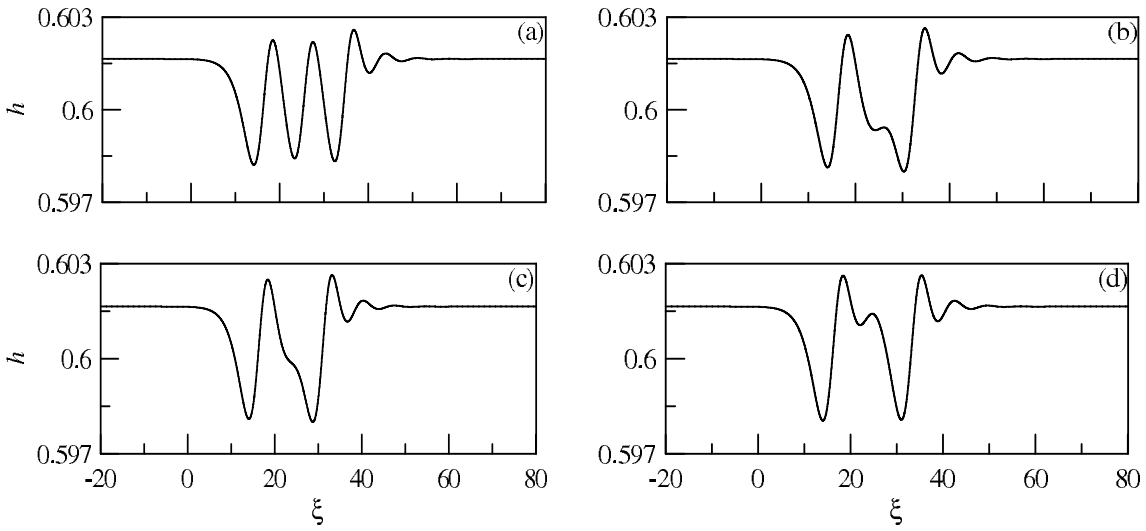

Figure 4.11: Fast solitary waves corresponding to S_0 solution: $c =$ 1.438970 (a), 1.438998 (b), 1.439008 (c), 1.439026 (d).

4.4.5 Homoclinic trajectories of the fixed point S_2

In contrast to the fixed point S_0, the fixed points belonging to the family S_2 are parametrised by the velocity c. This means that the velocity defines both solutions: a fixed point and the corresponding homoclinic trajectory. Here, it is shown that as in the case of the fixed point S_0, there are pairs of slow waves and fast waves.

Examples of slow waves with velocity $c < c_b$, are shown in Fig. 4.12. The shapes of these waves are similar to the slow waves found in falling films, but the ripples are located at the wave front. Also, it is worth noting that the disturbances mainly displace the liquid in the first layer, rather than the second layer as in Fig. 4.4, that is the first layer being considered as the 'film'. It is seen in the phase space (Fig. 4.13), by increasing the variable ξ, the trajectories leave the fixed point S_2 and initially travel along the unstable one-dimensional manifold. The trajectories are then attracted towards the fixed point S_0 and oscillate between the two planes containing the points S_0 and S_2. Finally the trajectories are attracted back towards the point S_2 along the stable two-dimensional

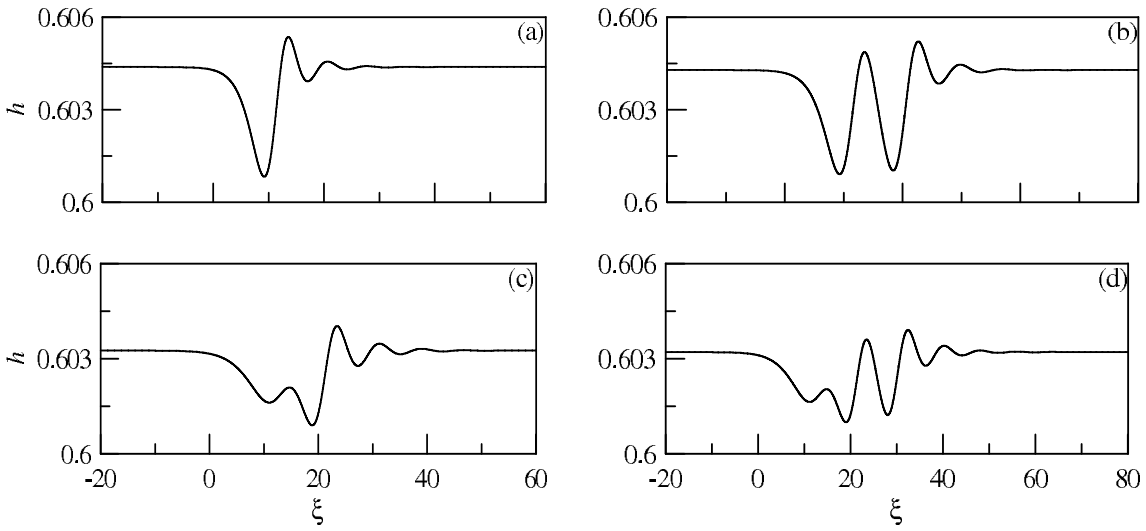

Figure 4.12: Slow solitary waves corresponding to S_2 solution: $c =$ 1.435494 (a), 1.435556 (b), 1.436226 (c), 1.436257 (d).

manifold.

Fast solitary waves for the fixed points S_2 (Fig. 4.14) are also similar to the fast waves for the point S_0 but again, their humps protrude into the domain of the second fluid layer. The diminishing ripples which appeared at the wave front in Fig. 4.9, now appear at the rear of the wave. The phase trajectories (Fig. 4.15) also include exponential parts and oscillating parts as in all previous cases.

Other examples of fast waves and their trajectories are given in Figs. 4.16 and 4.17. These waves have velocities from the interval $(1.438118, 1.438138)$ corresponding to the interval between the third pair of fast solitary waves for the fixed point S_2. Again, due the more unstable nature of the waves appearing at these intermediate values, non-linear parts of the waves are approximately twice as long. All regimes shown here have increasingly larger amplitude oscillations at the rear of the wave, and a monotonically decreasing shape at the wave front. The varying large amplitude oscillations in the centre of the regimes, correspond to the complex phase trajectories (Fig. 4.17), however some repetition and progression can be deciphered. As before, the disturbances return firmly to the fixed

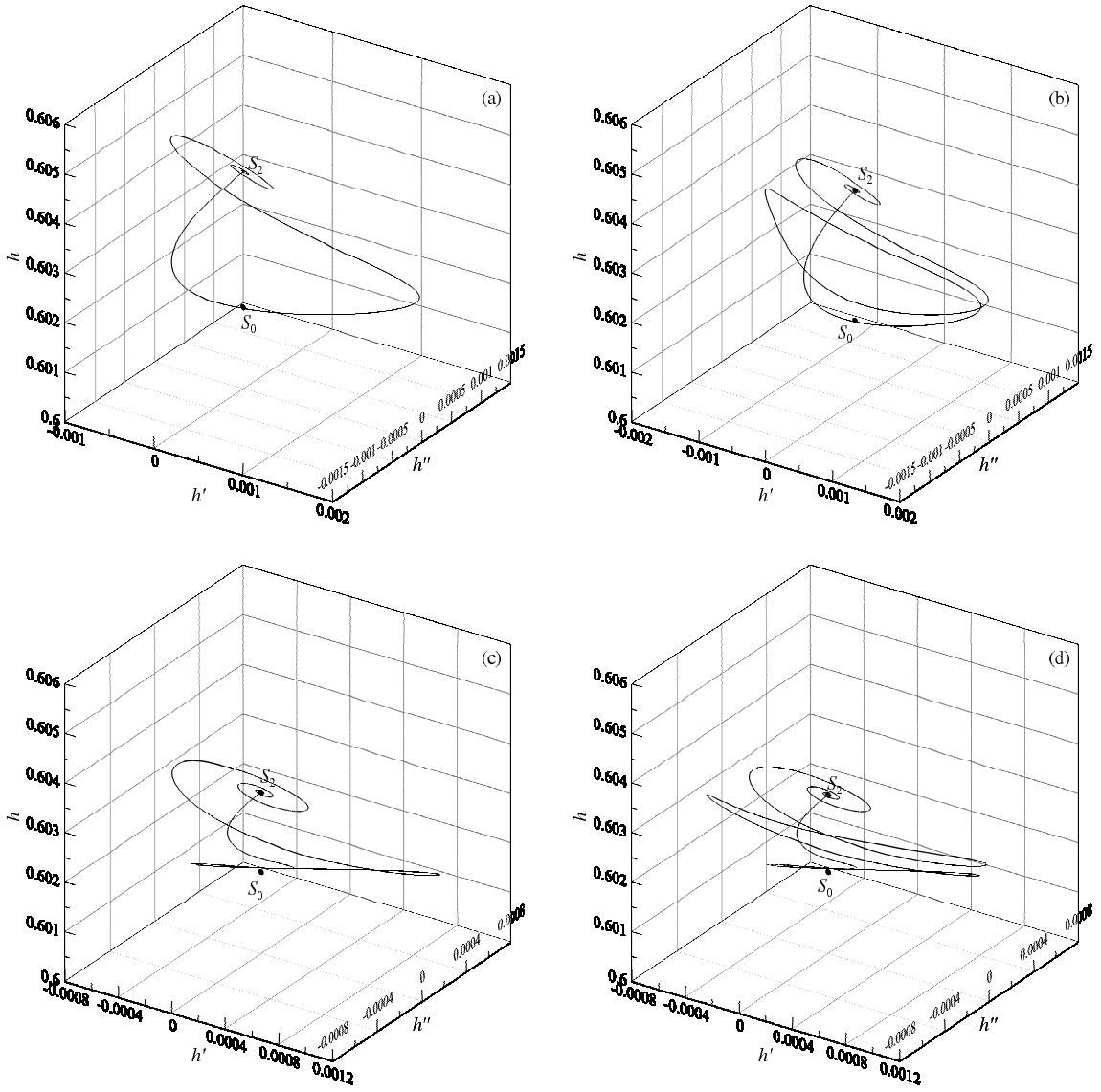

Figure 4.13: Phase trajectories corresponding to waves shown in Fig. 4.12 at $c = 1.435494$ (a), 1.435556 (b), 1.436226 (c), 1.436257 (d).

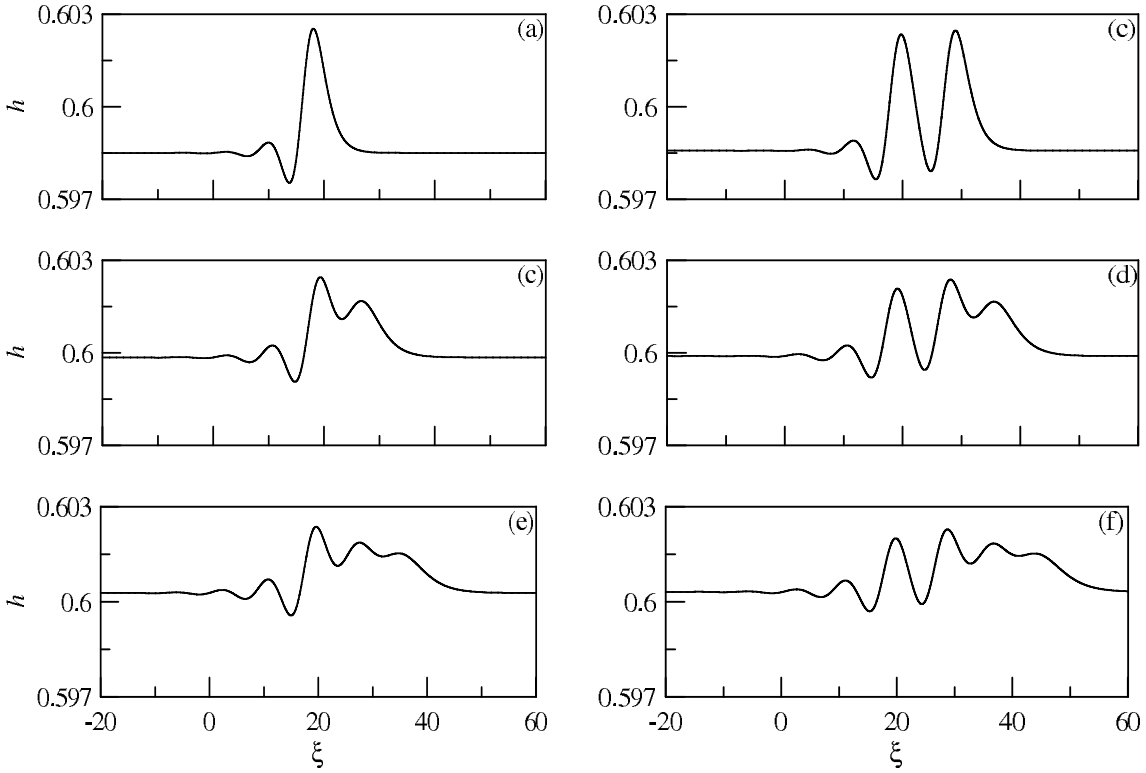

Figure 4.14: Fast solitary waves corresponding to S_2 solution: $c =$ 1.439261 (a), 1.439214 (b), 1.438409 (c), 1.438381 (d), 1.438138 (e), 1.438118 (f).

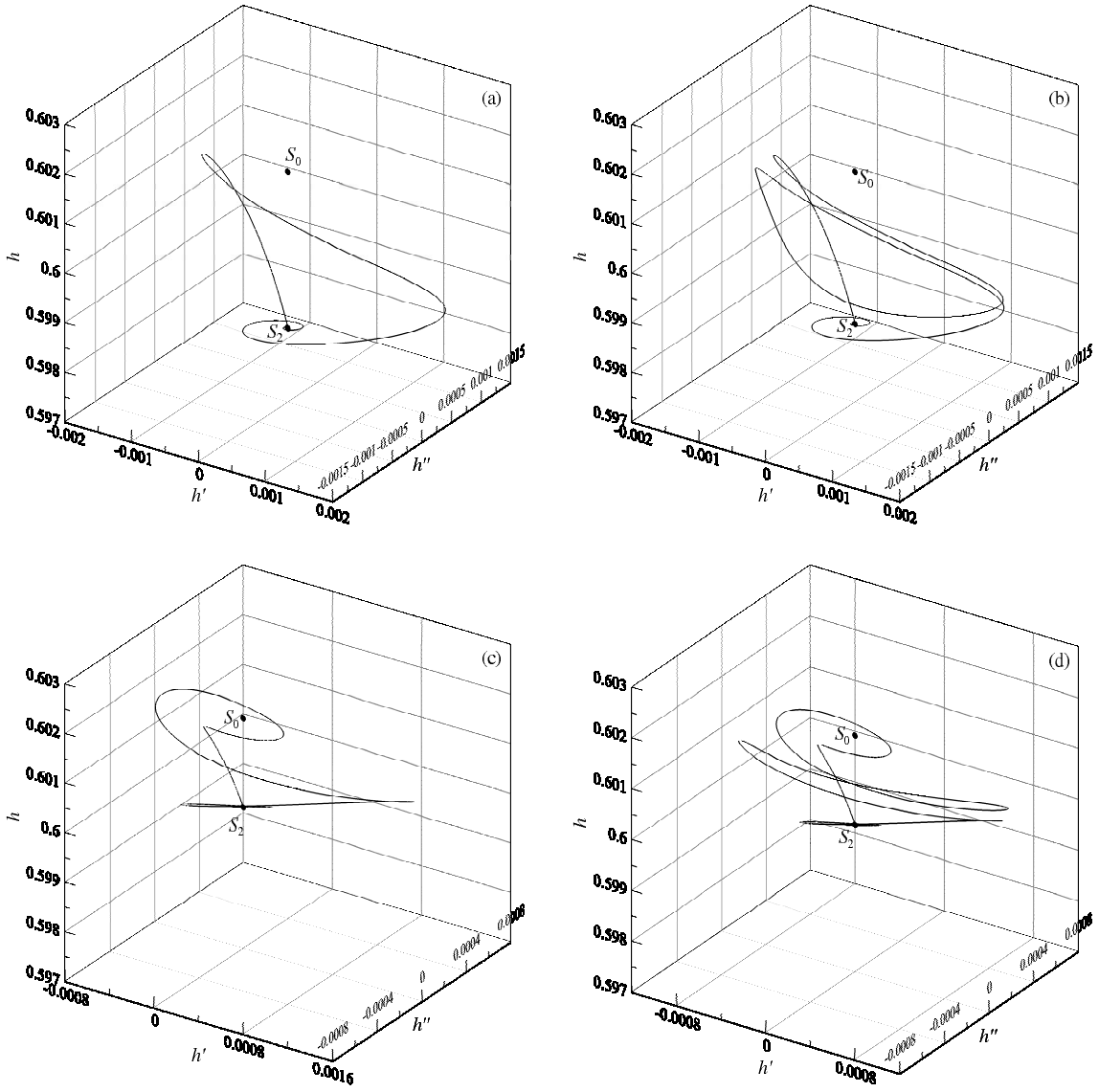

Figure 4.15: Phase trajectories corresponding to waves shown in Fig. 4.14 at $c = 1.439261$ (a), 1.439214 (b), 1.438409 (c), 1.438381 (d).

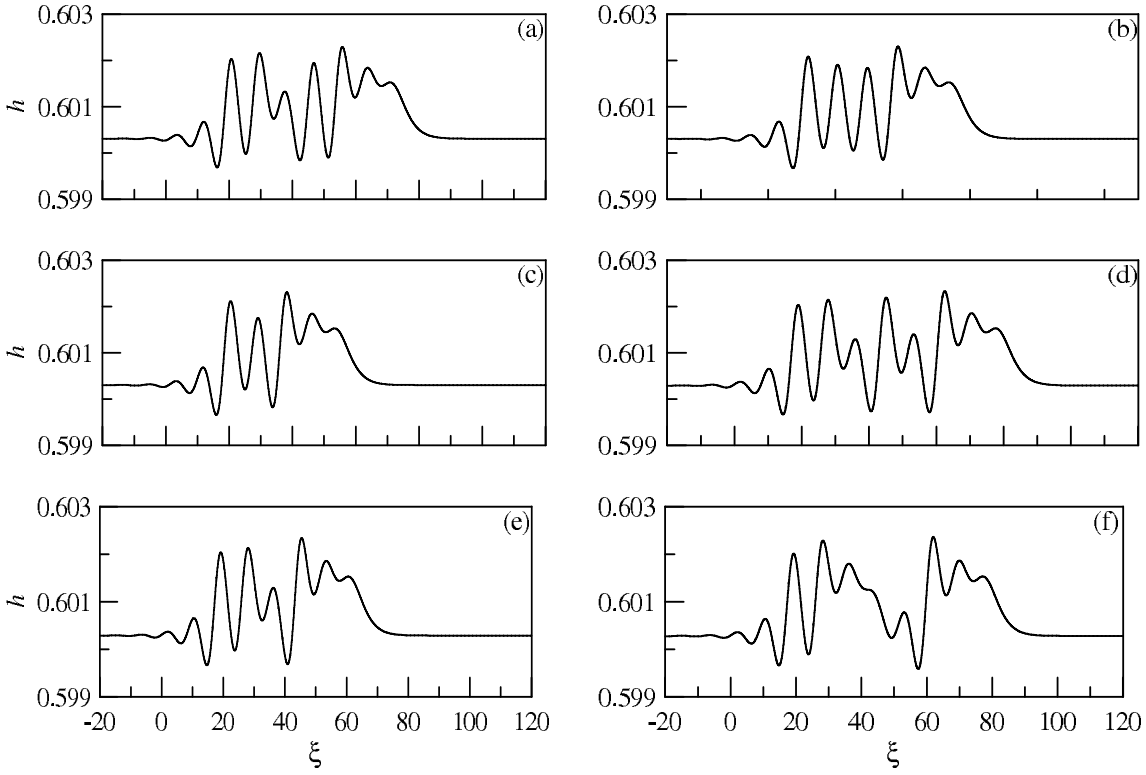

Figure 4.16: Fast solitary waves corresponding to S_2 solution: $c =$ 1.438119 (a), 1.438122 (b), 1.438124 (c), 1.438130 (d), 1.438132 (e), 1.438137 (f).

point.

It is worth noting that solitary waves corresponding to a film thickness different to that of the waveless thickness, have not been found in the falling film theory.

According to Shilnikov's theorem [43], the phase space contains a countable set of periodic orbits in any neighbourhood of each homoclinic trajectory for saddle-focus points, such as S_0 and S_2. In the physical space, each solitary wave is the limit long wave of a family of steady-travelling periodic waves, parametrised by the wavelength when this value tends to infinity. Therefore, it has been shown that numerous families of periodic waves exist in the pressure-driven two-layer microchannel flow, considered here.

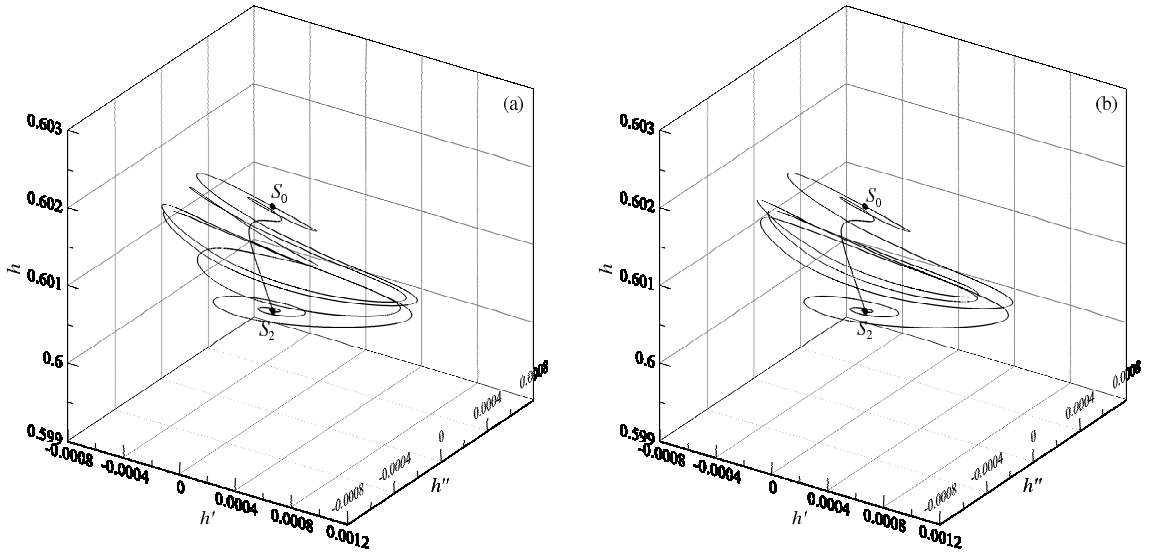

Figure 4.17: Phase trajectories corresponding to waves shown in Fig. 4.16 at $c = 1.438119$ (a) and 1.438122 (b).

4.4.6 Transitional waves

In this section heteroclinic trajectories, corresponding to transitional waves in the physical space, are presented. Both waves of thickening and thinning have been found, and examples are given for the cases of the unstable and stable waveless flow.

In case C of Table 2.1, the waveless flow is unstable, and the existence of solitary waves in this case was demonstrated in Sections (4.4.4) and (4.4.5). The phase trajectories corresponding to the solitary waves, shows that in all cases, the trajectory starting from the fixed point S_0 approaches a small neighbourhood of the fixed point S_2 or vice versa, before returning to the initial point. However in some cases, trajectories originating from S_0 can approach the neighbourhood of S_2 and be attracted to it.

Two examples of transitional waves are shown in Fig. 4.18. In these cases, the transitional waves decrease the thickness of the first layer from the value h_2 to the waveless thickness h_0.

On the other hand, passing waves shown in Figs. 4.19 and 4.20 generate a waveless

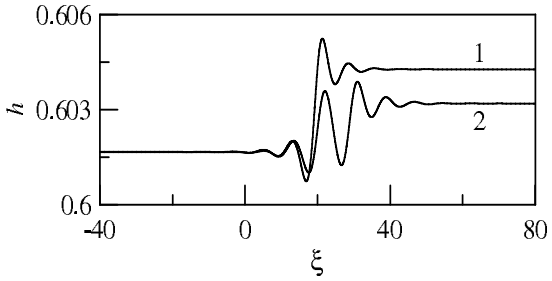

Figure 4.18: Transitional waves with S_0 at $\xi = -\infty$ and S_2 at $\xi = +\infty$: $c = 1.435558$ (curve 1), 1.436256 (2).

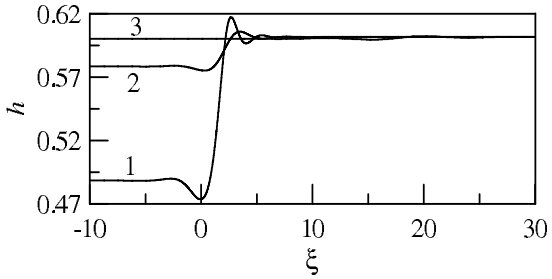

Figure 4.19: Transitional waves with S_2 at $\xi = -\infty$ and S_0 at $\xi = +\infty$: $c = 1.482563$ (curve 1), 1.450989 (2), 1.438128 (3).

flow of thickness h_2 from the waveless flows of thicknesses h_0 and h_1, respectively. In the first case of Fig. 4.19, the wave is faster and the first layer thickness decreases more significantly. In Fig. 4.20 the first layer thickness increases in both cases. Two examples of phase trajectories for solutions having oscillating asymptotics at $\xi \to \pm\infty$, are shown in Fig. 4.21. In both cases, the trajectories lie on the intersection of two two-dimensional, unstable and stable, manifolds of the saddle-foci.

Examples of irregular transitional waves, corresponding to the intersection of a one-dimensional manifold and a two-dimensional manifold, are shown in Fig. 4.22. In the first case, the first layer thickness increases, and in the second case it decreases. In both cases, the waves provide transitions between the fixed points S_0 and S_1. The phase trajectories are shown in Fig. 4.23.

In case A of Table 2.1 the waveless flow is stable, and there are no solitary waves.

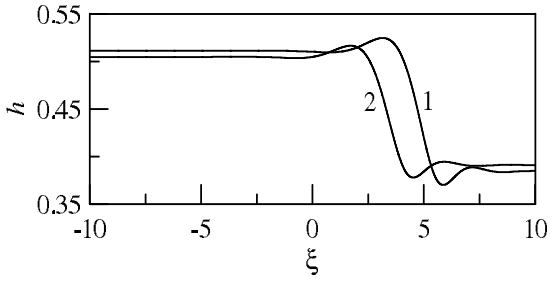

Figure 4.20: Transitional waves with S_2 at $\xi = -\infty$ and S_1 at $\xi = +\infty$: $c = 1.477800$ (curve 1), 1.479320 (2).

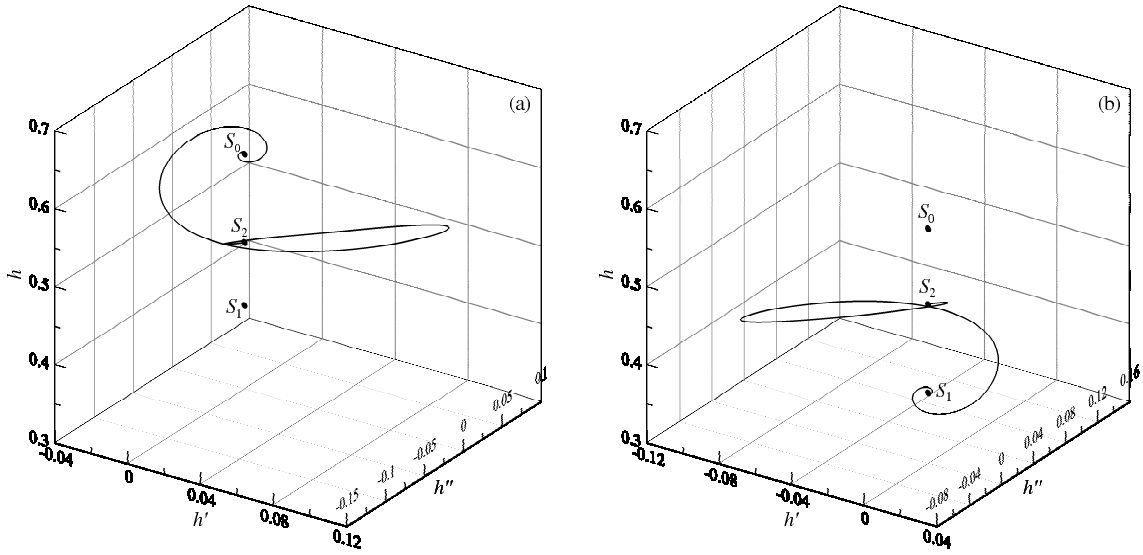

Figure 4.21: Phase trajectories corresponding to waves shown in Fig. 4.19 at $c = 1.482563$ (a) and Fig. 4.20 at $c = 1.479320$ (b).

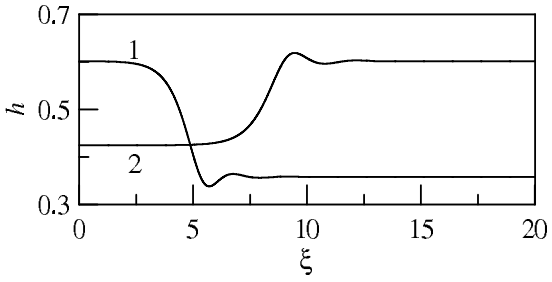

Figure 4.22: Transitional waves with S_0 at $\xi = -\infty$ and S_1 at $\xi = +\infty$ at $c = 1.469809$ (curve 1) and with S_1 at $\xi = -\infty$ and S_0 at $\xi = +\infty$ at $c = 1.484691$ (2).

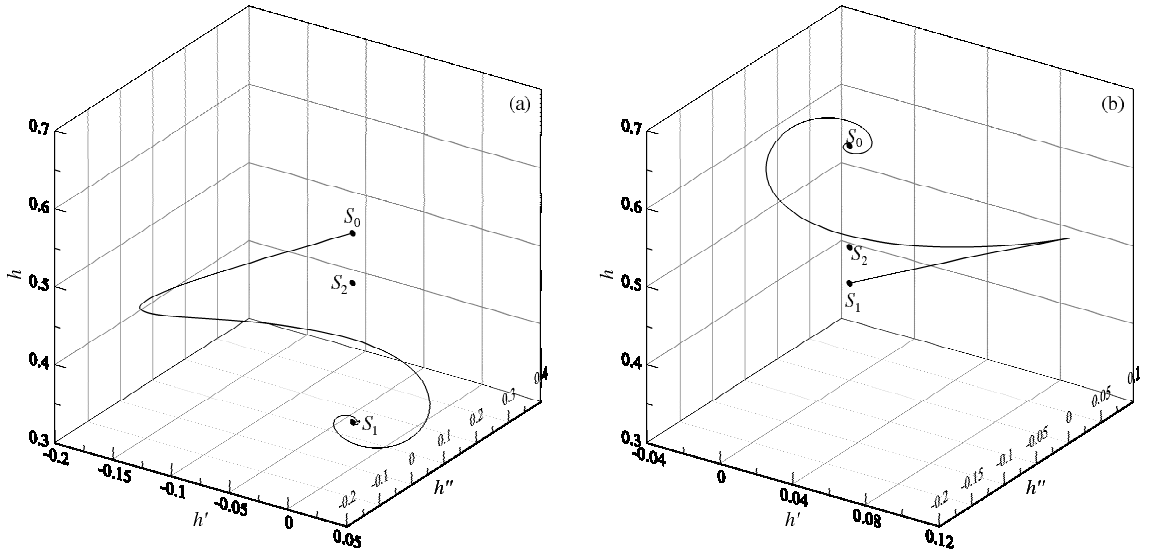

Figure 4.23: Phase trajectories corresponding to waves shown in Fig. 4.22 at $c = 1.469809$ (a) and 1.484691 (b).

However it is seen that transitional waves do exist and such solutions are demonstrated below.

Two examples of transitional waves are shown in Fig. 4.24 at the same value of the velocity c to six decimal places. This is an important example as it demonstrates how sensitive the solution is to infinitesimal changes of the input parameters. These solutions correspond to the regular case of transitional waves when $\beta_r > 0$ for the fixed point $(h_{f,l}, c)$ and $\beta_r < 0$ for the fixed point $(h_{f,r}, c)$. The phase trajectories shown in Fig. 4.25 demonstrate that both trajectories leave the fixed point S_0 along the same unstable two-dimensional manifold, but arrive at different fixed points, S_1 or S_2. This means that the unstable two-dimensional manifold has smooth intersections with two stable two-dimensional manifolds of the fixed points S_1 and S_2.

An example of an irregular wave is shown in Fig. 4.26, where $\beta_r < 0$ at both fixed points $(h_{f,l}, c)$ and $(h_{f,r}, c)$. In this case, the trajectory belongs to the unstable one-dimensional manifold at S_1 intersecting with the stable two-dimensional manifold at S_2 as ξ varies from $-\infty$ to $+\infty$ (Fig. 4.27).

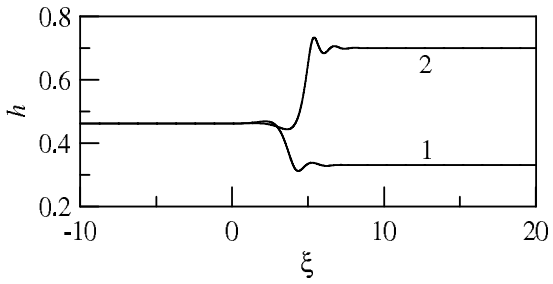

Figure 4.24: Transitional waves with S_0 at $\xi = -\infty$ and S_1 (curve 1) and S_2 (2) at $\xi = +\infty$ at $c = 1.430552$.

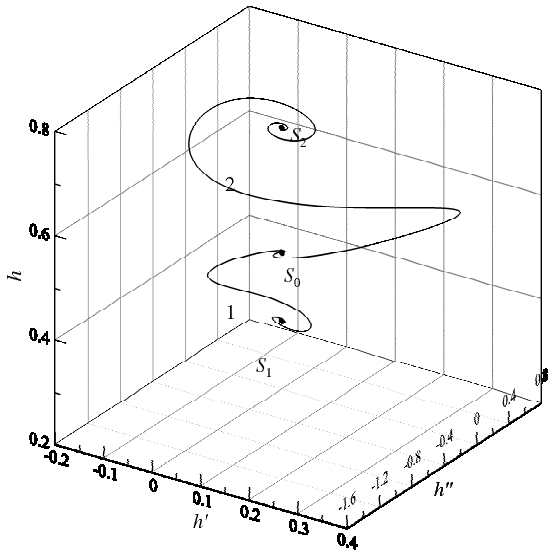

Figure 4.25: Phase trajectories corresponding to waves shown in Fig. 4.24 at $c = 1.430552$.

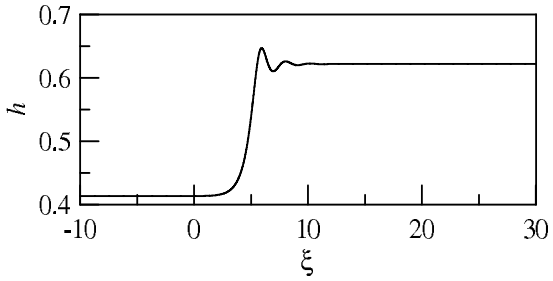

Figure 4.26: Transitional wave with S_1 at $\xi = -\infty$ and S_2 at $\xi = +\infty$ at $c = 1.477548$.

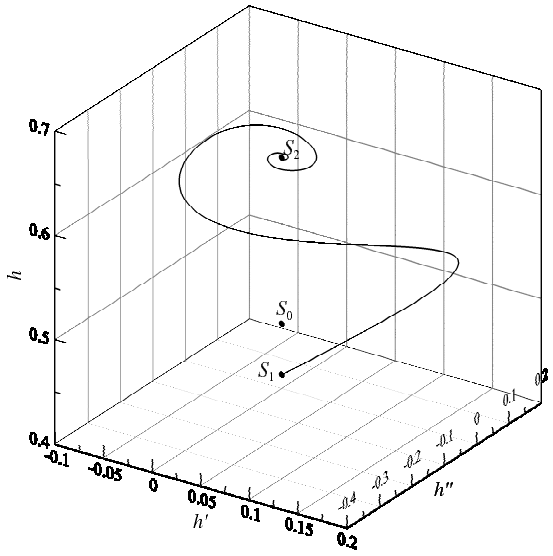

Figure 4.27: Phase trajectory corresponding to the wave shown in Fig. 4.26 at $c = 1.477548$.

It is seen that, as with the gravity-driven case, all solutions found above have wave velocities which fall within a narrow interval, and again, waves are seen to propagate roughly 50% faster than the fluids themselves. However, the amplitudes of the waves found for the pressure-driven case are much smaller than those found for the gravity-driven case, typically $\sim 0.01\%$ of the channel width as compared to $\sim 20\%$. This observation confirms why it is difficult to observe long waves in pressure-driven experiments.

Chapter 5

Conclusions

The aim of this study was to find, for two immiscible fluids flowing simultaneously in a microchannel, solitary and transitional waves propagating on the interface. Flows driven by both gravity and pressure were considered to encapsulate body force driven and boundary condition driven cases. It is seen that solitary and transitional waves do exist, proving the existence of many families of periodic waves by Shilnikov's theorem.

The evolution system for the gravity-driven case, first derived and verified by Sisoev *et al.* [52], was re-derived for a pressure driven flow. Both systems of evolution equations were then transformed into a dynamical system, to which solitary and transitional wave solutions were sought. Both models allowed numerous examples of homoclinic and heteroclinic trajectories in the phase space to be found, using a specifically devised numerical method. In particular, the results given here for the case of the gravity-driven flow, prove that the set of families of steady-travelling periodic waves, is much richer than those found initially by Sisoev *et al.* [52].

Each homoclinic and heteroclinic trajectory found in this Thesis, corresponds to a unique solution of a structurally unstable problem. Each of these results exists at a very specific value of the similarity parameters and the wave velocity, and are individually specified, since the existence of any particular solution does not depend on another. Due

to the structural instability of the problem, the homoclinic or heteroclinic behaviour of a given trajectory is immediately destroyed if a small perturbation is applied.

The trajectories corresponding to solitary and transitional waves in the physical space, were presented at real life values of the similarity parameters, in order to be as realistic as possible.

Waves of this type have not been observed in experiments due to the fact that very long waves with large flat sections are unstable to small perturbations. This is similar to the case of a falling film, where the instability of very long waves was first observed in pioneering experiments conducted by Kapitza and Kapitza [25]. However, the theoretical results given here provide insight into the existence of the corresponding periodic waves. These results can potentially offer advances for a wide spectrum of applications in the micro-device industry, as discussed in Chapter 1.

In future work, the aim is to specifically identify examples of the periodic waves eluded to in this study. Following the periodic wave study, the mass transfer problem may be solved to give details on the improved efficiency provided by wavy interfacial flows. Furthermore, the case of a three-layer microchannel flow, such as that seen in experiments by Zhao *et al.* [68] (see also Li *et al.* [30]), where a cross-flow junction is used to inject a more viscous fluid into the stream of another, may also be modelled using the same approach.

Chapter A

Appendices

A.1 Linearised coefficients

$$
\begin{aligned}
A^{(1)}_{11,0} &= \left[1-\left(1-2\rho_0\nu_0\right)h_0\right]\left[4-\left(4-\rho_0\nu_0\right)h_0\right]+2\rho_0\nu_0h_0\left(h_0-1\right),\\
A^{(1)}_{11,1} &= -\left[1-\left(1-2\rho_0\nu_0\right)h_0\right]\left[4-\left(4-\rho_0\nu_0\right)h_0\right]\\
&\quad\times\left(\frac{1-2\rho_0\nu_0}{1-\left(1-2\rho_0\nu_0\right)h_0}+\frac{4-\rho_0\nu_0}{4-\left(4-\rho_0\nu_0\right)h_0}\right)\\
&\quad+2\rho_0\nu_0h_0\left(h_0-1\right)\left(\frac{1}{h_0}+\frac{1}{h_0-1}\right),\\
A^{(2)}_{11,0} &= \frac{A^{(1)}_{11,0}}{1-\left(1-\rho_0\nu_0\right)h_0},\\
A^{(2)}_{11,1} &= A^{(2)}_{11,0}\left(\frac{A^{(1)}_{11,1}}{A^{(1)}_{11,0}}+\frac{1-\rho_0\nu_0}{1-\left(1-\rho_0\nu_0\right)h_0}\right),\\
A^{(3)}_{11,0} &= 4-2\left(2-\rho_0\nu_0\right)h_0-A^{(2)}_{11,0},\\
A^{(3)}_{11,1} &= -2\left(2-\rho_0\nu_0\right)-A^{(2)}_{11,1},\\
A^{(4)}_{11,0} &= \frac{3A^{(3)}_{11,0}\left(q-q^{(1)}_0\right)}{h_0\left(h_0-1\right)^2},\\
A^{(4)}_{11,1} &= A^{(4)}_{11,0}\left(\frac{A^{(3)}_{11,1}}{A^{(3)}_{11,0}}-\frac{1}{h_0}-\frac{2}{h_0-1}\right),
\end{aligned}
$$

$$A_{11,2}^{(4)} = -\frac{A_{11,0}^{(4)}}{q - q_0^{(1)}},$$

$$A_{11,0}^{(5)} = \frac{3\left[1-(1-2\rho_0\nu_0)\,h_0\right]}{h_0^2\left[1-(1-\rho_0\nu_0)\,h_0\right]}\; q_0^{(1)},$$

$$A_{11,1}^{(5)} = A_{11,0}^{(5)}\left(\frac{1-\rho_0\nu_0}{1-(1-\rho_0\nu_0)\,h_0} - \frac{1-2\rho_0\nu_0}{1-(1-2\rho_0\nu_0)\,h_0} - \frac{2}{h_0}\right),$$

$$A_{11,2}^{(5)} = \frac{A_{11,0}^{(5)}}{q_0^{(1)}},$$

$$a_{11,0} = A_{11,0}^{(5)} + A_{11,0}^{(4)}, \quad a_{11,1} = A_{11,1}^{(5)} + A_{11,1}^{(4)}, \quad a_{11,2} = A_{11,2}^{(5)} + A_{11,2}^{(4)};$$

$$A_{12,0}^{(1)} = \left[1-(1-2\rho_0\nu_0)\,h_0\right]\left[4-(4-\rho_0\nu_0)\,h_0\right],$$

$$A_{12,1}^{(1)} = -A_{12,0}^{(1)}\left(\frac{1-2\rho_0\nu_0}{1-(1-2\rho_0\nu_0)\,h_0} + \frac{4-\rho_0\nu_0}{4-(4-\rho_0\nu_0)\,h_0}\right),$$

$$A_{12,0}^{(2)} = \frac{A_{12,0}^{(1)}}{1-(1-\rho_0\nu_0)\,h_0},$$

$$A_{12,1}^{(2)} = A_{12,0}^{(2)}\left(\frac{A_{12,1}^{(1)}}{A_{12,0}^{(1)}} + \frac{1-\rho_0\nu_0}{1-(1-\rho_0\nu_0)\,h_0}\right),$$

$$A_{12,0}^{(3)} = 4 - 2\,(2-\rho_0\nu_0)\,h_0 - A_{12,0}^{(2)},$$

$$A_{12,1}^{(3)} = -2\,(2-\rho_0\nu_0) - A_{12,1}^{(2)},$$

$$A_{12,0}^{(4)} = \frac{3A_{12,0}^{(3)}}{2h_0^2\,(h_0-1)^2}\left(q - q_0^{(1)}\right),$$

$$A_{12,1}^{(4)} = A_{12,0}^{(4)}\left(\frac{A_{12,1}^{(3)}}{A_{12,0}^{(3)}} - \frac{2}{h_0} - \frac{2}{h_0-1}\right),$$

$$A_{12,2}^{(4)} = -\frac{A_{12,0}^{(4)}}{q - q_0^{(1)}},$$

$$A_{12,0}^{(5)} = \frac{3\left[1-(1-4\rho_0\nu_0)\,h_0\right]}{2h_0^3\left[1-(1-\rho_0\nu_0)\,h_0\right]}\; q_0^{(1)},$$

$$A_{12,1}^{(5)} = A_{12,0}^{(5)}\left(-\frac{1-4\rho_0\nu_0}{1-(1-4\rho_0\nu_0)\,h_0} - \frac{3}{h_0} + \frac{1-\rho_0\nu_0}{1-(1-\rho_0\nu_0)\,h_0}\right),$$

$$A_{12,2}^{(5)} = \frac{A_{12,0}^{(5)}}{q_0^{(1)}},$$

$$a_{12,0} = -A_{12,0}^{(5)} - A_{12,0}^{(4)}, \quad a_{12,1} = -A_{12,1}^{(5)} - A_{12,1}^{(4)}, \quad a_{12,2} = -A_{12,2}^{(5)} - A_{12,2}^{(4)};$$

$$A_{21,0}^{(1)} = \frac{3\left[2-(2-\rho_0\nu_0)\,h_0\right]}{(h_0-1)^2\left[1-(1-\rho_0\nu_0)\,h_0\right]}\;\left(q - q_0^{(1)}\right),$$

$$A_{21,1}^{(1)} = A_{21,0}^{(1)} \left(\frac{1-\rho_0\nu_0}{1-(1-\rho_0\nu_0)\,h_0} - \frac{2-\rho_0\nu_0}{2-(2-\rho_0\nu_0)\,h_0} - \frac{2}{h_0-1} \right),$$

$$A_{21,2}^{(1)} = -\frac{A_{21,0}^{(1)}}{q-q_0^{(1)}},$$

$$A_{21,0}^{(2)} = \frac{3}{h_0\left[1-(1-\rho_0\nu_0)\,h_0\right]}\; q_0^{(1)},$$

$$A_{21,1}^{(2)} = A_{21,0}^{(2)} \left(\frac{1-\rho_0\nu_0}{1-(1-\rho_0\nu_0)\,h_0} - \frac{1}{h_0} \right),$$

$$A_{21,2}^{(2)} = \frac{A_{21,0}^{(2)}}{q_0^{(1)}},$$

$$a_{21,0} = A_{21,0}^{(2)} - A_{21,0}^{(1)}, \quad a_{21,1} = A_{21,1}^{(2)} - A_{21,1}^{(1)}, \quad a_{21,2} = A_{21,2}^{(2)} - A_{21,2}^{(1)};$$

$$A_{22,0}^{(1)} = \frac{3\left[4-(4-\rho_0\nu_0)\,h_0\right]}{2\left(h_0-1\right)^3\left[1-(1-\rho_0\nu_0)\,h_0\right]}\; \left(q-q_0^{(1)}\right),$$

$$A_{22,1}^{(1)} = A_{22,0}^{(1)} \left(\frac{1-\rho_0\nu_0}{1-(1-\rho_0\nu_0)\,h_0} - \frac{4-\rho_0\nu_0}{4-(4-\rho_0\nu_0)\,h_0} - \frac{3}{h_0-1} \right),$$

$$A_{22,2}^{(1)} = -\frac{A_{22,0}^{(1)}}{q-q_0^{(1)}},$$

$$A_{22,0}^{(2)} = \frac{9}{2h_0\left(h_0-1\right)\left[1-(1-\rho_0\nu_0)\,h_0\right]}\; q_0^{(1)},$$

$$A_{22,1}^{(2)} = A_{22,0}^{(2)} \left(\frac{1-\rho_0\nu_0}{1-(1-\rho_0\nu_0)\,h_0} - \frac{1}{h_0} - \frac{1}{h_0-1} \right),$$

$$A_{22,2}^{(2)} = \frac{A_{22,0}^{(2)}}{q_0^{(1)}},$$

$$a_{22,0} = -A_{22,0}^{(2)} + A_{22,0}^{(1)}, \quad a_{22,1} = -A_{22,1}^{(2)} + A_{22,1}^{(1)}, \quad a_{22,2} = -A_{22,2}^{(2)} + A_{22,2}^{(1)};$$

$$I_{1,0} = \frac{a_{11,0}^2 h_0^3}{3} + \frac{a_{11,0}a_{12,0}h_0^4}{2} + \frac{a_{12,0}^2 h_0^5}{5},$$

$$I_{1,1} = \frac{a_{11,0}^2 h_0^3}{3} \left(\frac{2a_{11,1}}{a_{11,0}} + \frac{3}{h_0} \right) + \frac{a_{11,0}a_{12,0}h_0^4}{2} \left(\frac{a_{11,1}}{a_{11,0}} + \frac{a_{12,1}}{a_{12,0}} + \frac{4}{h_0} \right)$$
$$+ \frac{a_{12,0}^2 h_0^5}{5} \left(\frac{2a_{12,1}}{a_{12,0}} + \frac{5}{h_0} \right),$$

$$I_{1,2} = \frac{2a_{11,0}a_{11,2}}{3}h_0^3 + \frac{a_{11,0}a_{12,2} + a_{11,2}a_{12,0}}{2}h_0^4 + \frac{2a_{12,0}a_{12,2}}{5}h_0^5,$$

$$I_{2,0} = \frac{a_{21,0}^2}{3}\left(h_0-1\right)^3 + \frac{a_{21,0}a_{22,0}}{2}\left(h_0-1\right)^4 + \frac{a_{22,0}^2}{5}\left(h_0-1\right)^5,$$

$$I_{2,1} = \frac{a_{21,0}^2}{3}\left(h_0-1\right)^3 \left(\frac{2a_{21,1}}{a_{21,0}} + \frac{3}{h_0-1} \right)$$

$$
\begin{aligned}
&+\frac{a_{21,0}a_{22,0}}{2}\left(h_0-1\right)^4\left(\frac{a_{21,1}}{a_{21,0}}+\frac{a_{22,1}}{a_{22,0}}+\frac{4}{h_0-1}\right)\\
&+\frac{a_{22,0}^2}{5}\left(h_0-1\right)^5\left(\frac{2a_{22,1}}{a_{22,0}}+\frac{5}{h_0-1}\right),\\
I_{2,2}=&\frac{2a_{21,0}a_{21,2}}{3}\left(h_0-1\right)^3+\frac{a_{21,0}a_{22,2}+a_{21,2}a_{22,0}}{2}\left(h_0-1\right)^4\\
&+\frac{2a_{22,0}a_{22,2}}{5}\left(h_0-1\right)^5.
\end{aligned}
$$

A.2 Partial derivatives of the dynamical system (4.3)

$$
\begin{aligned}
\frac{\partial a_{11}}{\partial h}=&\left[-\frac{3(1-2\rho_0\nu_0)}{h^2[1-(1-\rho_0\nu_0)h]}-\frac{6[1-(1-2\rho_0\nu_0)h]}{h^3[1-(1-\rho_0\nu_0)h]}\right.\\
&\left.+\frac{3(1-\rho_0\nu_0)[1-(1-2\rho_0\nu_0)h]}{h^2[1-(1-\rho_0\nu_0)h]^2}\right]q^{(1)}\\
&+\left[\left(-\frac{3}{h^2(h-1)^2}-\frac{6}{h(h-1)^3}\right)(4-2(2-\rho_0\nu_0)h\right.\\
&\left.-\frac{[1-(1-2\rho_0\nu_0)h][4-(4-\rho_0\nu_0)h]+2\rho_0\nu_0h(h-1)}{1-(1-\rho_0\nu_0)h}\right)\\
&+\frac{3}{h(h-1)^2}\left(-2(2-\rho_0\nu_0)\right.\\
&-\frac{-(1-2\rho_0\nu_0)[4-(4-\rho_0\nu_0)h]-[1-(1-2\rho_0\nu_0)h](4-\rho_0\nu_0)+2\rho_0\nu_0(2h-1)}{1-(1-\rho_0\nu_0)h}\\
&\left.-(1-\rho_0\nu_0)\frac{[1-(1-2\rho_0\nu_0)h][4-(4-\rho_0\nu_0)h]+2\rho_0\nu_0h(h-1)}{[1-(1-\rho_0\nu_0)h]^2}\right)\Bigg](1-q^{(1)})\\
\frac{\partial a_{11}}{\partial q^{(1)}}=&\frac{3[1-(1-2\rho_0\nu_0)h]}{h^2[1-(1-\rho_0\nu_0)h]}-\frac{3}{h(h-1)^2}\\
&\times\left[4-2(2-\rho_0\nu_0)h-\frac{[1-(1-2\rho_0\nu_0)h][4-(4-\rho_0\nu_0)h]+2\rho_0\nu_0h(h-1)}{1-(1-\rho_0\nu_0)h}\right]\\
\frac{\partial a_{12}}{\partial h}=&\left[\frac{3(1-4\rho_0\nu_0)}{2h^3[1-(1-\rho_0\nu_0)h]}+\frac{9[1-(1-4\rho_0\nu_0)h]}{2h^4[1-(1-\rho_0\nu_0)h]}\right.\\
&\left.-\frac{3(1-\rho_0\nu_0)[1-(1-4\rho_0\nu_0)h]}{2h^3[1-(1-\rho_0\nu_0)h]^2}\right]q^{(1)}\\
&+\left[\left(\frac{3}{h^3(h-1)^2}+\frac{3}{h^2(h-1)^3}\right)\right.\\
&\left.\times\left(4-2(2-\rho_0\nu_0)h-\frac{[1-(1-2\rho_0\nu_0)h][4-(4-\rho_0\nu_0)h]}{1-(1-\rho_0\nu_0)h}\right)\right.
\end{aligned}
$$

$$
\begin{aligned}
&-\frac{3}{2h^2(h-1)^2}\left(-2(2-\rho_0\nu_0)\right.\\
&+\frac{(1-2\rho_0\nu_0)[4-(4-\rho_0\nu_0)h]+[1-(1-2\rho_0\nu_0)h](4-\rho_0\nu_0)}{1-(1-\rho_0\nu_0)h}\\
&\left.-(1-\rho_0\nu_0)\frac{[1-(1-2\rho_0\nu_0)h][4-(4-\rho_0\nu_0)h]}{[1-(1-\rho_0\nu_0)h]^2}\right)\Bigg](1-q^{(1)})\\
\frac{\partial a_{12}}{\partial q^{(1)}} &= -\frac{3[1-(1-4\rho_0\nu_0)h]}{2h^3[1-(1-\rho_0\nu_0)h]}+\frac{3}{2h^2(h-1)^2}\\
&\times\left(4-2(2-\rho_0\nu_0)h-\frac{[1-(1-2\rho_0\nu_0)h][4-(4-\rho_0\nu_0)h]}{1-(1-\rho_0\nu_0)h}\right)\\
\frac{\partial a_{21}}{\partial h} &= \left[-\frac{3}{h^2[1-(1-\rho_0\nu_0)h]}+\frac{3(1-\rho_0\nu_0)}{h[1-(1-\rho_0\nu_0)h]^2}\right]q^{(1)}\\
&+\left[\frac{3(2-\rho_0\nu_0)}{(h-1)^2[1-(1-\rho_0\nu_0)h]}+\frac{6[2-(2-\rho_0\nu_0)h]}{(h-1)^3[1-(1-\rho_0\nu_0)h]}\right.\\
&\left.-\frac{3(1-\rho_0\nu_0)[2-(2-\rho_0\nu_0)h]}{(h-1)^2[1-(1-\rho_0\nu_0)h]^2}\right](1-q^{(1)})\\
\frac{\partial a_{21}}{\partial q^{(1)}} &= \frac{3}{h[1-(1-\rho_0\nu_0)h]}+\frac{3[2-(2-\rho_0\nu_0)h]}{(h-1)^2[1-(1-\rho_0\nu_0)h]}\\
\frac{\partial a_{22}}{\partial h} &= \left[\frac{9}{2h^2(h-1)[1-(1-\rho_0\nu_0)h]}+\frac{9}{2h(h-1)^2[1-(1-\rho_0\nu_0)h]}\right.\\
&\left.-\frac{9(1-\rho_0\nu_0)}{2h(h-1)[1-(1-\rho_0\nu_0)h]^2}\right]q^{(1)}+\left[-\frac{3(4-\rho_0\nu_0)}{2(h-1)^3[1-(1-\rho_0\nu_0)h]}\right.\\
&\left.-\frac{9[4-(4-\rho_0\nu_0)h]}{2(h-1)^4[1-(1-\rho_0\nu_0)h]}+\frac{3(1-\rho_0\nu_0)[4-(4-\rho_0\nu_0)h]}{2(h-1)^3[1-(1-\rho_0\nu_0)h]^2}\right](1-q^{(1)})\\
\frac{\partial a_{22}}{\partial q^{(1)}} &= -\frac{9}{2h(h-1)[1-(1-\rho_0\nu_0)h]}-\frac{3[4-(4-\rho_0\nu_0)h]}{2(h-1)^3[1-(1-\rho_0\nu_0)h]}
\end{aligned}
$$

A.3 Linearised coefficients k_0 and k_1 for equation (3.8)

$$
\begin{aligned}
k_1 &= \frac{5\delta\beta}{h_f}\left[c^2\left(1+\frac{\rho_0 h_f}{1-h_f}\right)-(I_{1,1}+cI_{1,2})-\frac{\rho_0 h_f}{1-h_f}(I_{2,1}+cI_{2,2})\right]\\
k_0 &= \frac{1}{h_f}\left[\frac{2\left(a_{12,0}-\rho_0\nu_0 a_{22,0}\right)}{\gamma}+\frac{2h_f}{\gamma}\left(a_{12,1}-\rho_0\nu_0 a_{22,1}\right)+\frac{2h_f c}{\gamma}\left(a_{12,2}-\rho_0\nu_0 a_{22,2}\right)\right.\\
&\left.+1-\rho_0\right].
\end{aligned}
$$

Coefficents $I_{i,j}$ and $a_{ij,k}$ are given above, in (A.1).

List of References

[1] D. J. Acheson. *Elementary Fluid Dynamics*. Clarendon Press, Oxford, 1990.

[2] R. A. Adams. *Calculus: A Complete Course (Edition 8)*. Prentice Hall Canada, 2013.

[3] S. V. Alekseenko, V. E. Nakoryakov, and B. G. Pokusaev. *Wave Flow of Liquid Films*. Begel House, Inc., New York, 1994.

[4] D. G. Arkhipov and G. A. Khabakhpashev. Modeling of long nonlinear waves on the interface in a horizontal two-layer viscous channel flow. *Fluid Dynamics*, 40(1):126–139, 2005.

[5] D. G. Arkhipov and G. A. Khabakhpashev. Evolution of long nonlinear waves on the interface of a stratified viscous fluid flow in a channel. *Journal of Applied Mechanics and Technical Physics*, 48(4):508–518, 2007.

[6] P. A. M. Boomkamp and R. H. M. Miesen. Classification of instabilities in parallel two-phase flow. *International Journal of Multiphase Flow*, 22(Suppl.):67–88, 1996.

[7] A. V. Bunov, E. A. Demekhin, and V. Ya. Shkadov. Bifurcations of solitary waves on a flowing liquid film. *Moscow University Mechanics Bulletin*, 41(2):73–78, 1986.

[8] J. R. Burns and C. Ramshaw. Development of a microreactor for chemical production. *Chemical Engineering Research and Design*, 77:206–211, 1999.

[9] Q. Cao, K. Sarkar, and A. K. Prasad. Direct numerical simulations of two-layer viscosity-stratified flow. *International Journal of Multiphase Flow*, 30:1485–1508, 2004.

[10] G. Çekiç and G. Sisoev. Dominating wave regimes in a two-layer film flowing down a vertical wall. *Physics of Fluids*, 26, 2014.

[11] H.-C. Chang. Wave evolution on a falling film. *Annual Review of Fluid Mechanics*, 26:103–136, 1994.

[12] H.-C. Chang and E. A. Demekhin. *Complex Wave Dynamics on Thin Films*. Elsevier, Amsterdam, 2002. 412pp.

[13] M. E. Charles and L. U. Lilleleht. An experimental investigation of stability and interfacial waves in co-current flow of two liquids. *Journal of Fluid Mechanics*, 22(2):217–224, 1965.

[14] F. Charru and J. Fabre. Long waves at the interface between two viscous fluids. *Phisics of Fluids*, 6(3):1223–1235, 1994.

[15] S. Colin(Ed.). *Microfluidics*. ISTE Ltd., 2010.

[16] A.-L. Dessimoz, L. Cavin, A. Renken, and L. Kiwi-Minsker. Liquid-liquid two-phase flow patterns and mass transfer characteristics inrectangular glass microreactors. *Chemical Engineering Science*, 63:4035–4044, 2008.

[17] A. M. Frank. Shear driven solitary waves on a liquid film. *Physical Review E*, 74:065301, 2006.

[18] A. M. Frank. Numerical simulation of gas driven waves on a liquid film. *Physics of Fluids*, 20:122102, 2008.

[19] P. Guillot and A. Colin. Stability of parallel flows in a micrchannel after a t junction. *Physical Review E*, 72:066301, 2005.

[20] A. Günther and K. F. Jensen. Multiphase microfluidics: from flow characteristics to chemical and material synthesis. *Lab on a Chip*, 6:1487–1503, 2006.

[21] A. Gunther and T. Kreutzer. *Multiphase Flow*. Wiley, 2009.

[22] S. Hardt and T. Hahn. Microfluidics with aqueous two-phase systems. *Lab on a Chip*, 12:434–442, 2012.

[23] A. P. Hooper and R. Grimshaw. Nonlinear instability at the interface between two viscous fluids. *Physics of Fluids*, 28(1):37–45, 1985.

[24] T. W. Kao and C. Park. Experimental investigation of the stability of channel flow. Part 2. Two-layred co-current flow in rectangular channel. *Journal of Fluid Mechanics*, 52:401–423, 1972.

[25] P. L. Kapitza and S. P. Kapitza. Wave flow of thin viscous liquid films. III. Experimental study of wave regime of a flow. *Journal of Experimental and Theoretical Physics*, 19(2):105–120, 1949.

[26] M. N. Kashid, A. Renken, and L. Kiwi-Minsker. Gas-liquid and liquid-liquid mass transfer in microstructured reactors. *Chemical Engineering Science*, 66:3876–3897, 2011.

[27] N. Kockmann, T. Kiefer, M. Engler, and P. Woias. Convective mixing and chemical reactions in microchannels with high flow rates. *Sensors and Actuators B*, 117:495–508, 2006.

[28] D. J. Korteweg and G. de Vries. On the change of form of long waves advancing in a rectangular canal and on a new type of long stationary waves. *Philosophical Magazine*, 39:422–443, 1895.

[29] W. C. Kuru, M. Sangalli, D. D. Uphold, and M. J. McCready. Linear stability of stratified channel flow. *International Journal of Multiphase Flow*, 21(5):733–753, 1995.

[30] J. Li, P. Sheeran, and C. Kleinstreuer. Analysis of multi-layer immiscible fluid flow in a microchannel. *Journal of Fluids Engineering*, 133, 2011.

[31] T. Maruyama, J. Uchida, T. Ohkawa, T. Futami, K. Katayama, K. Nishizawa, K. Sotowa, F. Kubota, and M. Kamiya, N. Gote. Enzymatic degradation of *p*-clorophenol in a two-phase flow microchannel system. *Lab on a Chip*, 3:308–312, 2003.

[32] O. K. Matar, C. J. Lawrence, and G. M. Sisoev. Interfacial dynamics in pressure-driven two-layer laminar channel flow with high viscosity ratios. *Physical Review E*, 75:056313, 2007.

[33] O. K. Matar, G. M. Sisoev, and C. J. Lawrence. Two-layer flow with one viscous layer in inclined channels. *Mathematical Modelling of Natural Phenomena*, 3:126–148, 2008.

[34] A. Mavromoustaki, O. K. Matar, and R. V. Craster. Shock-wave solutions in two-layer channel flow. i. one-dimensional flows. *Physics of Fluids*, 22(112102):1–19, 2010.

[35] N. Nguyen and S. Wereley. *Fundamentals and Applications of Microfluidics*. Artech House, 2 edition, 2006.

[36] W. McF. Orr. Stability and instability of steady motions of a perfect liquid. *Proc. Ir. Acad. Sect. A, Math Astron. Phys. Sci*, 27, 1907.

[37] W. McF. Orr. Stability and instability of steady motions of a perfect liquid, part ii: a viscous liquid. *Proc. Ir. Acad. Sect. A, Math Astron. Phys. Sci*, 27, 1907.

[38] A. Pohar, M. Lakner, and I. Plazl. Parallel flow of immiscible liquids in a microreactor: modeling and experimental study. *Microfluid Nanofluid*, 12:307–316, 2012.

[39] J. W. S. Rayleigh. Investigation of the character of the equilibrium of an incompressible heavy fluid of variable density. *Proceedings of the London Mathematical Society*, 14:170–177, 1883.

[40] R. M. Roberts, Y. Ye, E. A. Demekhin, and H.-C. Chang. Wave dynamics in two-layer couette flow. *Chemical Engineering Science*, 55:345–362, 2000.

[41] J. Scott Russell. *Report on Waves*. Meetings of the British Association, 1845.

[42] T. M. Segin, B. S. Tilley, and L. Kondic. On undercompressive shocks and flooding in countercurrent two-layer-flows. *Journal of FLuid Mechanics*, 532:217–242, 2005.

[43] L. P. Shilnikov. A case of the existence of a countable number of periodic motions (point mapping proof of existence theorem showing neighborhood of trajectory which departs from and returns to saddle-point focus contains denumerable set of periodic motions). *Soviet Mathematics*, 6:163–166, 1965.

[44] V. Ya. Shkadov. Wave flow regimes of a thin layer of viscous fluid subject to gravity. *Fluid Dynamics*, 2(1):29–34, 1967.

[45] V. Ya. Shkadov. Solitary waves in a viscous liquid layer. *Fluid Dynamics*, 12(1):52–55, 1977.

[46] V. Ya. Shkadov and G. M. Sisoev. Wavy falling liquid films: theory and computation instead of physical experiment. In H.-C. Chang, editor, *IUTAM Symposium on Nonlinear Waves in Multi-Phase Flow*, volume 57 of *Fluid Mechanics and Its Applications*, pages 1–10, Notre Dame, USA, July 2000. Notre Dame University, Kluwer. Hardbound, ISBN 0-7923-6454-6, 272p.

[47] V. Ya. Shkadov and G. M. Sisoev. On the theory of solitary waves in flowing-down layer of viscous fluid. *Doklady-Physics*, 46(10):760–764, 2001.

[48] V. Ya. Shkadov and G. M. Sisoev. Waves induced by instability in falling films of finite thickness. *Fluid Dynamics Research*, 35(5):357–389, 2004.

[49] G. Sisoev and C. Bennett. Solitary and transitional waves in gravity-driven two-layer microchannel flow. *Fluid Dynamics Research*, 45:015503, 2013.

[50] G. Sisoev and C. Bennett. Solitary and transitional waves in pressure-driven two-layer microchannel flow. *Fluid Dynamics Research*, 46:025504, 2014.

[51] G. M. Sisoev, O. K. Matar, and C. J. Lawrence. Absorption of gas into a wavy falling film. *Chemical Engineering Science*, 60:827–838, 2005.

[52] G. M. Sisoev, O.K. Matar, D. Sileri, and C.J. Lawrence. Wave regimes in two-layer microchannel flow. *Chemical Engineering Science*, 64:3094–3102, 2009.

[53] A. Sommerfeld. A contribution to the hydrodynamical explanation of turbulent fluid motions. *Proc. Int. Congress Math. Rome*, 3, 1908.

[54] M. J. South and A. P. Hooper. Linear growth in two-fluid plane Poiseuille flow. *Journal of Fluid Mechanics*, 381:121–139, 1999.

[55] J. E. Steinbrenner, C. H. Hidrovo, F.-M. Wang, S. Vigneron, E. S. Lee, T. A. Krammer, C.-H. Cheng, J. K. Eaton, and K. E. Goodson. Measurement and modeling of liquid film thickness evolution in stratified two-phase microchannel flows. *Applied Thermal Engineering*, 27:1722–1727, 2007.

[56] H. A. Stone, A. D. Stroock, and A. Ajdari. Engineering flows in small devices: Microfluidics toward a lab-on-a-chip. *Annual Review of Fluid Mechanics*, 36:381–411, 2004.

[57] P. Tabeling. *Introduction to Microfluidics*. Oxford University Press, 2005.

[58] G. I. Taylor. The instability of liquid surfaces when accelerated in a direction perpendicular to their planes. *Proceedings of the Royal Society of London*, 201:192–196, 1950.

[59] B. S. Tilley, S. H. Davis, and S. G. Bankoff. Linear stability theory of two-layer fluid flow in an inclined channel. *Physics of Fluids*, 6(12):3906–3922, 1994.

[60] B. S. Tilley, S. H. Davis, and S. G. Bankoff. Nonlinear long-wave stability of superposed fluids in an inclined channel. *Journal of Fluid Mechanics*, 277:55–83, 1994.

[61] M. Tokeshi, T. Minagawa, K. Uchiyama, A. Hibara, K. Sato, H. Hisamoto, and T. Kitamori. Continuous-flow chemical processing on a microchip by combining microunit operations and a multiphase network. *Analytical Chemistry*, 74(7):1565–1571, 2002.

[62] L. N. Trefethen, L. N. Trefethen, S. C. Reddy, and T. A. Dricoll. Hydrodynamic stability without eigenvalues. *Science*, 261(578):1234, 1993. (Ud).

[63] S. G. Yiantsios and B. G. Higgins. Linear stability of plane poiseuille flow of two superposed fluids. *Physics of Fluids*, 31(11):3225–3236, 1988.

[64] C.-S. Yih. Instability due to viscosity stratification. *Journal of Fluid Mechanics*, 27(2):337–352, 1967.

[65] J. Zhang, M. J. Miksis, Bankoff S. G., and G. Tryggvason. Nonlinear dynamics of an interface in an inclined channel. *Physics of FLuids*, 14:1877–1885, 2002.

[66] C.-X. Zhao and A. P. J. Middelberg. Two-phase microfluidic flows. *Chemical Engineering Science*, 66:1394–1411, 2011.

[67] Y. Zhao, G. Chen, and Q. Yuan. Liquid-liquid two-phase flow patterns in a rectangular microchannels. *AIChE Journal*, 52(12):4052–4060, 2006.

[68] Y. Zhao, G. Chen, and Q. Yuan. Liquid-liquid two-phase mass transfer in the T-junction microchannels. *AIChE Journal*, 53(12):3042–3053, 2007.

[69] Y. Zhao, Y. Su, G. Chen, and Q. Yuan. Effect of surface properties on the flow characteristics and mass transfer performance in microchannels. *Chemical Engineering Science*, 65:1563–1570, 2010.